What's in the Box?

Towards a Mechanistic Understanding of Twin-Screw Extrusion of Plant Proteins: Local Processing Conditions and Flow Behavior

Zur Erlangung des akademischen Grades eines

DOKTORS DER INGENIEURWISSENSCHAFTEN (Dr.-Ing.)

von der KIT-Fakultät für Chemieingenieurwesen und Verfahrenstechnik des

Karlsruher Instituts für Technologie (KIT)

genehmigte

DISSERTATION

von

M.Sc. Felix Ellwanger

aus Heidelberg, Germany

Tag der mündlichen Prüfung:	21.05.2026
Erstgutachter:	Priv. Doz. Dr.-Ing. Azad Emin
Zweitgutachter:	Prof. Dr.-Ing. Hermann Nirschl

Für meine Mutter Uli, meinen Vater Stefan und meinen Bruder Daniel.

Table of Contents

Abstract

Accompanied by extensive studies, meat analogues have gained significant attention, evolving from niche alternatives into popular options for flexitarians. To further improve their appeal, continued product development is necessary. This includes enhancing sensory properties, such as taste and texture, as well as diversifying the raw materials used. Meeting these demands requires a mechanistic understanding of the process in order to perform targeted product design instead of relying on trial-and-error or experience.

The twin-screw extrusion process is the key technology for producing meat analogues. Despite extensive research, the mechanistic understanding required for targeted product design remains incomplete. In particular, the interplay between local process conditions and resulting structure is not yet fully understood. One reason is the limited availability of methods capable of examining both the process and the material properties under extrusion-relevant conditions.

This thesis contributed to closing this gap by using three complementary methods to investigate and link local processing conditions with material behavior under extrusion: the structure modulation method, the ramp test method, and the Moving-Particle Semi-Implicit (MPS) simulation method.

To study the extrusion process, which is complex and involves many modifiable parameters affecting both process conditions and product properties, a model process was required to generate reproducible model products. The first step was therefore to establish a method that allows modification of the final product structure without changing either the process parameters or the protein source. This requirement was fulfilled by the structure modulation method presented in chapter 2. In this method, the pH of the liquid phase was systematically lowered by adding acids. It is well known that changes in pH affect the surface charge of proteins and thereby influence their folding and intermolecular interactions. Accordingly, pH adjustment was expected to alter network formation during extrusion and thus change product properties. Material screening of soy protein isolate (SPI) and wheat gluten doughs in a closed cavity rheometer confirmed these expected effects. Lowering the pH increased the complex viscosity of SPI, whereas gluten displayed altered reaction behavior. Extrusion trials reflected these findings. SPI extrudates became denser and more brittle with decreasing pH, while gluten extrudates became more elastic and dough-like. Mechanical and solubility analyses further revealed that SPI formed a higher density of physical cross-links, while gluten formed fewer disulfide bonds. Based on these results, SPI processed with the structure modulation method was selected as the model system for this thesis, as it produced a controllable set of model products for systematic investigation.

To gain a mechanistic understanding of the extrusion process, the local process conditions must be known. Since these conditions strongly influence product properties but can only be measured to a limited extent, chapter 3 presents a method for determining them using numerical flow simulation. Grid-based simulation approaches are restricted to small sections of the screw and generally assume a fully filled domain. To overcome these limitations, the particle-based MPS method was introduced. Since this method had not been applied to the screw section of extruders before, the first step was to evaluate the effect of particle size on simulation outputs, such as residence time and degree of fill. Data on material parameters were taken from literature on a SPI dough with 55 wt% water. The results showed that particle sizes must be smaller than the gap between screw and barrel to obtain results independent of particle resolution. Based on this, simulations were performed for three kneading block configurations to determine local residence time, degree of fill, and shear rate distributions. The simulated fill levels were compared qualitatively with dead-stop experiments and showed good agreement in the kneading block. Finally, an extended simulation including the energy equation was carried out, demonstrating that a local temperature increase of more than 10 °C can occur in the kneading block, which is an effect not detectable experimentally.

To understand the extrusion process, it is essential not only to know the local process conditions but also how the material behaves under these conditions. Shear viscosity is the key material property describing this behavior. Although several methods exist to determine shear viscosity, none are suitable for protein doughs used in meat analogue production. These mixtures are highly viscoelastic, may undergo reactions at elevated temperatures, and can suffer from water loss or evaporation. The closed cavity rheometer (CCR) can overcome these limitations due to its sealed and pressurized measuring cavity, which enables rheological measurements at extrusion-relevant temperatures without water loss. The rheometer can perform a single controlled rotation within a defined time, the so called ramp test, which should provide access to shear viscosity at steady shear.

To verify the ramp test and assess the accuracy of the resulting shear viscosity data, three commercial polyolefin polymers were investigated in chapter 4: low density polyethylene, linear low density polyethylene, and polybutadiene. Their complex viscosities were measured and compared with shear viscosities obtained using a capillary rheometer and the CCR. Time temperature superposition master curves for the complex viscosity and the CCR-based shear viscosity were developed for linear low density polyethylene and polybutadiene. The influence of the cavity sealing on measurement accuracy was examined using finite element simulations, showing an effect of less than 12%. Overall, the results demonstrated that the ramp test performed with the CCR is a practical method for determining reliable and reproducible shear viscosity data across a temperature range from 50 to 180 °C and for materials covering viscosities from 1,600 to 480,000 Pa · s.

After validating the method with polymers, the ramp test was transferred to soy protein isolate dough with a water content of 55 wt% in chapter 5. Measurements were carried out at

temperatures from 95 to 140 °C. In parallel, the protein doughs were examined using a capillary rheometer to identify potential flow instabilities. However, the capillary rheometer data did not align with the ramp test results. The ramp test produced higher consistency indices (K = 3,412–32,237 Pa · s^n) and lower flow behavior indices (n = 0–0.43) compared to the uncorrected capillary rheometer data (K = 708–13,013 Pa · s^n, n = 0.10–0.48). Visual inspection revealed gel fracture at 95 °C and 110 °C, wall-slip effects, and browning at 140 °C, indicating protein reactions. Overall, chapter 5 presents two approaches for determining shear viscosity of protein douhgs at extrusion-relevant temperatures, identifies their limitations, and discusses how these observations may influence structure formation of meat analogues.

In chapter 6, the ramp test and MPS simulation were then applied to interpret observations made using the structure modulation method on SPI. When examining torque, die pressure, and material temperature, contradictory results were observed. The ramp test showed that lowering the pH increases shear viscosity, while increasing temperature decreases shear viscosity, which is consistent with complex viscosity measurements presented in chapter 2. However, these trends could not explain the unusual torque and pressure behavior. Using the MPS method with shear viscosity data from the ramp test for water-based dough and a pH-reduced dough at 140 °C revealed that the extruder operated at a very low degree of filling. Shear rate distributions remained unchanged, and residence times differed increased slightly with decreasing pH. These results suggest that the unexpected torque and pressure behavior is primarily caused by lubrication effects in the screw section and slippage in the die, rather than by changes in the local flow field. Under low filling conditions, the material temperature is dominated by heat exchange with the barrel rather than by viscous energy dissipation from mechanical input, which explains the nearly constant material temperature.

While the ramp test and MPS simulation helped interpret the observations made with the structure modulation method, each method also provides valuable insights on its own. The structure modulation method allows systematic adjustment of protein networks and targeted modification of meat analogue texture. The ramp test provides direct access to shear viscosity at extrusion-relevant temperatures, supporting material characterization and model development. The MPS simulation approach enables realistic analysis of partially filled screw sections, offering insight into local processing conditions.

Together, these methods contribute to a deeper mechanistic understanding of plant protein extrusion and provide a foundation for more targeted and efficient product and process design.

Zusammenfassung

Begleitet von umfangreichen Forschungsarbeiten haben Fleischersatzprodukte in den vergangenen Jahren zunehmend an Bedeutung gewonnen und sich von Nischenprodukten zu beliebten Optionen für Flexitarier entwickelt. Um ihre Attraktivität weiter zu steigern, ist eine kontinuierliche Produktentwicklung erforderlich. Dies umfasst sowohl die Verbesserung sensorischer Eigenschaften, wie Geschmack und Textur, als die Verwendung einer vielseitigeren Rohstoffpalette. Das Erfüllen dieser Anforderungen setzt ein mechanistisches Prozessverständnis voraus, um eine gezielte Produktgestaltung zu ermöglichen, anstatt sich auf Trial-and-Error oder Erfahrungswissen zu verlassen.

Der Doppelschneckenextrusionsprozess stellt die zentrale Technologie für die Herstellung von Fleischersatzprodukten dar. Trotz umfangreicher Forschung ist das mechanistische Verständnis, das für eine gezielte Produktgestaltung notwendig ist, noch unvollständig. Insbesondere das Zusammenspiel zwischen lokalen Prozessbedingungen und der resultierenden Struktur ist bislang nicht vollständig geklärt. Ein Grund hierfür ist die begrenzte Verfügbarkeit geeigneter Methoden, die sowohl den Prozess als auch die Materialeigenschaften unter extrusionsrelevanten Bedingungen untersuchen können.

Diese Dissertation verkleinert diese Lücke, indem drei komplementäre Methoden eingesetzt werden, um lokale Prozessbedingungen mit dem Materialverhalten während der Extrusion zu verknüpfen: die Strukturmodulationsmethode, der Rampentest und die Moving-Particle-Semi-Implicit (MPS) Simulationsmethode.

Zur Untersuchung des komplexen Extrusionsprozesses, der zahlreiche varierbare Parameter umfasst, welche sowohl die Prozessbedingungen als auch die Produkteigenschaften beeinflussen, war ein Modellprozess erforderlich, mit dem reproduzierbare Modellprodukte erzeugt werden können. Der erste Schritt bestand daher darin, eine Methode zu etablieren, die eine gezielte Veränderung der Endproduktstruktur ermöglicht, ohne die Prozessparameter oder die Proteinquelle zu verändern. Diese Anforderung wird durch die in Kapitel 2 vorgestellte Strukturmodulationsmethode erfüllt. Dabei wird der pH-Wert der flüssigen Phase systematisch durch Zugabe von Säuren abgesenkt. Da bekannt ist, dass pH-Änderungen die Oberflächenladung von Proteinen beeinflussen und damit deren Faltung sowie intermolekulare Wechselwirkungen verändern, wurde erwartet, dass die pH-Anpassung die Netzwerkbildung während der Extrusion beeinflusst und somit die Produktstruktur modifiziert. Materialutnersuchungen von Sojaproteinisolat- (SPI) und Weizengluten-Teigen in einem Closed Cavity Rheometer bestätigten diese Erwartung. Eine pH-Absenkung erhöhte die komplexe Viskosität von SPI, während

Gluten ein verändertes Reaktionsverhalten zeigte. Extrusionsversuche spiegelten diese Ergebnisse wider. Mit sinkendem pH-Wert wurden SPI-Extrudate dichter und spröder, während Glutenextrudate elastischer und teigartiger wurden. Mechanische- und Löslichkeitsanalysen zeigten zudem, dass SPI eine höhere Dichte physikalischer Wechselwirkungen bildete, während Gluten weniger Disulfidbrücken ausbildete. Auf Basis dieser Ergebnisse wurde SPI, verarbeitet mit der Strukturmodulationsmethode, als Modellsystem für die Arbeit ausgewählt, da es eine kontrollierbare Produktvielfalt für systematische Untersuchungen bereitstellte.

Für ein mechanistisches Verständnis des Extrusionsprozesses müssen auch die lokalen Prozessbedingungen bekannt sein. Da diese Bedingungen die Produkteigenschaften stark beeinflussen, aber experimentell nur begrenzt zugänglich sind, wird in Kapitel 3 eine Methode vorgestellt, die diese Bedingungen mittels numerischer Strömungssimulation bestimmt. Gitterbasierte Simulationsansätze sind auf kleine Schneckenabschnitte beschränkt und setzen typischerweise ein vollständig gefülltes Rechengebiet vorraus. Zur Überwindung dieser Einschränkungen wurde die partikeldiskrete Moving-Particle-Semi-Implicit (MPS) Methode eingeführt. Da diese Methode bisher nicht für den Schneckenbereich von Extrudern angewendet wurde, bestand der erste Schritt darin, den Einfluss der Partikelgröße auf Simulationsergebnisse wie Verweilzeit und Füllgrad zu untersuchen. Materialeigenschaften wurden aus Literaturdaten für einen SPI-Teig mit 55 wt% Wasser entnommen. Die Ergebnisse zeigten, dass die Partikelgröße kleiner sein muss als der Spalt zwischen Schnecke und Gehäuse, um partikelunabhängige Ergebnisse zu erhalten. Darauf aufbauend wurden Simulationen für drei Knetblockkonfigurationen durchgeführt, um lokale Verweilzeiten, Füllgrade und Scherratenverteilungen zu bestimmen. Die simulierten Füllgrade wurden qualitativ mit experimentellen Dead-Stop-Versuchen verglichen und zeigten im Bereich des Knetblocks eine gute Übereinstimmung. Abschließend wurde eine erweiterte Simulation unter Einbeziehung der Energiegleichung durchgeführt, die zeigte, dass lokale Temperaturerhöhungen von mehr als 10 °C im Knetblock auftreten können, ein Effekt, der experimentell nicht messbar wäre.

Für das Prozessverständnis ist es jedoch nicht nur entscheidend, die lokalen Prozessbedingungen zu kennen, sondern auch zu verstehen, wie sich das Material unter diesen Bedingungen verhält. Die Scherviskosität ist die zentrale Materialeigenschaft, die dieses Verhalten beschreibt. Obwohl verschiedene Methoden zur Bestimmung der Scherviskosität existieren, sind diese für proteinreiche Teige, wie sie bei der Herstellung von Fleischersatzprodukten eingesetzt werden, nicht geeignet. Diese Teige sind hoch viskoelastisch, können bei erhöhten Temperaturen reagieren und unterliegen Wasserverlust oder Verdampfung. Das Closed Cavity Rheometer (CCR) kann diese Herausforderungen durch seine geschlossene und druckbeaufschlagte Messkammer überwinden und ermöglicht somit rheologische Messungen unter extrusionsrelevanten Bedingungen ohne Wasserverlust. Das Gerät kann eine einzelne kontrollierte Rotation innerhalb einer definierten Zeit durchführen, den sogenannten Rampentest, der Zugang zur Scherviskosität unter stationärer Scherung ermöglichen sollte.

Zur Validierung des Rampentests und Bewertung der Genauigkeit der resultierenden Daten der Scherviskosität wurden in Kapitel 4 drei kommerzielle Polyolefinpolymere untersucht:

Polyethylen niedriger Dichte, lineares Polyethylen niedriger Dichte und Polybutadien. Ihre komplexen Viskositäten wurden gemessen und mit Scherviskositäten aus Kapillarrheometer und CCR verglichen. Für lineares Polyethylen niedriger Dichte und Polybutadien wurden Masterkurven mittels Zeit Temperatur Verschiebung für die komplexe Viskosität und die CCR-basierte Scherviskosität erstellt. Der Einfluss der Kammerabdichtung auf die Messgenauigkeit wurde mithilfe der Finite-Elemente-Methode numerisch untersucht und lag unter 12 %. Insgesamt zeigten die Ergebnisse, dass der Rampentest im CCR eine praxistaugliche Methode darstellt, um zuverlässige und reproduzierbare Scherviskositätsdaten im Temperaturbereich von 50 bis 180 °C und für Materialien mit Viskositäten von 1,600 bis 480,000 Pa · s zu erhalten.

Nach der Validierung der Methode wurde der Rampentest in Kapitel 5 auf SPI-Teig mit einem Wassergehalt von 55 wt% übertragen. Die Messungen erfolgten bei Temperaturen von 95 bis 140 °C. Parallel wurden die Proteiteige mit einem Kapillarrheometer untersucht, um mögliche Fließinstabilitäten zu identifizieren. Die Daten des Kapillarrheometers stimmten jedoch nicht mit den Ergebnissen des Rampentests überein. Der Rampentest lieferte höhere Konsistenzindizes (K = 3,412–32,237 Pa · s^n) und niedrigere Fließverhaltensindizes (n = 0–0.43) als die nicht korrigierten Kapillardaten (K = 708–13,013 Pa · s^n, n = 0.10–0.48). Visuelle Untersuchungen zeigten Gelbrüche bei 95 °C und 110 °C, Wandgleiten sowie Bräunung bei 140 °C, was auf Proteinreaktionen hinweist. Insgesamt präsentiert Kapitel 5 zwei Ansätze zur Bestimmung der Scherviskosität von Proteinteigen unter extrusionsrelevanten Bedingungen, identifiziert deren Einschränkungen und diskutiert, wie diese Beobachtungen das Verständnis bei der Erzeugung von Fleischersatzprodukten beeinflussen können.

In Kapitel 6 wurden Rampentest und MPS-Simulation zur Interpretation des Extrusionsprozesses von SPI unter Verwendung der Strukturmodulationsmethode geingesetzt. Bei der Analyse von Drehmoment, Düsendruck und Materialtemperatur zeigten sich widersprüchliche Befunde. Der Rampentest zeigte, dass eine pH-Absenkung die Scherviskosität erhöht, während steigende Temperaturen die Scherviskosität verringern, was sich mit den Messungen komplexen Viskositätsdaten aus Kapitel 2 deckt. Diese Trends konnten jedoch die ungewöhnlichen Verläufe von Drehmoment und Druck nicht erklären. Die Anwendung der MPS-Methode unter Verwendung der Viskositätsdaten des Rampentests für eine wasserbasierte und eine pH-abgesenkte Masse bei 140 °C ergab, dass der Extruder mit einem sehr niedrigen Füllgrad betrieben wurde. Die Scherratenverteilung blieb unverändert und die Verweilzeit nahmen mit sinkendem pH leicht zu. Diese Ergebnisse deuten darauf hin, dass die unerwarteten Verläufe von Drehmoment und Druck hauptsächlich durch Schmier- und Gleitfeffekte im Schneckenbereich und der Düse verursacht werden und weniger durch Änderungen im lokalen Strömungsfeld. Bei geringem Füllgrad wird die Materialtemperatur hauptsächlich durch den Wärmeaustausch mit dem Gehäuse bestimmt, während die viskose Wärmeentwicklung durch mechanische Energieeinträge eine untergeordnete Rolle spielt.

Während Rampentest und MPS-Simulation halfen, die Beobachtungen der Strukturmodulationsmethode zu interpretieren, liefern alle drei Methoden auch unabhängig voneinander wertvolle Erkenntnisse. Die Strukturmodulationsmethode ermöglicht eine systematische Anpassung von

Proteinnetzwerken und eine gezielte Modifikation der Textur von Fleischersatzprodukten. Der Rampentest bietet direkten Zugang zur Scherviskosität unter extrusionsrelevanten Bedingungen und unterstützt die Materialcharakterisierung. Die MPS-Simulation ermöglicht eine realistische Analyse teilgefüllter Schneckenbereiche und liefert Einblicke in lokale Prozessbedingungen.

Zusammen tragen diese Methoden zu einem tieferen mechanistischen Verständnis der Extrusion pflanzlicher Proteine bei und bilden eine Grundlage für eine gezieltere und effizientere Produkt- und Prozessgestaltung.

Nomenclature

Acronyms and abbreviations

1D	One Dimensional
3D	Three Dimensional
AC	Acetic Acid
B2B	Business to Business
BSA	Bovine Serum Albumin
CCR	Closed Cavity Rheometer
CFD	Computational Fluid Dynamics
CT	Citric Acid
DEM	Discrete Element Method
FEM	Finite Element Method
HMMA	High-Moisture Meat Analogue
IEP	Iso Electric Point
LDPE	Low Density Polyethylene
LLDPE	Linear Low Density Polyethylene
LED	Light-Emitting Diode
LMTVP	Low Moisture Texturized Vegetable Protein
LVE	Linear Visco-Elastic
MPS	Moving Particle Semi-Implicit
PBD	Polybutadiene
PE	Polyethylene
RAM	Random-Access Memory
RPA	Rubber Process Analyzer
RTD	Residence Time Distribution

SAOS	Small Amplitude Oscillatory Shear
SDS	Sodium Dodecyl Sulfat
SEC	Size Exclusion Chromatography
SME	Specific Mechanical Energy Input
SPH	Smoothed Particle Hydrodynamics
SPI	Soy Protein Isolate
TTS	Time Temperature Superposition

Constants

g	Gravity: 9.81 m/s
R	Gas constant: 8.314 J/mol*K

Latin symbols

A	Surface area
a	Horizontal shifting factor
b	Vertical shifting factor
C	Constant, Center Distance, Courant Number
D	Diameter
$\mathscr{D}$	Deformation tensor
d	Diameter
E	Young's modulus, Energy
e	Energy
F	Force
f	Frequency, Degree of fill
$\mathbf{f}$	Body force
G	Modulus
H	Height
K	Consistency index
L	Length
l	Length

M	Motor torque, Molar mass
$\dot{m}$	Mass flow rate
N	Number
n	Screw speed, Flow behavior, Particle number density
P	Motor power
p	Pressure
Q	Cumulative Distribution, Volumetric flow rate
$\mathbf{q}$	Heat flux
$\dot{q}$	Specific heat source
r	Radius
T	Temperature
t	Time
V	Volume
$\mathbf{v}$	Velocity
W	Width
w	Kernel function

Greek symbols

α	Compressibility coefficient, Arrhenius factor
β	Parameter pressure stabilization model
ε	Strain
γ	Strain, Parameter pressure stabilization model
$\dot{\gamma}$	Shear rate
η	Shear viscosity
$\lvert\eta^*\rvert$	Complex viscosity
λ	Thermal conductivity, Relaxation coefficient
ν	Kinematic viscosity
ρ	Density
σ	Compression stress, Shear stress
τ	Shear stress

τ	Stress tensor
θ	Angle
ω	Angular frequency

Operators and mathematical expressions

a^T	Transpose of vector a
a	Vector a
$\dashv$	Tensor a
Δ	Delta, Difference
$\frac{D}{Da}$	Lagrangian derivative with respect to a
$\frac{\partial}{\partial a}$	Partial derivative with respect to a
∇	Gradient
∇a	Divergence of vector a
$\sum_{j \neq i} a_j$	Sum of all terms a_j except a_i

Subscripts and superscripts

$*$	Temporary time step, Complex
$'$	Storage
$''$	Loss
0	Zero value, Initial State, Numerical
1	Number for a constant, Number for a barrel segment
2	Number for a constant, Number for a barrel segment
3	Number for a constant, Number for a barrel segment
4	Number for a barrel segment
5	Number for a barrel segment
6	Number for a barrel segment
7	Number for a barrel segment
8	Number for a barrel segment
$50,0$	50th percentile of the 0th (numerical) distribution
$Adapter$	Adapter

a	Activation
app	Apparent
ave	Average
$Bagley$	Bagley corrected
Die	Die
e	Effective action
end	End
i	Inner
$idle$	Idle value
in	In
$infty$	Infinity value
k	Current time step
L	Liquid
$Material$	Material
max	Maximum value
n	Number average
O	Outer
out	Out
p	Protein, Particle, Structural Breakdown
$prim$	Primitive
R	Relaxation coefficient
ref	Reference
RTD	Residence Time Distribution
T	Temperature
w	Weight average, Wall

1 General Introduction

1.1 Motivation

Over the past decade, meat analogues have gained significant attention. Initially regarded as niche products for vegans and vegetarians, they have now become common items on supermarket shelves and in refrigerated sections. Today, they are primarily purchased by flexitarians (Bundesminisrium für Ernährung und Landwirtschaft, 2024). As with many emerging innovations, an initial increase in interest led to a rapid increase in the number of new products seeking to take advantage of the trend. Over time, only brands delivering satisfactory sensory and nutritional quality have established themselves, while others have disappeared from the market.

To further strengthen the role of meat analogues in flexitarian diets, continued product improvement is essential. Consumer acceptance still depends largely on texture and taste, but increasing attention is also being paid to diversifying the protein sources used (Manjunhata Prabhu and Shanthala, 2025; Baig et al., 2025). Meeting these demands requires targeted product design. Purely empirical, trial-and-error approaches are time-consuming and costly. They also provide limited insight into transferable process-structure functions. Furthermore, conventional knowledge derived from these approaches is often inadequate because different protein sources have unique functional and processing properties. This limits the applicability of this knowledge to different materials and processing conditions.

Twin-screw extrusion processing of plant proteins is the key technology for producing meat analogues. This technology represents a highly coupled, nonlinear process in which thermal, mechanical, and physicochemical phenomena interact strongly and evolve locally and dynamically along the extruder. These interactions result in continuous changes to the material's state and structure. This makes intuitive and empirical product development approaches difficult and often unreliable. Despite extensive research in this field, a complete mechanistic understanding required for targeted product design remains incomplete. In particular, the interplay between process conditions and structure (process–structure function) and between structure and product properties (structure–property function) is not yet fully understood.

One reason for this knowledge gap is the limited availability of methods that can be used to establish a mechanistic understanding of extrusion processing. This is where the present thesis contributes. This introductory chapter first provides an overview of twin-screw extrusion of plant proteins. It then presents experimental and numerical approaches for investigating process conditions, as well as modeling techniques that mimic the screw section of an extruder. In addition, the fundamentals and methods for determining steady-state shear viscosity as an important material property that describes the flow behavior relevant for extrusion are presented. Finally, the chapter concludes with the objectives and outline of the thesis.

1.2 Structuring of meat analogues via twin-screw extrusion of plant proteins

1.2.1 Background

Plant proteins

Plant proteins are biomolecules composed of amino acids. Peptide bonds between the amino and carboxyl groups of two amino acids lead to the formation of linear polymers. The structure and functional properties of a protein can differ greatly depending on the functional groups of the amino acids (Nakai, 1983). The structure can be divided into four hierarchical levels and is illustrated schematically in figure 1.1. The primary structure describes the linear sequence of the amino acids linked by peptide bonds. The secondary structure describes local folding patterns, such as α-helices and β-sheets, which are stabilized by hydrogen bonds. The tertiary structure describes the protein's three-dimensional folding, which is influenced by intramolecular interactions such as hydrophobic forces, ionic bonds, and disulfide bonds. Finally, the quaternary structure arises when several polypeptide chains assemble into a three-dimensional complex through intermolecular forces, similar to those stabilizing the tertiary structure. (Belitz et al., 2001)

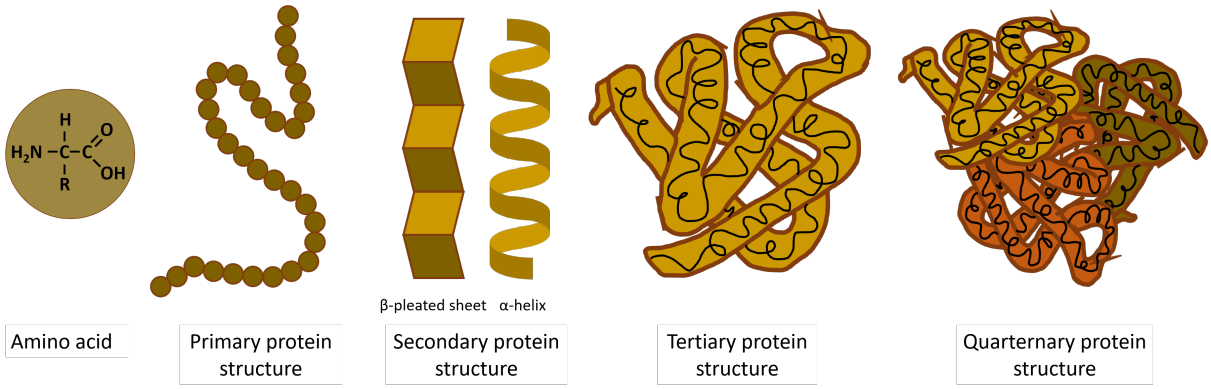

Figure 1.1: Schematc illustration of hierarchical structure of proteins

To targetly structure foods based on proteins, aggregation or gelation of the proteins is often used. Aggregation and gelation result from a change in the secondary, tertiary and quaternary structure of the proteins and depend on intrinsic factors (i.e. amino acid composition) and extrinsic factors (i.e. pH, ionic strength, temperature, shear) (Totosaus et al., 2002). For aggregation or gel formation to occur, the proteins must first be denatured by physical (shear, temperature, ...) or chemical influences (pH, enzymes, ...). During this process, the protein loses its three-dimensional structure and side groups are exposed, allowing them to interact and react with the side groups of neighboring proteins. This initially results in protein aggregates. If the protein concentration is sufficient, further networks (gels) can form which bind solvents and occupy the entire volume. (Wong, 2018; Kinsella and Melachouris, 1976)

Soy protein isolate and wheat gluten are the two most commonly used raw materials for producing meat analogues. These materials differ in protein content and how they aggregate and form a gel. Soy protein isolate has a protein content of around 90 *wt%*, while gluten has a content of around 80 *wt%*. Soy protein forms aggregates via non-covalent interactions, whereas gluten forms disulfide bridges under extrusion conditions. (Fischer, 2004; Emin et al., 2017; Chen et al., 2011; Wittek et al., 2020)

Twin-screw extrusion to produce meat analogues

The twin-screw extrusion process is flexible, continuous, cost-efficient and energy-efficient, and can be used to structure foods (Schuchmann, 2008; Bouvier and Campanella, 2014). Figure 1.2 shows a schematic illustration of a co-rotating twin-screw extruder used for processing proteins, particularly for producing meat analogues. The heart piece of the extruder are the pair of intermeshing screws within a barrel. The barrel consists of different segments, each of which has its own temperature control. The screws consist of screw elements, the two most important of which are conveying elements and kneading discs. Protein or protein rich blends are often fed into the screw section via gravimetric or volumetric powder feeding. Liquids such as water, emulsions or acids are then added by a liquid pump.

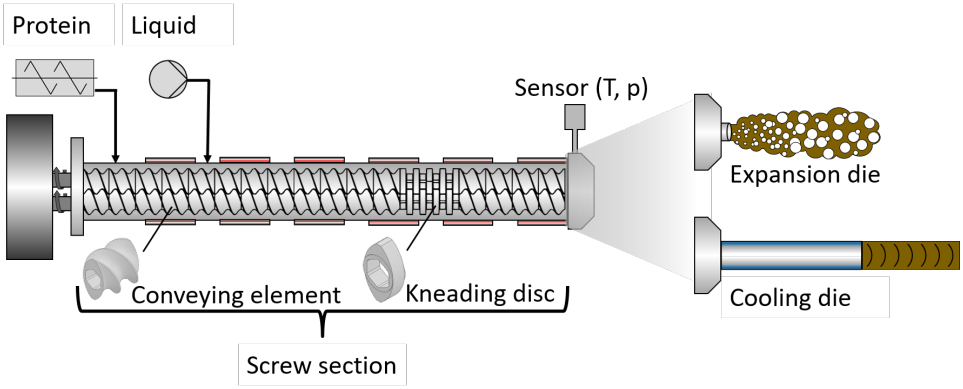

Figure 1.2: Schematic illustration of a twin-screw extruder used for production of meat analogues

In the screw section, various basic process operations, such as conveying, heating, mixing, plasticizing and cooking take place (Kohlgrüber, 2019; Bouvier and Campanella, 2014). For proteins, and protein rich blends, the powder is conveyed and mixed with the liquid, thereby plasticizing it. The resulting dough is then conveyed further, heated and sheared, which further homogenizes it and allows the proteins to denature and aggregate (Camire, 1991; Koch et al., 2017a; Emin et al., 2017; Pietsch et al., 2019c). At the end of the screw section is the die adapter, where a temperature and pressure sensor are usually mounted. The die attatched on the adapter is either a short expansion die or a long cooling die, depending on whether low-moisture texturized vegetable proteins (LMTVP) or high-moisture meat analogues (HMMA) are being produced. The expansion die is used for producing LMTVP and the cooling die for producing HMMA. LMTVPs are typically produced for the B2B market as they require rehydration, flavouring and shaping to produce items such as burger patties. In contrast, HMMAs deliver larger ready-to-eat products, such as vegetarian schnitzel or chicken chunks. The production of LMTVPs and

HMMAs differs not only in the die used, but also in the processing conditions and formulation. LMTVPs are produced at water contents below 30 wt% and temperatures above 150 °C, while HMMAs are produced at water contents above 50 wt% and temperatures between 130 and 150 °C (De Angelis et al., 2024).

Structure formation of LMTVPs and HMMAs

The structuring mechanisms that lead to LMTVPs and HMMAs being used as meat substitutes differ significantly. In both cases, the denaturation of proteins due to thermal and mechanical stress in the screw section of the extruder is important because it weakens the intramolecular and intermolecular interactions between protein molecules and allows new interactions to form, which is necessary for further structuring (Camire, 1991).

For the LMTVPs, the crucial structuring step is expansion within and immediately after the die. Due to the die channel's cross-sectional narrowing, pressure builds up in front of the expansion die. Despite the high temperatures, this keeps the vapor pressure of the protein-rich dough above the boiling point of water. In the die, or latest upon exiting it, the pressure drops below the vapor pressure. This causes abrupt water evaporation and bubble formation, which expands the extrudate. For LMTVPs, this expansion step is influencing product properties such as structure, hardness, porosity and rehydration behavior (Webb et al., 2020, 2023; Van Esbroeck et al., 2024). Before expansion, the proteins have been denatured by shear and heat in the barrel, allowing them to form new intermolecular bonds (Camire, 1991). These proteins can interact through disulfide, hydrophobic, and hydrogen bonding to build an elastic network that resists tearing despite swelling from water vapor. Thus, they create the favoured porous, elastic structure. As the extrudate cools under ambient conditions, the protein network solidifies and shrinks until the temperature falls below the glass transition temperature. At this point, the final structure is fixed (Kaletunç and Breslauer, 1996).

For HMMAs, it is assumed that structuring mainly takes place in the die adapter and the cooling die (van der Sman and van der Goot, 2023; Wittek et al., 2021a). Several hypotheses have been proposed, the most prominent being orientation within the flow profile and the formation of a multi-phase system. The two hypotheses are schematically shown in figure 1.3.

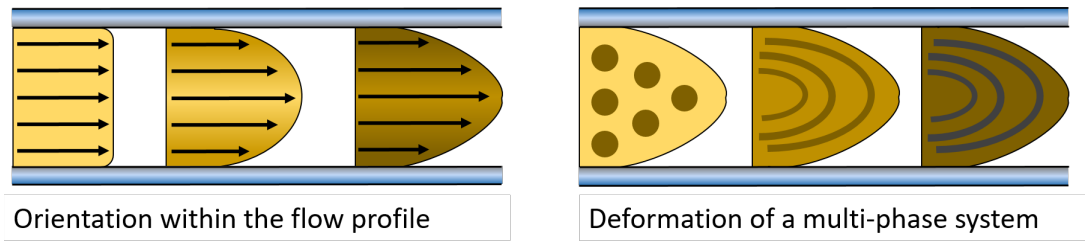

Figure 1.3: Schematic illustration of structure formation of high-moisture meat analogues

According to the orientation hypothesis, the proteins enter the die adapter in a denatured state. As they pass through the die, the proteins align with the flow profile, form new bonds and

solidify as they cool down (Arêas, 1992; Cheftel et al., 1992; Akdogan, 1999). The flow profile is often compared to Hagen–Poiseuille flow, which is characterized by a parabolic velocity distribution (Wittek et al., 2021d). This hypothesis therefore relies on the assumptions that denaturation is already complete before entering the die adapter, that alignment is mainly induced by die flow, and that the material behaves as a viscoelastic melt during processing.

The second hypothesis states that a multiphase system is formed through phase separation of various components, such as proteins and polysaccharides (Tolstoguzov, 1993). Wittek et al. (2021d) stated that phase separation into protein-rich and water-rich domains can happen. However, phase separation has primarily been demonstrated with soy protein isolate, and its occurrence with other protein sources is uncertain. Furthermore, phase separation is kinetically limited during extrusion due to short residence times and high viscosity. These factors restrict diffusion and may prevent the formation of equilibrium phase domains. This multi-phase system is then oriented by the flow within the die adapter and cooling die.

Other hypotheses propose that syneresis in the cooling die modifies the multi-phase system, and that solidification during cooling contributes to the final structure (van der Sman and van der Goot, 2023). Flow instabilities, such as melt fracture, are also said to play a role in the formation of fibrous structures (Guan et al., 2024). These hypotheses are not mutually exclusive and may occur simultaneously on different length and time scales. They remain largely qualitative, though, and are difficult to resolve experimentally. Therefore, their relative importance in real extrusion processes is unclear.

1.2.2 Methods of structure modulation of meat analogues

Although the structuring mechanisms are not fully understood, it is well established that the structure of proteins, and consequently meat analogues, can be modified through process-, material-, and chemical environment-driven modifications.

Process-driven modifications include more than just adjusting the water content when switching between LMTVP and HMMA. This approach involves adjusting the screw design and rotational speed, altering the mass flow rate, and controlling the barrel temperature profile (Pietsch et al., 2019b,a, 2017; Wittek et al., 2021a). The design of the die and the temperature profile in the cooling die also play crucial roles in controlling protein alignment and network formation (Guyony et al., 2022; Choi et al., 2025). These processing parameters influence local processing conditions, which will be explained further in the following chapter. Changes in processing conditions alter protein denaturation and aggregation, determining how the protein network develops during extrusion.

Material-driven modifications can be achieved by varying the protein source or processing blends of different proteins (Wittek et al., 2021b). Additionally, components such as polysaccharides (e.g. starch), oil or dietary fibers (e.g. pectin) can be added. According to Dickinson's classification (Chen and Dickinson, 1999), these components can act as active or inactive fillers or form an additional phase within the protein network (McClements, 2024). For example, Wittek et al. (2021b) showed, that adding whey protein isolate to soy protein isolate resulted in a more pronounced formation of anistropic fibers in high-moisture meat analogues. This was attributed to the additional protein phase that was introduced by the whey protein. Taghian Dinani et al. (2023) showed, that adding several hydrocolloids improved the mechanical anisotropy index. The addition of components affect the rheology, phase behavior, and texture of the extrudate. They also influence how proteins interact, align, and cross-link during extrusion (Kyriakopoulou et al., 2021).

Chemical modifications involve altering the protein network by changing its chemical environment. One way to achieve this is by adjusting the pH, which affects protein charge and influences the formation of the three-dimensional network (Nisov et al., 2022). Additionally, changes in pH result in changes in protein solubility (Totosaus et al., 2002). At the isoelectric point (IEP), more aggregation occurs due to hydrophobic interactions. However, a pH shift above the IEP results in increased electrostatic repulsion, leading to less aggregation (Totosaus et al., 2002). Molecules that act as physical or chemical cross-linkers can be added to promote new interactions between protein chains. In addition, salts and changes in ionic strength modify protein-protein interactions. Enzymatic activity can be exploited to selectively cut or link proteins. Together, these chemical factors influence protein denaturation, alignment, and cross-linking during extrusion, thereby determining the formation of the network structure and texture (Totosaus et al., 2002).

1.3 Process conditions in the screw section

1.3.1 Background

The twin-screw extrusion process is flexible and versatile process. As mentioned above, ground operations involve conveying, mixing, shearing, heating, cooking, and building pressure to push the material through a die. During process development, various process parameters must be defined, including screw speed, barrel temperature, and mass flow rates to achieve desired processing conditions and product properties (Kohlgrüber, 2019; Bouvier and Campanella, 2014).

Achieving the desired process conditions is possible by adjusting various processing parameters. An overview of the key processing parameters, processing conditions, and resulting product properties is shown in figure 1.4. For instance, the material temperature can be increased by modifying the screw configuration. However, it should be noted that such a change also affects many other processing conditions, as illustrated in figure 1.4. Furthermore, altering a single processing condition can influence several product properties. In addition to this complex interplay, the process is often referred to as a "black box" because many important local variables inside the extruder are difficult to measure directly. This complicates mechanistic understanding of the process and product design.

The important process conditions for process driven structure modulation of meat analogues are primarily residence time and temperature, as protein denaturation, aggregation, and network formation depend on them (Pietsch et al., 2017, 2019a,b). Table 1.1 illustrates the impact of an increase of various processing parameters on the residence time and temperature. In addition to these two processing conditions, mechanical stress also influences protein denaturation and network formation (Spiegel and Huss, 2002). It arises mainly from shear and elongational deformation within the screw section and contributes to the unfolding and alignment of protein chains.

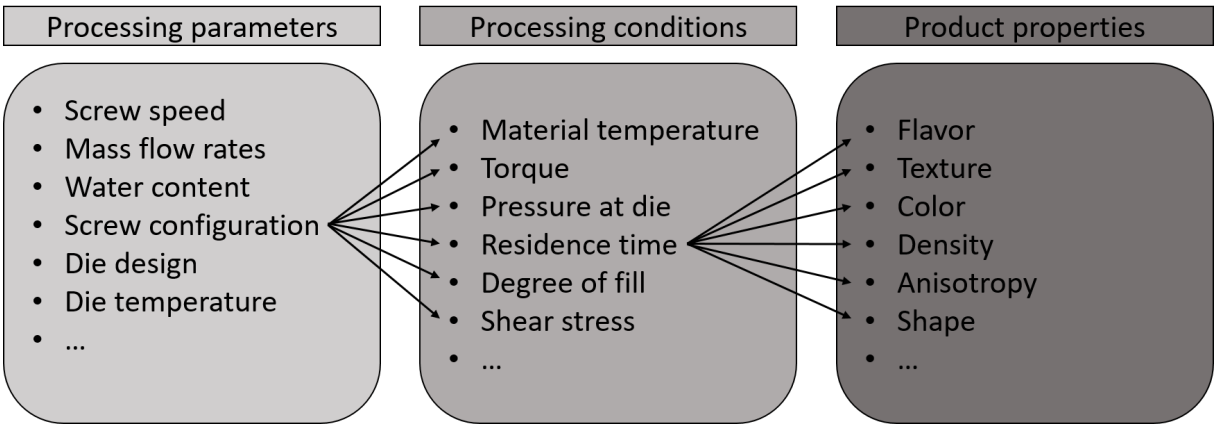

Figure 1.4: Schematic illustration of structure formation of meat analogues adapted and modified from Emin and Schuchmann (2017)

To monitor and control the thermal and mechanical stress in the extrusion process, only a limited number of control parameters are available. Typically, the barrel temperature, the temperature and pressure of the material in the die adapter, and the torque of the motor are monitored (van Lengerich, 1990; Rauwendaal, 2014; Martin, 2016). These parameters reflect the overall, integral stress history within the screw section. However, for understanding protein structuring and network formation, knowledge of the local processing conditions, particularly the true time–temperature history, is crucial (Van Den Einde et al., 2004; Pietsch et al., 2019c).

Table 1.1: Expected changes (increase ($\nearrow$), decrease ($\searrow$), unchanged ($\rightarrow$)), unknown (?) in material temperature and residence time when increasing ($\uparrow$) process parameters during the extrusion of non-reactive proteins.

	screw speed ↑	mass flow rate ↑	barrel temperature ↑	water content ↑
material temperature	$\nearrow$	$\searrow$	$\nearrow$	$\searrow$
residence time	$\searrow$	$\searrow$	$\rightarrow$	?

Due to the complexity of the process and the limited number of control parameters, it is understandable that targeted product design is difficult and often based on trial and error or experience. To overcome this and to enable a more systematic selection of extrusion parameters, more advanced monitoring techniques are required to generate a mechanistic process understanding.

Several experimental, numerical, and modeling approaches have therefore been developed to improve the mechanistic understanding of the extrusion process and to reduce reliance on empirical optimization.

1.3.2 Experimental methods for investigating processing conditions

The specific mechanical energy input (SME) is the most common key figure and is often used to describe the mechanical stress transferred into the material in the screw section (Meuser et al., 1984). It is calculated according to equation 1.1, where $M - M_{idle}$ is the torque of the motor corrected by the idle torque, $\dot{m}$ the mass flow, n the screw speed, n_{max} the maximum screw speed, and P_{max} the maximum power of the motor.

$$SME = \frac{\frac{n}{n_{max}} \cdot \frac{M - M_{idle}}{100}}{\dot{m}} \cdot P_{max} \tag{1.1}$$

SME is often used to compare different processing parameters and is sometimes correlated with product properties (Pietsch et al., 2019b; Schmid et al., 2022). However, it only provides an integral value for the entire process and does not provide information about the local energy input

along the screws, which can play a decisive role (Van Der Goot et al., 2008; Emin and Schuchmann, 2013). Another non-integral method that provides information about shear stress is using encapsulated dye tracers (Pappas et al., 2012; Fukuda et al., 2015). The stress at which the capsule breaks and releases the tracer can be controlled by adjusting the hardness through particle diameter and capsule wall thickness. By measuring encapsulated dye tracers of different hardness levels and comparing the released dye to the added dye, it is possible to obtain information about maximum shear stress and how much of the fluid is experiencing this maximum shear stress.

Thermal stress can be measured by mounting a temperature sensor in the die adapter to measure the temperature of the material (Abeykoon et al., 2012; Martin, 2016). As for the SME, this material temperature only provides information about the integral thermal stress. To obtain temperature information along the screw section of the extruder, temperature sensors can be mounted in ports along the barrel. However, temperature measurements are affected by the barrel's temperature and heat conduction. Therefore, they are not an accurate description of the temperature of the material in the screw section. Additionally, the sensor's response time is slow compared to the screw's rotation speed, resulting in an averaged temperature reading over time. Using infrared sensors can overcome these limitations, but calibration is material-dependent and time-consuming (Emin et al., 2016).

Tracer experiments can be performed to determine residence time (Leeb et al., 2008). A small amount of a detectable tracer is introduced into the feed, and its concentration is monitored at the die outlet over time. The resulting intensity versus time curve provides the residence time distribution (RTD), which depends on local flow velocities, back-mixing, and the degree of fill (Kohlgrüber, 2019). Parameters such as the mean residence time and degree of mixing can be derived from the RTD. While this method provides important residence time information, it does not indicate where materials reside along the screw or how long it remains there. This information is necessary for an accurate time-temperature description of the material. Two approaches can be used to obtain information about local residence time. One approach is to add the tracer at several positions in the barrel and measure the intensity at the die exit (Oberlehner et al., 1994). Alternatively, the tracer can be detected at several positions along the extruder (Zhang et al., 2006). Using a deconvolution of individual residence time distributions can yield local profiles (Calumby and Canevarolo, 2002).

To summarize, experimental investigations do not allow conclusions to be drawn about local process conditions, despite their great importance and potential role in structural changes (Emin and Schuchmann, 2013; Van Der Goot et al., 2008; Liu et al., 2010).

1.4 Numerical simulation of the process conditions inside the screw section

1.4.1 Background

Given the challenge of determining local processing conditions inside the extruder through experimentation alone, numerical simulations of the screw section offer valuable insight into the underlying local process mechanics (Schuchmann, 2008). According to Wittek and Emin (2017), various numerical approaches and modeling strategies have been developed over time to describe flow behavior in extrusion processes, ranging from simplified one-dimensional (1D) models to fully three-dimensional (3D) simulations based on finite element (FEM), or mesh-free smoothed particle hydrodynamics (SPH). There is a wide range of literature providing background information on computational fluid dynamics. In the following, the explanations are primarily based on Paschedag (2004), Monaghan (2005), and Versteeg and Malalasekera (2007). The above mentioned numerical methods differ in complexity and computational cost. Nonetheless, they all share the same approach. This approach involves solving the fundamental transport equations for mass (equation 1.2), energy (equation 1.3), and momentum (equation 1.4).

$$\frac{\partial \rho}{\partial t} + \nabla \cdot (\rho \mathbf{v}) = 0 \tag{1.2}$$

$$\frac{\partial (\rho \mathbf{v})}{\partial t} + \nabla \cdot (\rho \mathbf{v}\mathbf{v}) = -\nabla p + \nabla \cdot \tau + \rho \mathbf{f} \tag{1.3}$$

$$\frac{\partial (\rho e)}{\partial t} + \nabla \cdot (\rho e \mathbf{v}) = -\nabla \cdot (p\mathbf{v}) + \nabla \cdot (\tau \cdot \mathbf{v}) - \nabla \cdot \mathbf{q} + \rho \dot{q}. \tag{1.4}$$

Here, ρ is the fluid density, t the time, $\mathbf{v}$ the velocity vector, p the pressure, τ the viscous stress tensor, $\mathbf{f}$ the body force per unit mass, e the total energy per unit mass, $\mathbf{q}$ the heat flux vector, and $\rho \dot{q}$ the volumetric heat generation term.

To close the set of transport equations, a constitutive law describing the rheological behavior of the material is required. In its simplest form, for a Newtonian fluid, the stress tensor τ is proportional to the rate of deformation, and given by equation 1.5

$$\tau = 2\eta \mathscr{D} \tag{1.5}$$

with

$$\mathscr{D} = \frac{1}{2}(\nabla \mathbf{v} + \nabla \mathbf{v}^T) \tag{1.6}$$

where η is the shear viscosity and $\mathscr{D}$ is the rate-of-deformation tensor. The rheological behavior of protein doughs used in meat analogues typically exhibits non-Newtonian characteristics, which will be described in the next chapter.

To solve the governing transport equations and obtain information about the flow field in the screw section of the extruder, the flow domain must first be discretized in space and time. Depending on the numerical approach chosen, this can be done in different ways, which vary in complexity, accuracy, and computational cost.

In 1D models, the flow within the screw section is simplified by averaging the geometry along the screw axis. The governing equations for mass, momentum, and energy conservation are then solved using analytical or semi-empirical correlations that account for conveying, pressure flow, leakage, and viscous dissipation (Vergnes et al., 1998).

In FEM simulations, the flow domain is discretized into a mesh of elements, and the transport equations are solved numerically for each element. The coupled, nonlinear system of equations is iteratively solved until convergence is achieved. However, since the geometry of twin-screw extruders changes continuously due to screw rotation and intermeshing, additional techniques must be employed to accurately represent the moving boundaries.

In the SPH method, the fluid is represented by a set of discrete particles instead of a mesh. Each particle carries physical properties such as mass, velocity, and temperature, and interacts with neighboring particles through a kernel function that defines the spatial extent of the interactions. The governing equations are then solved in a Lagrangian framework, meaning that the particles move with the flow. This makes SPH particularly suitable for complex, transient geometries and free-surface flows, as no mesh deformation or remeshing is required.

1.4.2 Numerical methods for simulation of the screw section

Ludovic® can be used as commercial software for performing 1D twin-screw extrusion simulations (Vergnes et al., 1998). Required parameters include the extruder geometry and the material properties, such as heat capacity, density, thermal conductivity, and shear viscosity. The operating conditions must also be specified, e.g. screw speed, barrel temperature profile, and feed rate. The main output parameters are material temperature, pressure, shear rate, filling ratio, and residence time (Durin et al., 2014; Kristiawan et al., 2022). These parameters are relevant for describing processing conditions when producing meat analogues. The main advantages of the approach in the Ludovic® software are its low computational cost and short calculation time compared to more complex 3D simulations. However, the model does not account for local variations along the screw elements and provides only averaged values for each element. Furthermore, it cannot fully capture the complex, time-dependent, or non-Newtonian rheological behavior of protein systems.

A three-dimensional simulation of the screw section can be done using Polyflow® software (Wittek and Emin, 2017). This finite element approach is more computationally expensive due to the mesh-based discretization of the flow domain and the iterative solution of the governing equations. To account for the rotation of the screws, the mesh-superposition technique is used. Here, the barrel is represented by a static mesh, while the screws are represented by a rotating mesh. At each time step, the two meshes are superimposed, and the solver determines for every fluid element whether it is occupied by the screw or available for flow. This allows the rotating, intermeshing screw geometry to be captured without the need for continuous remeshing (Avalosse, 1996; Avalosse and Rubin, 2000). Furthermore, the flow field can be solved over multiple time steps. This allows for the changing position of the screws during rotation to be taken into account. The same input data is required as for the 1D simulation, but temperature dependence can be included in the rheological behavior.

The additional modeling effort (3D, mesh rotation, temperature dependence of the rheological behavior) provides information about mechanical and thermal stresses, such as local temperature distributions. Moreover, 3D simulations can describe the mixing behavior within the screw section (Zhang et al., 2009; Sun et al., 2022). By tracking particle trajectories, also insight into the distribution of mechanical and thermal stresses can be obtained (Emin et al., 2021). While these simulations provide valuable insights into local processing conditions relevant to meat analogue extrusion, they are computationally demanding and are typically limited to small, representative screw sections. Additionally, the model assumes a completely filled flow domain, which does not always reflect actual operating conditions in experimental extrusion processes.

The limitation of assuming a fully-filled flow field can be overcome using a Lagrangian simulation approach. In this approach, the fluid is represented by a collection of moving particles rather than a fixed mesh. This allows for the natural representation of free surfaces and partially filled regions. However, approaches based on smoothed particle hydrodynamics (SPH) are still under development, and there is no commercial software that has established itself as the standard tool for twin-screw extrusion simulations. Pioneering studies by Eitzlmayr and Khinast (2015), Wittek et al. (2018), Bauer and Khinast (2022), and Bauer et al. (2022) have demonstrated the applicability of the SPH method to twin-screw extruders. This enables the investigation of local residence time distributions, mixing behavior, and flow characteristics. Furthermore, Meza Gonzalez and Nirschl (2023) showed that mechanical stresses, expressed as local shear rate distributions, can be evaluated using this approach as well. Although particle-based methods offer promising insights into local processing conditions, they have not yet been applied to non-Newtonian rheological behavior, and the energy balance is neglected. Another limitation is of computational nature. The particle sizes are often too large to adequately resolve narrow flow areas, such as the gap between the screw tips, the barrel, and the intermeshing screws. Reducing the particle size would increase computing time.

1.5 Mimicking the process conditions in the screw section

Experimental investigations and numerical simulations help characterize the mechanical and thermal stresses to which protein doughs are subjected in the screw section of an extruder. However, these methods do not allow for direct investigation of how the dough itself responds to these stresses. This response to stress, in turn, influences the local processing conditions.

The challenge in identifying a suitable method to study material response arises from two main factors. First, mechanical and thermal stresses must be decoupled. Second, the experimental conditions must reproduce conditions relevant to extrusion, particularly temperatures above 100 °C, while preventing water evaporation.

A suitable model system has been found in the Rubber Process Analyzer, which enables rheological measurements in a closed, pressurized cavity. This is why it is also called a closed cavity rheometer (CCR) (Emin et al., 2017). This setup prevents water loss while allowing independent control of time, temperature and shear, thereby providing conditions representative of thermomechanical extrusion processing.

Using this modeling technique, two complementary approaches can be followed. On the one hand, samples can be prepared with a well defined thermomechanical stress history. These samples can subsequently be used for further offline analyzes, for example of the degree of denaturation or aggregation (Koch et al., 2017b; Pietsch et al., 2019c; Quevedo et al., 2021b). Such analyses provide insights into ongoing reactions and reaction kinetics, which can be used to predict behavior under extrusion conditions. On the other hand, direct rheological measurements can yield valuable information about material properties and stress responses, including shear viscosity dependencies, reaction onset temperatures, gel strength, relaxation behavior, and reaction kinetics (Quevedo et al., 2020; Wittek et al., 2020; Quevedo et al., 2021b; Wittek et al., 2021c; Schreuders et al., 2021b). A limitation of this powerful tool is, that the applied shear deformation is oscillatory rather than steady. Consequently, the stress conditions are not directly transferable to those in the rotating screw, and both, the achievable shear rates and shear stress are typically one to two orders of magnitude lower.

1.6 Investigation of flow behavior under extrusion-relevant conditions

1.6.1 Background

The previous chapter introduced experimental and numerical methods for studying local processing conditions within the extruder. Additionally, it presented a modeling approach to investigate how the material responds to oscillatory thermomechanical stresses under conditions relevant to extrusion. However, since shear deformation in the screw section is predominantly steady rather than oscillatory, this approach cannot directly describe material flow through the extruder. This flow behavior is important for processing and texturing plant proteins, so there is a gap in the understanding of the process. The background given in this chapter, is taken, if not stated otherwise explicitly, from Steffe (1996).

To quantify flow behavior under steady deformation, the shear viscosity can be measured as a function of shear rate and temperature. The shear viscosity, $\eta(\dot{\gamma})$, is a fundamental rheological property that describes a material's resistance to flow under continuous shear. It is defined as the ratio of the applied shear stress τ, to the resulting shear rate, $\dot{\gamma}$:

$$\eta(\dot{\gamma}) = \frac{\tau}{\dot{\gamma}}. \tag{1.7}$$

In the simplest case of shear flow between a stationary and a moving plate, the shear stress represents the tangential force F required to move the plate with a given surface area A:

$$\tau = \frac{F}{A}. \tag{1.8}$$

The corresponding shear rate can be expressed as the ratio of the velocity difference v to the gap height H between the two parallel plates:

$$\dot{\gamma} = \frac{v}{H}. \tag{1.9}$$

The response of a material to different shear rates and temperatures is referred to as its flow behavior. If the shear viscosity is independent of the applied shear rate, the material exhibits Newtonian flow behavior. In contrast, when shear viscosity decreases with increasing shear rate, the material shows shear-thinning (pseudoplastic) behavior, while an increase in shear viscosity with shear rate is known as shear-thickening (dilatant) behavior.

Some fluids also exhibit a yield stress, meaning that a certain critical stress must be exceeded before flow begins. The simplest case is a Bingham plastic, which behaves as a rigid body below the yield stress and flows with constant shear viscosity once the yield stress is overcome.

To quantitatively describe the flow behavior of fluids, several empirical and semi-empirical models have been developed. Among the most widely used is the Herschel–Bulkley model. This model is capable of representing the different dependencies of shear stress on shear rate discussed above.

The general form of the Herschel–Bulkley model (Herschel and Bulkley, 1926) is given by equation 1.10, where τ_0 is the yield stress, K is the consistency index, and n is the flow behavior index:

$$\tau = \tau_0 + K\dot{\gamma}^n. \tag{1.10}$$

For materials that do not exhibit a yield stress ($\tau_0 = 0$), the model reduces to the Ostwald–de Waele model. A value of $n < 1$ describes shear-thinning behavior, $n = 1$ corresponds to Newtonian flow, and $n > 1$ represents shear-thickening behavior.

In addition to shear-rate dependence, the shear viscosity of some materials also changes with time at constant shear rate. For thixotropic fluids, the shear viscosity decreases over time under constant shear, while rheopectic fluids show the opposite behavior, with shear viscosity increasing over time.

Temperature also strongly influences shear viscosity. For non-reactive systems, an increase in temperature generally results in a decrease in shear viscosity due to enhanced molecular mobility and weakened intermolecular interactions that resist flow. This temperature dependence can often be described empirically by the Arrhenius equation:

$$\eta = \eta_0 \exp\left(\frac{E_a}{RT}\right), \tag{1.11}$$

where η_0 is the pre-exponential factor, E_a is the activation energy for flow, R is the universal gas constant, and T is the absolute temperature. Alternatively, near the glass transition region, the Williams–Landel–Ferry (WLF) (Williams et al., 1955) equation is often used:

$$\log\left(\frac{\eta}{\eta_{\text{ref}}}\right) = -\frac{C_1(T - T_{\text{ref}})}{C_2 + (T - T_{\text{ref}})}, \tag{1.12}$$

where η_{ref} is the shear viscosity at a reference temperature T_{ref}, and C_1 and C_2 are empirical constants.

In reactive systems, however, the situation is more complex. In addition to the effects of increased molecular mobility and weakened intermolecular interactions, chemical reactions such as polymerization, crosslinking, or degradation may occur simultaneously. These reactions can increase shear viscosity through molecular network formation or decrease it through chain scission. Thus, the temperature dependence of shear viscosity in reactive systems arises from the interplay of physical and chemical effects, making case-by-case evaluation necessary.

1.6.2 Methods for investigating flow behavior under extursion relevant conditions

To investigate how protein doughs respond under extrusion-relevant conditions, it is important to consider once again the processing conditions prevailing in the screw section of the extruder. During the production of meat analogues, residence times of about one minute, temperatures ranging from 25 °C to 160 °C without water evaporation, and shear rates of up to 5000 s^{-1} can occur (Emin and Schuchmann, 2017). Consequently, the instrument used to measure shear viscosity must meet several requirements. It should provide fast and accurate temperature control, prevent water loss during measurement, generate sufficiently high force or torque to handle highly concentrated protein doughs, and enable the performance of steady shear tests.

There are several options for investigating shear viscosity. Classical open-boundary rheometers are ideal for studying the shear viscosity of melts and liquids. However, they have several limitations, including relatively low torque capacity, wall slippage effects in highly viscoelastic samples, and water loss at elevated temperatures. Using a pressure cell can prevent water evaporation, but this approach is still under development and faces challenges related to torque limitations, temperature control, accurate sample positioning, and potential sample slippage (Sägesser et al., 2025). Another way to obtain information about shear viscosity with such devices is to perform measurements at lower temperatures and higher water contents, followed by extrapolation to extrusion-relevant conditions (van der Sman et al., 2024). However, it should be noted that protein systems behave differently at high concentrations than at low concentrations (Quevedo et al., 2021a). This is particularly relevant for extrusion processing.

Capillary rheometry is another technique for measuring highly viscous materials at elevated temperatures. These measurements can be taken in-line by placing a defined capillary at the end of the extruder to measure pressure loss or offline with a stand-alone capillary rheometer. In both cases, the force applied by the extruder or instrument is not the limiting factor. The main drawbacks are the time-consuming measurement procedure and high material consumption.

Several corrections are required to obtain the true shear viscosity, including the Bagley correction (Bagley, 1957), the Rabinowitsch–Weißenberg correction (Rabinowitsch, 1929), and

the Mooney correction (Mooney, 1931). For simplicity, these corrections can be neglected because the general trends and relative differences between samples remain comparable for corrected and uncorrected data van der Sman et al. (2024). Additional limitations of offline capillary rheometers include slow temperature control and an inability to apply defined mechanical stresses to samples. Despite these limitations, offline capillary rheometer tests have been conducted on soy protein isolate. These tests examined the dependence of shear viscostiy on temperature ranges up to 140 °C and water content between 17 and 70 *wt%*. Shear-thinning behavior with a yield point was measured and could be described using the Herschel-Bulkley model (Fujio et al., 1991; Hayashi et al., 1991). However, it was also shown that long measurement times in the capillary rheometer influence the results, presumably due to protein degradation (Hayashi et al., 1992). Inline capillary rheometers have the advantage of directly determining shear viscosity after processing in the extruder. However, it is not possible to directly determine flow curves of materials as variations in shear rates and temperatures can only be achieved by adjusting the processing conditions (Dalle Fratte et al., 2022). These adjustments would influence the shear viscosity again because the thermomechanical stress in the screw section would change.

The aforementioned closed-cavity rheometer provides processing conditions relevant to extrusion, including fast temperature control, high torque capacity, and prevention of water loss and wall slippage. Additionally, samples can undergo defined pre-treatments, enabling the investigation of flow behavior as a function of thermomechanical stress history. However, this instrument has primarily been used to measure the complex viscosity because it is designed mainly for oscillatory tests, and the cone's stationary rotation is limited to one rotation. One method of estimating shear viscosity from these measurements is to apply the Cox–Merz empirical rule (Cox and Merz, 1958), which posits that the magnitude of complex viscosity at a given angular frequency is equivalent to the shear viscosity at the equal shear rate. While this relationship holds for many polymer melts and solutions, it has been shown to be inapplicable to systems with strong molecular interactions, such as concentrated protein dispersions (Mezger, 2021). Nevertheless, Wittek et al. (2021a) used this relationship to investigate the angular frequency and temperature dependence of soy protein isolate. It was found that the complex viscosity of soy protein isolate decreases with increasing temperature, a phenomenon that they described using an Arrhenius approach. Complex viscosity also decreased with increasing angular frequency. This relationship was described using a Bird-Carreau model.

1.7 Objective and outline of this thesis

For the targeted design of meat analogues, it is essential to have a mechanistic understanding of the high-moisture twin screw extrusion process. It is mandatory to know the process-structure function and the structure-property function. Because there is still a knowledge gap regarding this topic, the goal of this thesis is to improve mechanistic understanding. Because methods for investigating processing conditions and material behavior under extrusion-relevant conditions are limited, this work presents, discusses, and applies new experimental and numerical approaches to meat analogues. Particular attention is paid to process-structure function, especially the local process conditions in the screw section of the extruder, as well as the flow behavior of protein doughs under these conditions. The structure of the thesis is illustrated schematically in figure 1.5.

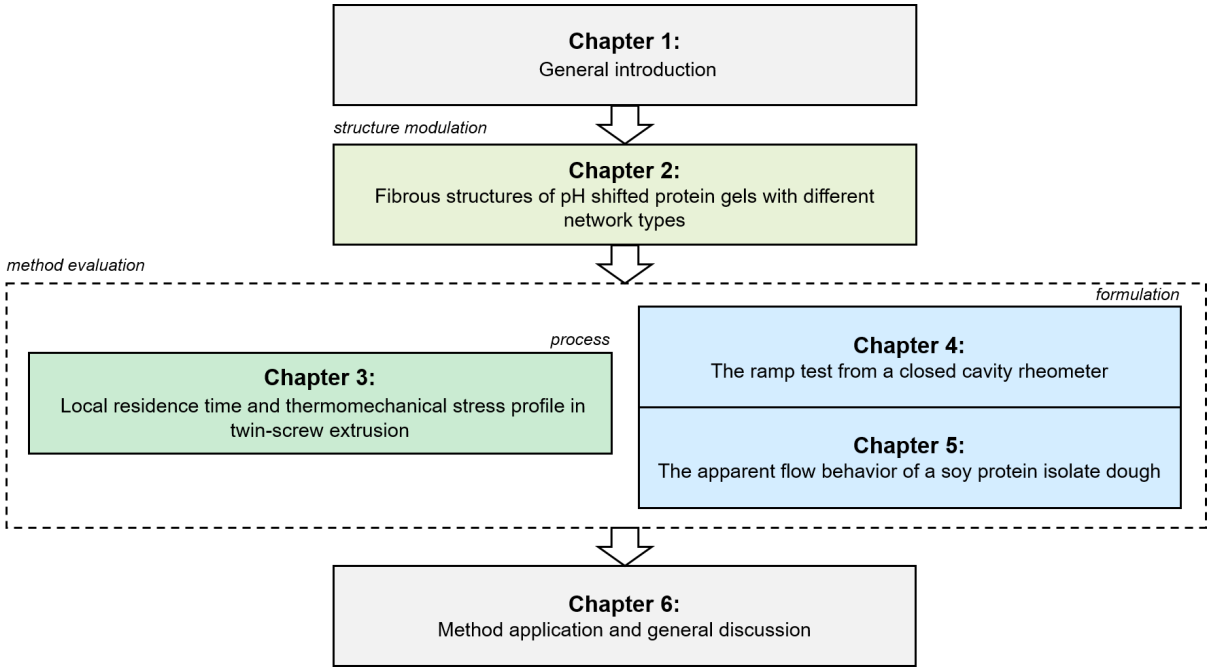

Figure 1.5: Schematic outline of the thesis.

To be able to test methods investigating local process conditions and material response, suitable model products are needed that allow observation of product property differences. Because changing a single process parameter affects many interrelated process conditions, which cannot be considered independently, model products are sought in which the process conditions remain constant. Furthermore, the protein source should not be changed, as different proteins exhibit distinct properties that strongly influence product characteristics.

Therefore, chapter 2 investigates a method of modifying the structure of high-moisture meat analogues by adjusting the pH and thereby altering the chemical environment. Soy protein isolate is examined as a representative protein forming physical gels, while wheat gluten represents proteins forming chemical gels. Doughs with reduced pH are produced for both protein sources, and rheological measurements are performed to study the effect of pH modification

on network formation. Furthermore, HMMAs with reduced pH are produced under constant process parameters. The resulting extrudates are analyzed optically, mechanically, and at the molecular level to relate macroscopic structure changes to molecular interactions. SPI-based HMMAs are selected as model products for further investigation because they exhibit limited time-temperature-dependent chemical reactions, such as degradation or new bond formation, under the chosen processing conditions.

To investigate if changes in local processing conditions may be the cause of changes in the product structure, a suitable method for determining local processing conditions is required. To this end, chapter 3 introduces a numerical approach based on the moving particle semi-implicit (MPS) simulation method. The MPS method was chosen because it enables the investigation of a large section of the screw section and does not require the common assumption of a fully filled extruder, which is often inaccurate. To establish the model, the influence of particle size on the local degree of fill and residence time is investigated. The numerical approach is then verified by comparing simulations for three kneading block configurations with experimental dead-stop data. The simulation results also provide information on local shear rate distributions, residence time distributions, and temperature profiles, offering new insights into local processing conditions during plant protein extrusion.

How the material behaves under these local conditions, particularly how it flows and moves through the extruder, can be understood once the material property of shear viscosity is known. This property is also one of the most critical input parameters for numerical simulation. Therefore, chapters 4 and 5 present, validate, and critically discuss the ramp test in a closed-cavity rheometer, a method developed to determine shear viscosity under extrusion-relevant conditions. In this test, the lower cone of a sealed cone–cone rheometer completes one rotation while the torque on the upper cone is measured. Since the rotational speed and measurement geometry are defined, the shear rate can be calculated from these parameters using standard assumptions for cone–cone rheometers. This allows for the calculation of shear viscosity.

Chapter 4 first applies this method to commercial polyolefin polymers, which are easier to characterize than protein doughs. The results are compared with those from a conventional capillary rheometer to demonstrate that both methods yield comparable shear viscosities. Additional measurements at different temperatures further demonstrate the method's relevance for extrusion processes.

Chapter 5 then applies the validated ramp test to SPI doughs at temperatures relevant for the production of high-moisture meat analogues. The results are compared with data obtained from capillary rheometry. Additionally, samples generated during the measurement procedure are visually examined and characterized, enabling a critical discussion of method-specific effects, the influence of temperature on apparent flow behavior, and implications for protein structuring potential.

Finally, chapter 6 highlights the need for methods capable of linking local process conditions with material properties. It demonstrates that conventional extrusion control parameters alone

are insufficient to describe the complex behavior inside the extruder. The new methods developed and validated in chapters 3 to 5 are applied to the SPI doughs used for the model HMMAs presented in chapter 2, allowing the explanation of previously unexplained phenomena in process monitoring. This chapter also discusses a potential side observation that could be exploited to assess the structuring ability of proteins. The thesis concludes with the main findings, limitations of the presented methods, and recommendations for future research.

2 Fibrous Structures of Protein Gels With Different Network Types

Chapter 2 is published as: F. Ellwanger, M. Fuhrmann, H.P. Karbstein, and G. I. Saavedra I. Influence of lowering the pH value on the generation of fibrous structures of protein gels with different network types. *Gels 10(3): 173* (2024). doi: 10.3390/gels10030173. Text, tables, figures and equations have been edited and reformatted for consistency.

Abstract

High-moisture extrusion of plant proteins to create meat-like structures is a process that has met with increasing attention in the recent past. In the process, the proteins are thermomechanically stressed in the screw section of the extruder, and the resulting protein gel is structured in the attached cooling die. Various protein sources, notably soy protein isolate (SPI) and wheat gluten, are used to form gels with different networks: SPI creates a physical, non-covalent network, while gluten forms a chemical, covalent one. The food industry frequently adds weak acids to modify taste and shelf life. However, it is known that a change in pH affects the gelation behavior of proteins because the repulsive forces within and between the proteins change. The research reported here was carried out to investigate for the two proteins mentioned the influence of pH modification by the addition of citric acid and acetic acid on gel formation and the meat-like structures produced. For this purpose, materials and parameters were screened using a closed cavity rheometer, followed by extrusion trials at pH 7.36–4.14 for SPI and pH 5.83–3.37 for gluten. The resulting extrudates were analyzed optically and mechanically, and protein solubility was tested in a reducing buffer. For both protein systems, the addition of acid results in less pronounced meat-like structures. At decreasing pH, the complex viscosity of SPI increases (from 11.970 Pa s to 40.480 Pa s at 100 °C, the generated gel becomes stronger (strain decreased from 0.62 to 0.48 at 4.5×10^5 Pa), and the cross-linking density grows. For gluten, a decreasing pH results in altered reaction kinetics, a more deformable resulting gel (strain increased from 0.7 to 0.95 at 4.5×10^5 Pa), and a decreased cross-linking density. Solubility tests show that no additional covalent bonds are formed with SPI. With gluten, however, the polymerization reaction is inhibited, and fewer disulfide bonds are formed.

2.1 Introduction

In recent years, meat substitutes have become increasingly popular. This may be due to consumers' increasing awareness of the ethical, environmental, and health impacts of meat consumption (Hallström et al., 2014; Apostolidis and McLeay, 2016). As plant-based protein sources, meat substitutes are supposed to represent a sustainable and healthy alternative to animal meat (Kumar et al., 2017). High-moisture extrusion is a common process for the production of such meat substitutes. In the high-moisture extrusion process, proteins are mixed with water and other ingredients, thermomechanically stressed in the screw section, and then pressed through a cooling die (Arêas, 1992; Cheftel et al., 1992). In the cooling die, anisotropic structures are generated that are supposed to imitate muscle meat (Beniwal et al., 2021). Various hypotheses have been proposed regarding the origin of these anisotropic, meat-like structures, with two being most widely accepted. Firstly, it is argued that proteins above the denaturation temperature align and rearrange within the shear flow in the cooling die. Upon cooling, the realigned protein gel solidifies (Akdogan, 1999). The second hypothesis assumes the formation of a multi-phase system, in which phase separation and phase deformation occur (Tolstoguzov, 1993). Wittek et al. showed for soy protein isolate that a water-rich, low-protein phase and a protein-rich, low-water phase are formed, which are aligned in the cooling die (Wittek et al., 2021a,d). It must be taken into account, however, that the different processes may take place simultaneously and influence each other. Protein denaturation and rearrangement may induce phase separation and thus support the formation of a multi-phase system. A clear overview of the different hypotheses as well as new considerations can be found in the recent review by van der Sman and van der Goot van der Sman and van der Goot (2023).

In protein-rich food gels, such as meat substitutes, yogurt, and cheese, the protein gel formed by gelation plays a decisive role in the product's texture. The gels that form can either be physical, i.e., formed by non-covalent bonds (e.g., hydrophobic, ionic), or chemical, i.e., additionally reinforced by covalent bonds (e.g., disulfide bonds) (Rubinstein and Colby, 2014). Regardless of the type of gel, the bonds between the molecules are referred to as cross-links. The gelation behavior and, hence, cross-linking density depend on both intrinsic factors that are related to the protein (i.e., amino acid composition, molecular weight) and extrinsic factors that are related to the conditions surrounding the proteins (i.e., pH, ionic strength, temperature) (Totosaus et al., 2002). While the influence of many intrinsic and extrinsic factors is extensively studied for meat substitutes, the influence of pH modification has not yet been investigated in sufficient detail.

Recently, two papers were published on pH modification in the high-moisture extrusion of pea protein isolate and concentrate, wheat gluten, and rice protein isolate (Nisov et al., 2022) and low-moisture extrusion of pea protein isolate (Muhialdin and Ubbink, 2023). These outstanding publications reveal differences in the micro- and macrostructures of the produced extrudates. The gelation process and differences in the present gel structure are not discussed in detail.

However, the influence of pH modification is studied well in many low-concentration protein solutions and protein-stabilized emulsions, such as yogurt and cheese. In this context, the process of acid-induced gel formation is referred to as acidification. The principle of gel formation is based on the effect whereby, when lowering the pH in the direction of the protein isoelectric point, the surface charge of the proteins decreases, repulsion no longer occurs, and aggregation up to gel formation takes place (Totosaus et al., 2002; Dickinson, 2012).

In addition to the altered gel formation mechanisms, a change in the pH value is also expected to alter the solubility of the proteins (Kinsella and Melachouris, 1976). For soy protein, for example, it is known that solubility is lowest at pH values of 4–5 and highest at a pH value of 2 (Foo, 2004). For a change in the pH value of gluten, it is known that the solubility is low at a neutral pH value but is fair at a pH of 4 or lower (Takeda et al., 2001). Although meat substitutes are highly concentrated systems that are not a solution as such, it can be assumed that protein solubility has an influence on the structuring of meat substitutes. In particular, it could have an influence on the formation of the multiphase system. However, this has not yet been investigated in detail and is also beyond the scope of this study.

In this work, the influence of pH modification on the gel forming and structuring of meat substitutes was investigated using two common proteins forming gels with different networks, soy protein isolate (SPI) and vital wheat gluten (referred to as gluten). SPI predominantly forms non-covalent bonds and therefore is considered a physical gel (Wittek et al., 2021d; Renkema, 2004; Chen et al., 2011). The isoelectric point (IEP) of SPI ranges between pH 4 and 5 (Gennadios et al., 1993; Malhotra and Coupland, 2004; O Flynn et al., 2021). Gluten proteins are additionally cross-linked by covalent disulfide bonds and represent a chemical gel (Fischer, 2004; Emin et al., 2017; Pietsch et al., 2017; Lagrain et al., 2010). The IEP of gluten ranges between pH 7 and 8 (Wu and Dimler, 1963).

The research question of this study is how the change in pH influences the gelation and thus the formation of meat-like structures in high-moisture extrusion process of meat substitutes. On the basis of the two protein systems, the following hypotheses are made:

The formation of a physical SPI gel is strengthened by a change in pH towards the IEP due to a decrease in electrostatic repulsive forces, resulting in an increased cross-linking density. To deform a stronger gel necessary to create meat-like structures, higher strain and shear stresses are required (Wittek et al., 2021a). Accordingly, the structure is expected to be less pronounced under constant extrusion conditions.

For a chemical gluten gel, a change in pH away from the IEP results in an increase in electrostatic repulsive forces between proteins. This may lead to fewer physical cross-links, and polymerization into a chemical gel is inhibited. A weak, unstable protein gel may result. However, the weaker gel can be better deformed in the die, although it may be doubted whether there are sufficient cross-links for a stable structure in the absence of covalent bonds.

In order to address the research question and hypotheses, first, temperature ramps were performed in a closed cavity rheometer to determine changes in gelation behavior and gel strength.

Furthermore, extrusion tests were carried out on a laboratory scale. The resulting extrudates were observed optically and investigated by classical mechanical methods to obtain further information about the resulting gels. Finally, solubility tests in reducing buffer were carried out to justify the differences in the resulting gels.

2.2 Materials and methods

2.2.1 Materials

Commercial soy protein isolate (SPI) Supro ST from Solae LLC (St. Louis, Mo, USA) and vital wheat gluten from Kröner Stärke (Ibbenbüren, Germany) were used for this study. According to the manufacturers, the protein content of SPI was >90 %, and the water content was < 6 %. The protein content of gluten was > 83 %, and the water content was < 8 %. The chemicals for studying protein solubility, sodium chloride, acetic acid, and citric acid, were obtained from Carl Roth GmbH + Co. KG (Karlsruhe, Germany) with a purity > 99.5 %.

2.2.2 Dough preparation for material screening with the closed cavity rheometer

Dough for rheological screening were prepared in a Thermomix from Vorwerk (Wuppertal, Germany). The water content of the protein doughs was adjusted according to the mass flows of the extrusion experiments. Mixtures with moisture contents of 55*wt%* for SPI and moisture contents of 45*wt%* for gluten were prepared, neglecting the water content of the protein powders. The following liquids were used: tap water; 0.1 M, 0.25 M, and 0.5 M acetic acids; 0.25 M and 0.5 M citric acids; and a sodium chloride solution with a conductivity of 6.96 mS cm^{-1}. The doughs were stored for at least 24 h in the refrigerator at 4 °C to ensure equilibrium of hydration.

2.2.3 pH Measurement of the doughs

The pH of the gluten doughs was measured with a foodcare pH electrode for meat from Hanna Instruments Deutschland GmbH (Vöhringen, Germany). As the SPI doughs were too hard and brittle, the electrode was not suitable for detecting the pH value. Here, a standard method for cereals, flour, and bread was used (Meißner, 2016). First, 5 mL of acetone and 95 mL of freshly boiled and cooled distilled water were mixed. Part of this mixture was placed in a grating bowl with 10 g of SPI dough sample and mixed to form a slurry. The slurry was then transferred without loss with the rest of the acetone/water mixture into a 250 mL Erlenmeyer flask and homogenized. The pH of the mixture was measured with a standard pH electrode while stirring gently with a magnetic stirrer. For verification, the method was also applied to selected gluten doughs and showed a good agreement with the measurements of the foodcare pH electrode for meat.

2.2.4 Material and parameter screening with the closed cavity rheometer

Material screening was performed with a rubber process analyzer (RPA) flex, also called a closed cavity rheometer (CCR), from TA Instruments, Inc. (New Castle, DE, USA). This rheometer possesses a closed bi-conical, grooved geometry (radius = 20.625 mm, angle = 7.16°) and is widely used to investigate rheological properties of protein–water mixtures (Emin et al., 2017; Wittek et al., 2020; Schreuders et al., 2021a). The sealed measuring geometry is closed during the measurement with a closing pressure of 4.5 bar, which prevents the evaporation of water at temperatures above 100 °C. The grooves in the geometry prevent the material from slipping.

For material screening, a temperature ramp was performed between 40 °C and 150 °C for SPI samples and between 40 °C and 170 °C for gluten samples. The heating rate was set constant at $5\,\mathrm{K\,min^{-1}}$. Strain sweeps were used to determine the combination of frequency and strain. For SPI samples, a frequency of 1 Hz and a strain of 1 % were chosen to ensure a good signal-to-noise ratio within the linear visco-elastic (LVE) region. For gluten samples, a frequency of 5 Hz and a strain of 5 % were required to obtain a good signal-to-noise ratio, which was still within the LVE region. Temperature sweeps were carried out in triplicate, and the mean value and the deviation were determined.

2.2.5 Extrusion process

Extrusion experiments were performed using a lab-scale twin-screw extruder Process 11 (Thermo Fisher Scientific, Karlsruhe, Germany) mounted with a cooled slit die. The protein powder (SPI or gluten) was dosed via a gravimetrically controlled feeder of Brabender Technology GmbH (Duisburg, Germany). The liquid feed (water, acid, or salt solution) was pumped by a peristaltic pump Masterflex L/S from Cole Parmer (Vernon Hills, IL, USA) into the third barrel element. A schematic drawing of the process is given in figure 2.1. The screw had a length to diameter ratio (L/D) of 40. It was mainly made of conveying elements, with a 1.5 L/D 90° kneading block installed after liquid dosing. The screw speed was kept constant at 600 rpm for all extrusion experiments. The dimensions of the cooling die were H × W × L: 4 × 19 × 125 mm, and temperature of the cooling die was set to 30 °C. Mass flow rates of the proteins, mass flow rates of the liquid feeds, and the barrel temperature profile can be found in Table 2.1. Tap water; 0.1 M, 0.25 M, and 0.5 M acetic acid; and 0.25 M and 0.5 M citric acid were used as liquid feeds. The extrudates obtained were cut into pieces and frozen for storage until further analysis. As shown in the study by Nieuwland et al., it is assumed that the freezing of the extrudates does not affect the meat-like structure and therefore has no influence on the subsequent analysis (Nieuwland et al., 2023).

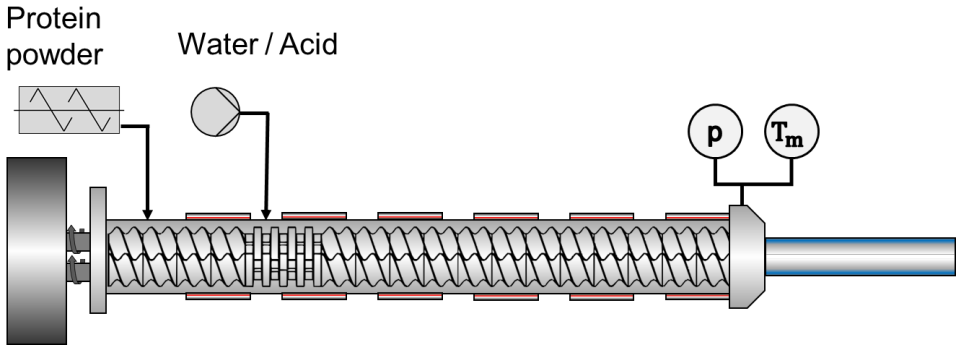

Figure 2.1: Schematic extruder setup.

Table 2.1: Mass flow rates of the protein powder ($\dot{m}_P$) and liquid feed ($\dot{m}_L$) as well as temperature profile of the seven extruder barrel sections (T_{2-8}) and the die adapter ($T_{Material}$)

Material	$\dot{m}_P$	$\dot{m}_L$	T_2	T_3	T_4	T_5	T_6	T_7	T_8	$T_{Material}$
	kg/h	kg/h	°C	°C	°C	°C	°C	°C	°C	°C
soy protein isolate	0.23	0.28	25	50	90	95	100	140	140	140
vital wheat gluten	0.55	0.45	25	50	90	95	100	160	160	160

2.2.6 Visual inspection

To visualize changes in the anisotropic structure, the extruded samples were thawed overnight and heated to room temperature. Figure 2.2 shows how the samples were prepared before pictures were taken.

2.2.7 Compression test

Compressive stresses of the extruded samples were measured with a stress-controlled HAAKE MARS 60 rheometer (Thermo Fisher Scientific, Karlsruhe, Germany). Samples with a round cross-sectional area of 6 mm in diameter were cut out of the center of the extrudates. The upper plate of the rheometer was closed with a velocity of 0.25 mm s^{-1}, and a stress–strain diagram was recorded. The measurements were performed up to a maximum force of 45 N. Young's modulus was calculated from the linear region of the stress–strain diagram using Equation 2.1 as described by Willats et al. (Willats et al., 2001) and Fraeye et al. (Fraeye et al., 2010), where

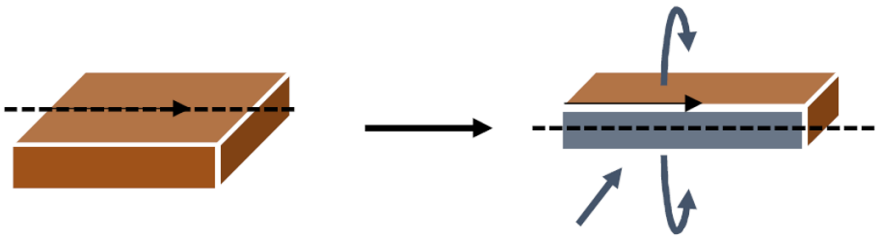

Figure 2.2: Representation of sample preparation: Thin black arrow—flow direction, dashed line—cutting line, gray plane—photographed plane.

E is Young's modulus, F the measured force, A the sample's cross-sectional area, σ the stress, and ε the strain.

$$E = \frac{F}{A \cdot \varepsilon} = \frac{\sigma}{\varepsilon} \tag{2.1}$$

Young's modulus was calculated for a strain of 4-12 % for SPI and 10-20 % for gluten (linear fit $R^2 > 0.99$). Compression tests were carried out in triplicate, and the mean value and the deviation were determined.

2.2.8 Rheological measurement of the extrudates

Strain-sweep experiments of the extrudates were performed using a stress-controlled HAAKE MARS 60 rheometer from Thermo Fisher Scientific (Karlsruhe, Germany). A serrated plate geometry was used with a diameter of 20 mm. Samples with a round cross-sectional area of 20 mm in diameter were cut out of the center of the extrudates. The gap width was set to 3.4 mm for the SPI extrudates and 3.0 mm for the gluten extrudates. The measurements were performed at a temperature of 20 °C, at a frequency of 1 Hz, and a stress between 1 and 10^5 Pa. Before each measurement, all samples were allowed to sit 120 s to rest and equilibrate. Strain-sweep experiments were carried out in triplicate, and the mean value and the deviation were determined.

2.2.9 Protein solubility

To investigate the formation of covalent bonds during the extrusion process, the solubility in a non-reducing buffer was studied. The buffer was prepared with 0.132 M sodium dihydrogen phosphate, 0.68 M disodium hydrogen phosphate, 0.05 M sodium chloride, 0.0173 M M sodium dodecyl sulfate (SDS), and 8 M urea. The extrudates as well as raw protein powders were predried at 50 °C for 24 h, ground, and sieved to a particle size < 280 µm. A total of 10 mg of the sample was mixed with 20 mL buffer, vortexed for 30 s, and dissolved at room temperature for 24 h in a rotary shaker from Edmund Bühler GmbH (Bodelshausen, Germany) at 200 rpm. To obtain the supernatant for determining the protein concentration, a 5920 R centrifuge from Eppendorf AG (Hamburg, Germany) was used at 4310 × g for 50 min. The absorbance at 280 nm of the supernatant was analyzed in an Evolution 201 spectrophotometer by Thermo Fisher Scientific Inc. (Waltham, MA, USA). A bovine serum albumin (BSA) calibration curve was obtained to calculate relative protein concentrations (concentration range 0.005–2 mg BSA/mL buffer, $R^2 > 0.99$). Solubility and absorbance measurements were repeated three times each, resulting in a total of nine absorbance values per sample.

2.2.10 Statistical analysis

Data of the analyses of the complex viscosity at 100 °C for SPI and analyses of the storage modulus of the extrudates was assessed via multifactorial analysis of variance (ANOVA) and a Turkey test as a post hoc test. Dissimilarities in the samples were considered statistically relevant at a level of $p \leq 0.05$. The software OriginPro 2019 v9.6 (OriginLab Corp., Northampton, MA, USA) was used for the statistical analysis, calculation of averages, and standard deviations.

2.3 Results and discussion

2.3.1 Material screening based on measurements in the closed cavity rheometer

Temperature ramps were performed to obtain information about the gel structure and to predict changes in the reaction and gelation behavior. Figure 2.3 shows the complex viscosity plotted over the temperature for SPI (A) and gluten (B) doughs prepared with water and acids. For protein doughs, a decrease in complex viscosity can be related either to an increase in molecular mobility or, at elevated temperatures, to degradation reactions. An increase in complex viscosity can be attributed to aggregation or polymerization reactions (Emin et al., 2017; Wittek et al., 2021c; Opaluwa et al., 2024).

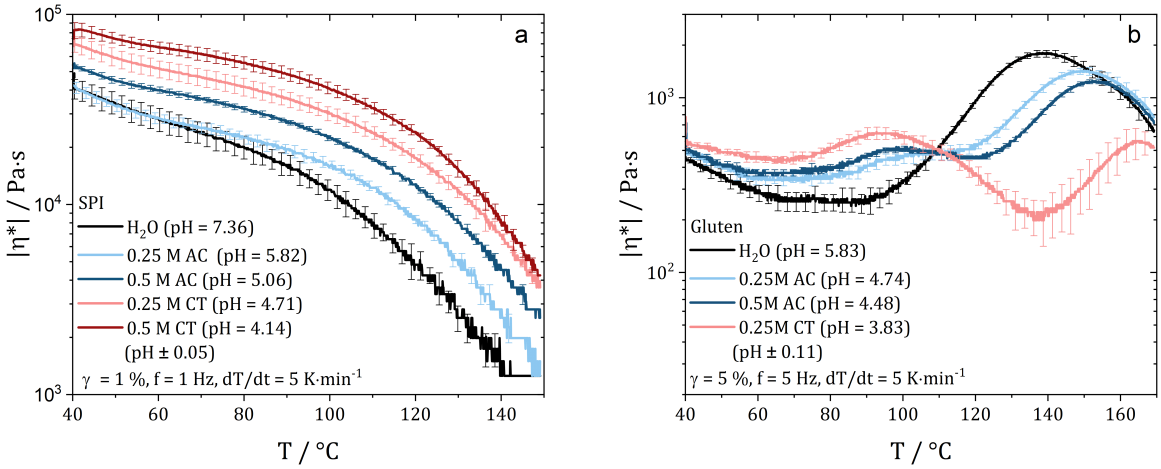

Figure 2.3: Temperature ramp of SPI (a) and gluten (b) doughs prepared with water and acids in different concentrations.

For all SPI samples (figure 2.3a), complex viscosity is observed to decrease with the increase in temperature for the whole temperature range. As described before, the decrease in complex viscosity is due to the higher mobility of the molecules. The absence of an increase in complex viscosity indicates that no polymerization takes place, as already described in the literature (Wittek et al., 2020).

The addition of the acid causes a horizontal shift of the complex viscosity curves. The complex viscosity increases at the starting temperature (40 °C), indicating that the proteins are pre-coagulated. The value of the complex viscosity at a temperature of 100 °C (taken from figure 2.3a) increases with the decrease in pH value, ranging from 11970 ± 1490 Pa s for pH 7.36 to 15,970 ± 1000 Pa s for pH 5.82, to 22350 ± 719 Pa s for pH 5.06, to 30090 ± 2520 Pa s for pH 4.71, to 40480 ± 2610 Pa s for pH 4.14. As assumed in the hypothesis, the increasing complex viscosity with the decrease in pH shows that the cross-linking density increases. This can be attributed to the pH moving towards the IEP of SPI, which reduces repulsion of the molecules.

The addition of acid to gluten leads to a shift away from the IEP. Even if repulsion between the molecules increases, a cross-linking of the proteins can be detected for all investigated samples. The complex viscosity of the dough with 0.5 M citric acid was too low to be measured with an acceptable signal-to-noise ratio and, hence, is not shown.

For the gluten/water mixture with a pH of 5.83, the typical behavior of gluten is obtained. There is an initial decrease in complex viscosity up to a temperature of about 60 °C due to the increasing mobility of the molecules with the increase in temperature. As the temperature is further increases, the slope changes (reaction onset), and a large increase in complex viscosity is observed from a temperature of about 90 °C. This increase can be linked to the polymerization reaction of the glutenin and gliadin fractions of gluten (Emin et al., 2017). The maximum is reached at 138 °C, after which the complex viscosity decreases again due to the increasing mobility and/or degradation reactions.

Contrary to SPI, no horizontal shift in complex viscosity is observed for gluten due to the modification of the pH by adding acids. At low temperatures (< 70 °C), complex viscosity is slightly increased with the decrease in pH. Interestingly, polymerization appears to start at lower temperatures with the decrease in pH. The increase in complex viscosity starts at a temperature around 90 °C for pH 5.83, 83 °C for pH 4.74, 80 °C for pH 4.48, and 80 °C for pH 3.83. For the pH-modified samples, there is a plateau in complex viscosity at a temperature of 102 °C for pH 4.7 and 98 °C for pH 4.48 and even a decrease in complex viscosity at a temperature of 92 °C for pH 3.83. However, a second increase in complex viscosity can be observed at temperatures of 115 °C for pH 4.7, 123 °C for pH 4.48, and 138 °C for pH 3.83. After reaching complex viscosity maxima at temperatures of 149 °C for pH 4.8, 152 °C for pH 4.48, and 165 °C for pH 3.83, it seems like the complex viscosity curves coincide again. The reason for the different complex viscosity curves, especially those with two regions of complex viscosity increase, is not clear.

However, when the pH is modified by the addition of acids, the ionic strength of the solution is also changed. It is known that the structure of protein networks can also be changed by changing the ionic strength (Totosaus et al., 2002). Accordingly, NaCl solutions were prepared with the ionic strength of the strongest acid (0.5 M citric acid), and temperature ramps were performed with the CCR. No significant change was observed (see Appendix figure 7.1), which is why the changes are attributed to the shift in pH exclusively.

Based on the changed gel strength for SPI and the changed polymerization behavior of gluten, we assume that the addition of acid affects the structuring process in high-moisture extrusion. The complex viscosity of the SPI doughs increases with the decrease in pH, which will have an influence on the flow profile in the cooling die. From these data, we expect that the meat-like structures are not as pronounced because higher shear rates and higher strain rates are required to deform the gel, and the effects of plug flow and wall slip may be enhanced. For gluten, no clear expectation can be stated. On the one hand, it should be easier to deform the weaker gels due to the decreased complex viscosity at moderate temperatures (110–140 °C). On the other

hand, lack of covalent cross-linking due to a change in polymerization rate can result in a gel that is too deformable and weak.

2.3.2 Changes in the macroscopic structure of meat substitutes due to the addition of acids

For the SPI (figure 2.4) and gluten extrudates (figure 2.5) prepared with water, anisotropic fibrous structures can be produced, as already shown in the literature (Wittek et al., 2021a; Kendler et al., 2021). Parabolic flow profiles are obtained for both protein types, with SPI exhibiting larger, longer fibers than gluten. As expected from the CCR experiments, both proteins exhibit a change in structure after extrusion with acids.

The fibrous structure of the SPI samples is less pronounced at pH 5.82. As the pH decreases further, no fibrous structure can be seen at all. The samples become very brittle and solid. The rheological data obtained with the CCR indicate that the complex viscosity increases with the decrease in pH. As no fibrous structure is visible after extrusion and no parabolic flow profile can be seen, it is hypothesized that the flow profile changes. It is possible that the shear stress is no longer sufficient to make the material flow, and a kind of plug flow prevails in the die. Additionally, the multi-phase system and phase separation may be changed due to the addition of the acid as a stronger gel is formed and the formation of a second phase could be suppressed. The change in the solubility of the proteins could also have an influence on the formation of the multiphase system, as it has been shown in the literature that a water-poor, protein-rich phase and a water-rich, protein-poor phase occur (Wittek et al., 2021d). Cryo-imaging or Micro-CT imaging may provide some more information in the future (Wittek et al., 2021d). It would also be interesting to see whether it is possible to create fibrous structures by changing the complex viscosity of the pH-modified samples, e.g., by increasing the temperature or decreasing the protein concentration.

For the gluten samples, fibrous structures are visible in the samples up to a pH value of 4.48, although they are less pronounced. For the samples with pH 3.83 and 3.37, a fibrous structure is no longer visible. With a decreasing pH and, hence, an increasing distance from the IEP, the extrudates become more elastic and dough-like. This can be attributed to the increased repulsion between the protein molecules as well as to the changed polymerization kinetics displayed by the rheological data obtained with the CCR, which could lead to fewer cross-links. For gluten dispersions prepared in a pH range from 7 to 2.5 and heated at 133 °C for 15 min, Langstraat et al. also reported that the cross-linking reaction was impaired significantly when the pH was lowered (Langstraat et al., 2015).

A comparison with high-moisture-extruded meat substitutes with altered pH value from the work of Nisov et al. is only possible to a limited extent, as the anisotropic structure was not visualized. However, the results describing that structuring at lower pH of rice protein, vital wheat gluten, and pea protein concentrate and isolate extrudates requires a higher temperature

Soy Protein Isolate	
H2O (pH = 7.36)	
0.25 M AC (pH = 5.82)	
0.5 M AC (pH = 5.06)	
0.25 M CT (pH = 4.71)	
0.5 M CT (pH = 4.14)	

Figure 2.4: Soy protein isolate extrudates produced with water, 0.25 M acetic acid, 0.5 M acetic acid, 0.25 M citric acid, and 0.5 M citric acid.

Gluten	
H2O (pH = 5.83)	
0.25 M AC (pH = 4.74)	
0.5 M AC (pH = 4.48)	
0.25 M CT (pH = 3.83)	
0.5 M CT (pH = 3.37)	

Figure 2.5: Gluten extrudates produced with water, 0.25 M acetic acid, 0.5 M acetic acid, 0.25 M citric acid, and 0.5 M citric acid.

suggest that the network has been altered by the pH change, and structuring is more difficult to achieve (Nisov et al., 2022).

2.3.3 Influence of the modification of pH on the mechanical properties of meat substitute extrudates

Mechanical analyses provide information about the gel structure, as the cross-linking density correlates with mechanical properties. For this reason, mechanical properties of the extrudate are used to confirm the explanations of the visual observations and CCR measurements.

Figure 2.6 shows the stress–strain curves for the SPI (a) and gluten extrudates (b). The stress–strain curves for SPI (figure 2.6a) confirm the optical description of the extrudate. As the pH decreases and the IEP is approached, the extrudates become stiffer and reach the maximum force at a lower strain. With the decrease in pH, the slope of the curves increases, and a higher force is needed for the same strain. While the extrudates produced with water can still be compressed by up to 62% at maximum force, the extrudate at pH 4.14 can only be compressed by 48% at the same force. Similar observations were reported in the literature for soy protein networks with lower concentrations. Shen et al. reported for a soy yoghurt that the hardness of the yoghurt increases with the decrease in pH (Shen et al., 2021). For heat-induced SPI gels, Renkema found that stronger networks were formed closer to the IEP due to the increased attractive interaction energy (Renkema, 2004). The results obtained here and the results presented in the literature indicate that the cross-link density increases with the decrease in pH, as was assumed. Accordingly, the gel becomes stronger, which correlates to the rheological data obtained with the CCR.

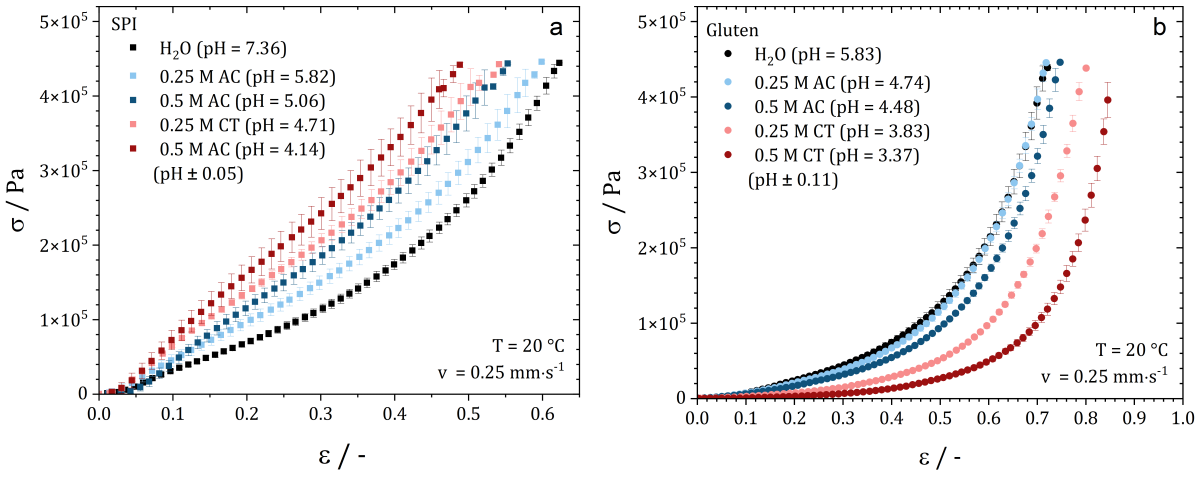

Figure 2.6: Compression tests of (a) soy protein isolate extrudates and (b) gluten extrudates produced with water, 0.25 M acetic acid, 0.5 M acetic acid, 0.25 M citric acid, and 0.5 M citric acid.

Visual inspection of the gluten doughs revealed that the extrudates became more deformable and dough-like with the decrease in pH. These observations are confirmed by the stress–strain curves. With the decrease in pH, the plastic behavior of the gluten extrudates increases, i.e., less force is required for the same deformation, and the sample can be deformed further before the yield point occurs. While the extrudate prepared with water was compressed by 70% at maximum force, a strain of 85% was achieved for the sample with a pH of 3.37. This could be due to the fact that repulsion increases with the decrease in pH and polymerization is inhibited, which results in a lower cross-linking density. This has already been reported in the literature for gluten dispersions (Langstraat et al., 2015).

In addition to the compression tests, strain sweeps were conducted on the different extrudate samples. The mean value of the storage modulus in the LVE (101–104 Pa) as well as Young's modulus were used to estimate the cross-link density (Shen et al., 2021; Saavedra I. et al., 2023). Figure 2.7 shows the storage modulus and Young's modulus plotted over the pH value. The corresponding strain sweeps are presented in Appendix figure 7.2). For the SPI extrudates (figure 2.7a), the storage modulus and Young's modulus increase with the decrease in pH value. While the absolute values of the storage modulus and Young's modulus differ, their trends are almost parallel. This indicates that the protein molecules become closer together with the decrease in pH value and more cross-links, and thus a stronger gel is formed, as expected. Solubility tests in reducing buffer (Appendix figure 7.3) suggest that no additional chemical cross-links are formed, as reported in the literature (Wittek et al., 2021d). The additional cross-links formed are due to steric, hydrophobic, ionic, van der Waals interactions or hydrogen bonds. Accordingly, we can confirm our hypothesis that a decrease in the pH in the high-moisture extrusion process leads to SPI forming a stronger gel based on physical interactions, which results in less pronounced meat-like structures.

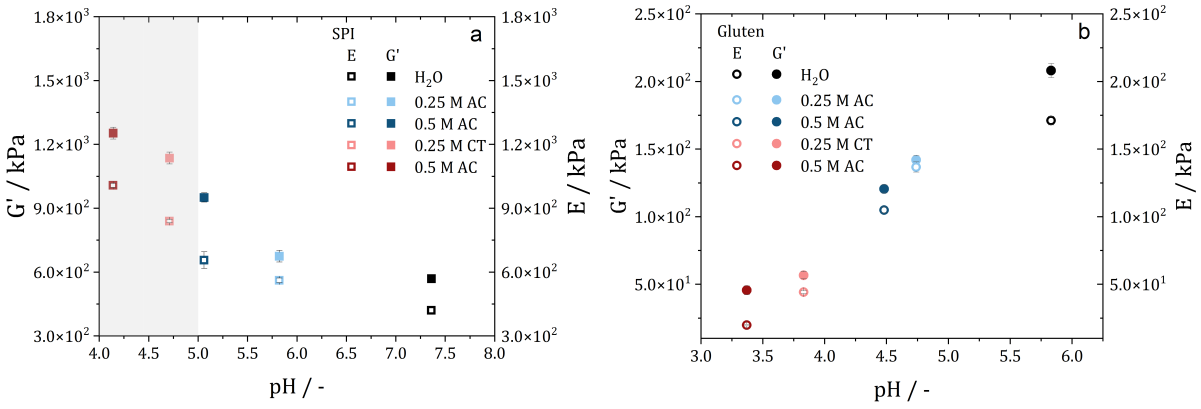

Figure 2.7: Compression tests of (a) soy protein isolate extrudates and (b) gluten extrudates produced with water, 0.25 M acetic acid, 0.5 M acetic acid, 0.25 M citric acid, and 0.5 M citric acid.

As already reported, the opposite behavior is found for gluten extrudates. With the decrease in pH, the storage modulus and Young's modulus decrease with the same tendency. Solubility tests

in reducing buffer (Appendix figure 7.3) indicate that with the decrease in pH, fewer disulfide bonds are formed, and the polymerization reaction is inhibited. The decreasing cross-linking density can be explained by two phenomena. On the one hand, repulsion between the protein molecules increases, as the pH moves away from the IEP. On the other hand, the polymerization reaction is inhibited, resulting in fewer covalent bonds. Thus, by lowering the pH during gluten extrusion, we obtain a weaker gel that is easier to deform. However, no anisotropic structures can be generated because there are probably too few cross-links.

2.4 Conclusion

The effects of pH modification on the textural properties of meat analogues were assessed successfully. Soy protein isolate (SPI) and vital wheat gluten were studied as representatives of a physical and chemical gel, respectively.

For gels made from SPI, tests at the closed cavity rheometer and mechanical tests of the meat substitutes produced have shown that the cross-linking density increases with the decrease in pH. Solubility tests showed that the new cross-links must be of a physical nature. The resulting firmer gels made structuring more difficult at a reduced pH value. For the gels produced from gluten, an altered polymerization reaction resulting from a change in pH was observed by screening in the closed cavity rheometer. Mechanical tests of the produced meat substitutes showed that the cross-linking density decreases with the decrease in pH, and solubility tests showed that fewer covalent bonds were formed. Structuring the pH-reduced gels is more difficult, as the gel is not strong enough to hold a structure due to the lack of disulfide bonds. This study shows that the addition of acid for taste or stability can have dramatic consequences in the production of meat substitutes. Accordingly, the process must be redesigned when the recipe is changed.

3 Local Residence Time and Thermomechanical Stress Profile in Twin-Screw Extrusion

Chapter 3 is published as: F. Ellwanger, L. Pernice, H.P. Karbstein, and M. A. Emin. Investigating local residence time and thermomechanical stress profile in twin-screw extrusion of plant proteins by using the moving particle semi-implicit simulation method. *Journal of Food Engineering 359: 11665* (2023). doi: 10.1016/j.jfoodeng.2023.111665. Text, tables, figures and equations have been edited and reformatted for consistency.

Abstract

Temperature, mechanical stress, and the residence time are important process variables that must be monitored during the production of food by twin-screw extrusion. In production, these variables are mainly considered as integral variables over the entire process. However, local deviations, for example in temperature, can lead to uncontrolled product changes. In this work, the moving particle semi-implicit simulation method was used to simulate local sections of a partially filled twin-screw extruder. The influence of screw configurations with kneading blocks with different offset angles on the degree of filling, the residence time, and mechanical stress was investigated. Further, the temperature profile was determined for a screw configuration with neutral kneading blocks. To evaluate the physical reliability of the simulation results, deadstop experiments were performed, and a good agreement was found between the filling degrees obtained from the simulation and the experiments.

3.1 Introduction

Twin-screw extruders provide a continuous, cost-efficient manufacturing process. Due to its versatility, twin-screw extrusion finds application in the polymer, pharmaceutical, and food industries. To the food industry, the process is advantageous as many process steps like mixing, cooking, and forming can be realized in one unit. The thermal and mechanical (thermomechanical) stress profiles resulting from the rotation of the screws and the temperature control of the barrel can cause desired and undesired changes in the raw materials used. For example, valuable ingredients such as anthocyanins may be lost due to the thermomechanical treatment (Schmid et al., 2022). On the other hand, proteins, for example, may denature and react, resulting in new desired functional properties (Pietsch et al., 2019c). A detailed review of potential changes during extrusion is given, for example, in the work of Camire et al. (Camire et al., 1990).

For the extrusion of proteins and other foodstuffs, it is important to know the conditions prevailing in the extrusion process. Usually, information about these process conditions is obtained in the form of integral process variables. For the mechanical stress profile, the torque of the motor that drives the screws is determined and expressed as specific mechanical energy (SME) (van Lengerich, 1990). For the thermal stress profile, mainly the material temperature shortly upstream of the extruder die is measured. The residence time in the extruder can be determined, for example, by tracer detection measurements at the outlet of the extruder. However, this information about the integral process conditions are not sufficient to control and predict reactions that occur inside the barrel of the extruder during the food extrusion process, e.g. protein denaturation. Rather, it would be necessary to know local process conditions such as temperature profiles and peaks, maximum shear stresses, and local residence times (Pietsch et al., 2019c). Determining these local conditions experimentally is very time-consuming or not even feasible due to the limited accessibility of sensors in the screw section. Obtaining the true melt temperature in the screw section requires a fast response time of the measuring device. This may be achieved by use of infrared sensors (Emin et al., 2016). In order to determine shear stresses, encapsulated dye tracers can be used, which break open under a defined stress and release the dye (Fukuda et al., 2015). Information on the local residence time can be obtained by measuring the residence time distribution at different positions along the barrel (Zhang et al., 2006). To reduce experimental effort and save material and costs, computational fluid dynamics (CFD) can be used to obtain more detailed information about the thermomechanical stress profile. In the past, mesh-based methods such as the Finite Element Method (FEM) were used to calculate the flow through the screw sections of extruders (Emin et al., 2021). This approach is suitable to simulate small sections of a fully filled extruder and to obtain information about the thermomechanical stress profile. Lagrangian particle-based simulation methods such as smoothed particle hydrodynamics (SPH) have recently gained in importance due to increasing computational power and efficiency. Since flows are computed from particles rather than meshes, these methods are suitable for simulating flow problems with complex moving geometries and free surfaces. Thus, these methods are very interesting for considering twin-screw extrusion processes. Accordingly, work has been done dealing with general flow conditions and limitations (Wittek et al., 2018),

mixing characteristics (Bauer and Khinast, 2022), and local residence time distributions (Bauer et al., 2022). Recently, Meza and Nirschl investigated the pressure characteristics and shear rate distribution of different screw elements under variation of the filling degree and flow rate for a Newtonian fluid at isothermal flow (Meza Gonzalez and Nirschl, 2023). However, the thermomechanical stress profile experienced by the extruded material has not yet been investigated in detail with these methods.

The aim of this publication is to demonstrate the potential applicability of the moving particle semi-implicit (MPS) method to the twin-screw extrusion of typical food raw materials. The MPS method was introduced in 1996 by Koshizuka and Oka (Koshizuka and Oka, 1996) and was built to investigate the fragmentation of incompressible fluids. The method is a mesh-less particle-based Lagrangian simulation method like the SPH method. Here, the MPS code was used, which is embedded in the commercial software Particleworks. This software is already being used in a wide variety of research areas, for example the oil distribution in gears (Deng et al., 2020), oil cooling of electrical motors (Moll et al., 2021), or the towing conditions of a cone-shaped drogue (Zhu et al., 2021). To the best of our knowledge, the MPS method and the Particleworks software were only used once in the context of twin-screw extrusion. Fukuzawa et al. coupled a discrete element method (DEM) with the MPS method to simulate the plasticization process of polymers in a twin-screw extruder (Fukuzawa et al., 2017).

In this publication, the reaction zone of the screw section of a laboratory-scale twin-screw extruder is considered by means of the MPS method. The focus is set on the mean residence time, the degree of filling, the local residence time distribution in the kneading blocks, the mean mechanical stress, and the local temperature profile. Additionally, the influence of the particle size on the simulation results is investigated at the beginning, which is similar to a mesh study in classical simulation approaches. The simulated material is a soy protein isolate - water mixture whose shear viscosity is described with a Bird-Carreau approach coupled with an Arrhenius approach as proposed by Wittek et al. (Wittek et al., 2021a). The results contribute to a better understanding of the extrusion process of food systems and can save resources in product design in the future.

3.2 Materials and methods

3.2.1 MPS methodology

The MPS method is a Lagrangian method where the physical quantities are calculated and distributed on moving particles. Accordingly, the simulated incompressible fluid is represented by the particles, each of which carries information about pressure, temperature, velocity, etc. The fundamental equations behind the MPS method are the continuity equation (3.1), the Navier-Stokes equation (3.2), and the energy conservation law (3.3),

$$\frac{D\rho}{Dt} = 0 \tag{3.1}$$

$$\frac{D\mathbf{v}}{Dt} = -\frac{\nabla p}{\rho} + \nu\nabla^2\mathbf{v} + \mathbf{g} \tag{3.2}$$

$$\frac{De}{Dt} = -\nabla * (-\lambda\nabla T) \tag{3.3}$$

where $\frac{D}{Dt}$ expresses a Lagrangian derivation, ρ is the density, $\mathbf{v}$ is the velocity, p is the pressure, ν is the kinematic shear viscosity coefficient, $\mathbf{g}$ is the gravity acceleration, e is the internal energy, λ is the thermal conductivity, and T is the absolute temperature. The Navier-Stokes equation (3.2) is solved using a temporary time step. First, all terms except for the pressure term are solved implicitly following Equation 3.4,

$$\frac{\mathbf{v}^* - \mathbf{v}^k}{\Delta t} = \nu\nabla^2\mathbf{v}^k + \mathbf{g} \tag{3.4}$$

where superscript k expresses the current time step and superscript $*$ expresses the temporary time step at which the explicit calculation has been completed. In a second step, the implicit calculation of the pressure takes place. By default, the calculation is done according to Equation 3.5,

$$\nabla^2 p^{k+1} = \frac{\rho}{\Delta t^2}\frac{n^* - n^0}{n^0} \tag{3.5}$$

where superscript $k+1$ expresses the following time step, n^* describes the particle number density, and n^0 the particle number density at the initial state. The number density is explained later.

In this work, a pressure stabilization model was used for calculation of the pressure according to Equation 3.6,

$$\nabla^2 p^{k+1} = -\lambda_R \frac{\rho}{\Delta t^2}\left[(1-\beta)\frac{n^* - 2n^k + n^{k-1}}{n^0} + (\beta-\gamma)\frac{n^* - n^k}{n^0} - \gamma\frac{n^* - n^0}{n^0} - \alpha P^{k+1}\right] \tag{3.6}$$

where β and γ are parameters of the pressure stabilization model, α is the compressibility, and λ_R is a relaxation coefficient. By default, the values of the compressibility and the relaxation coefficient are $\alpha = 10^{-9}$ and $\lambda_R = 0.2$, respectively. Finally, using the calculated pressure gradient, the temporary particle velocities and positions are corrected according to Equation 3.7

$$\frac{\vec{v}^{k+1} - \vec{v}^*}{\Delta t} = -\frac{\nabla p^{k+1}}{\rho}. \tag{3.7}$$

As the particles move, their interaction with neighbouring particles is described by a kernel function (3.8),

$$w(|\mathbf{r}_{ij}|) = \begin{cases} \dfrac{r_e}{|\mathbf{r}_{ij}|} - 1 & 0 \leq |\mathbf{r}_{ij}| < r_e \\ 0 & |\mathbf{r}_{ij}| \geq r_e \end{cases} \tag{3.8}$$

where $|\vec{r}_{ij}|$ is the distance between two particles, and r_e is the effective action radius of particles. Accordingly, if the distance between two particles is greater than the effective radius, they do not influence each other. Using the kernel function, the particle number density can be defined (Equation 3.9)

$$n_i = \sum_{j \neq i} w(|\mathbf{r}_{ij}|). \tag{3.9}$$

The particle number density is a dimensionless quantity, which is unique to the MPS method and expresses the density of particle placement.

3.2.2 Simulation setup

In this work, the MPS method implemented in the commercial Particleworks 7.1.0 software (Promtech Software Inc., Tokyo, Japan) was used. The simulated geometries were loaded into the software as stl files. These are the extruder barrel and the different screw configurations. The

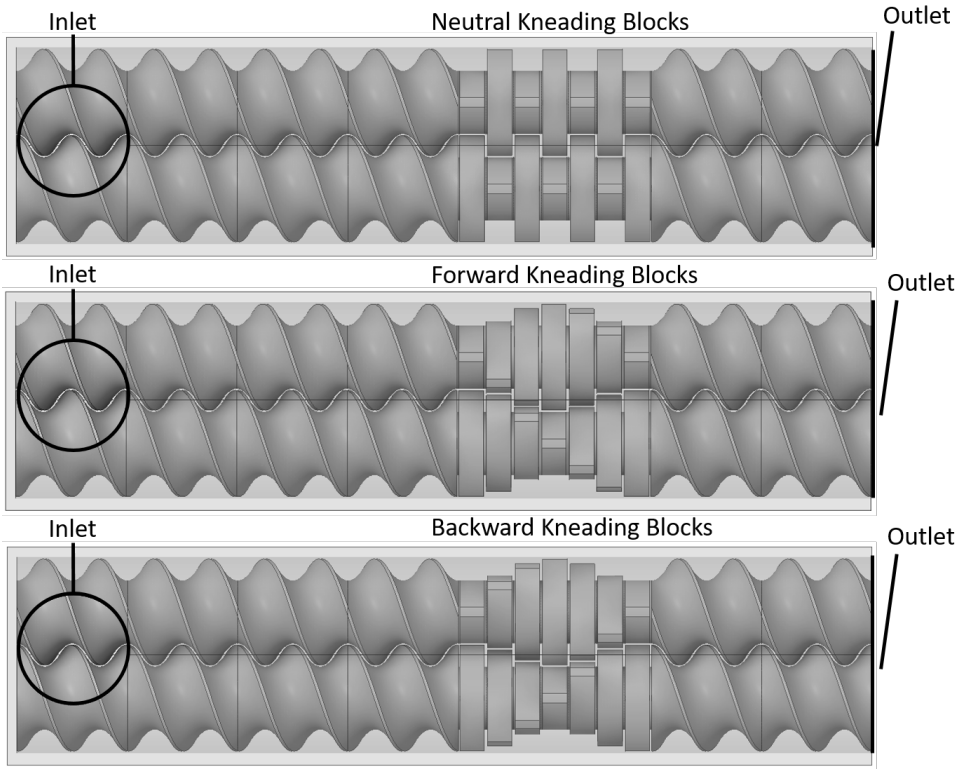

Figure 3.1: Simulated geometries with the simulated screw configurations with a L/D of 7.75 in the barrel, the inlet and the outlet.

Table 3.1: Dimensions of the barrel, conveying elements, and kneading discs.

	Variable	Dimension [mm]
Inner screw diameter	D_i	6.3
Outer screw diameter	D_o	10.6
Barrel diameter	D	11
Center distance	C	8.6
Conveying element length	L_1	11
Kneading disc length	L_2	2.75
Kneading section length	L_3	2.45

geometries are shown in figure 3.1. The different screw configurations are each composed of 4 conveying elements and 7 kneading discs followed by 2 further conveying elements. The offset angle between the kneading discs is 90° for the neutral kneading blocks and ±30° each for the forward and backward kneading blocks, respectively. A detailed illustration of the conveying elements and kneading discs inside the barrel is given in figure 3.2, and the corresponding dimensions are given in Table 3.1. The screws have a length-diameter ratio (L/D) of 7.75. The inlet has a diameter of 11 mm and a distance of 1.5 mm from the tip of the screw. The outlet is represented by a plane at the end of the screw and the barrel.

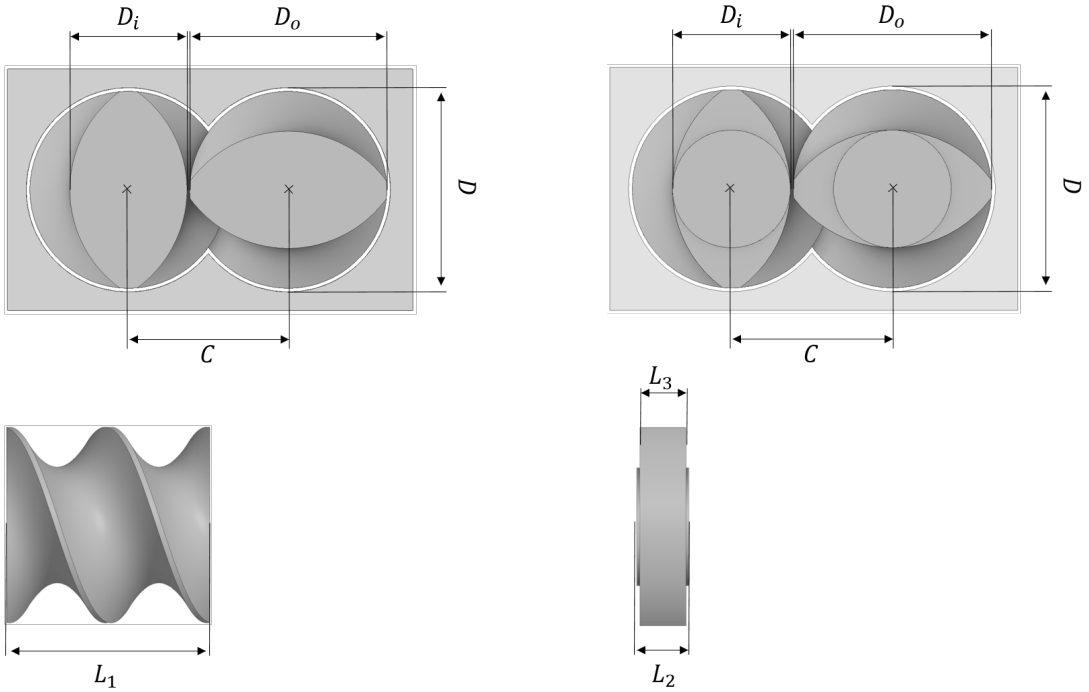

Figure 3.2: Illustration of the conveying elements and kneading discs inside the extruder barrel.

The screws rotate counterclockwise with a screw speed of 600 rotations per minute (rpm). A volumetric flow rate of $2.8 \times 10^{-7}\,\mathrm{m^3\,s^{-1}}$ is the inlet boundary condition. This corresponds to a massflow rate of $1.41\,\mathrm{kg\,h^{-1}}$ at a given density of $1400\,\mathrm{kg\,m^{-3}}$. Reaching the outlet plane, the particles are eliminated. The no-slip condition applies to the surfaces of the rotating screws and the barrel. For investigation of the influence of the particle size, the simulation results, particle diameters of $= 0.6, 0.3, 0.15$, and $0.1\,\mathrm{mm}$ were examined. The subsequent simulations were calculated with a particle diameter of $0.15\,\mathrm{mm}$. The simulations of the influence of the particle size on the conveying behaviour and the investigation of the influence of the screw configurations were carried out under isothermal conditions at a temperature of $100\,^{\circ}\mathrm{C}$. To investigate the thermomechanical stress profile, one simulation with neutral kneading blocks was performed under non-isothermal conditions. In that case, the particle inflow temperature is given with $100\,^{\circ}\mathrm{C}$, and the barrel has a constant temperature of $100\,^{\circ}\mathrm{C}$. The screws are considered as adiabatic, and the viscous energy dissipation of the material is taken into account. The thermal conductivity of the material is set to $\lambda = 0.375\,\mathrm{W\,m^{-1}\,K^{-1}}$ (Sweat V. E., 1986) and the specific heat to $2900\,\mathrm{J\,kg^{-1}\,K^{-1}}$ (Singh and Heldman, 2009).

The shear viscosity of the material is described with a user-defined function to couple the shear rate dependency with the temperature dependency. A Bird-Carreau approach was chosen for the shear rate dependence and an Arrhenius approach for the temperature dependence. The model is given in Equation 3.10. The values of the model are oriented towards a previous publication and are given in Table 3.2 (Wittek et al., 2021a).

Table 3.2: Values of the shear viscosity model describing the shear rate dependency of the shear viscosity and temperature dependency of the shear viscosity.

	Variable	Value	Unit
Shear viscosity at infinite shear rate	η_∞	27	Pa s
Shear viscosity at zero shear rate	η_0	$1.014 * 10^7$	Pa s
Characteristic time	λ_R	100	s
Shear thinning factor	n	0.099	-
Reference temperature	T_{ref}	333	K
Arrhenius factor	α	1383	K

$$\eta(\dot{\gamma},T) = (\eta_\infty + (\eta_0 - \eta_\infty) * (1 + (\lambda_R \dot{\gamma})^2)^{\frac{n-1}{2}}) * exp(\frac{\alpha}{T} - \frac{\alpha}{T_{ref}}) \tag{3.10}$$

The first part of Equation 3.10 is the Bird-Carreau approach, where $\dot{\gamma}$ is the shear rate, η_∞ is the shear viscosity at infinite shear rate, η_0 is the shear viscosity at zero shear rate, λ_R is the characteristic time, and n is the shear thinning factor. The second part of Equation 3.10 is the Arrhenius approach, where α is the Arrhenius factor, T is the temperature, and T_{ref} is a reference temperature. The temperature dependence of the characteristic time was neglected for simplicity. In order to achieve a steady state of the simulated extruder and to be able to evaluate the data accordingly, at least 20 s of operating time were simulated. For this purpose, an initial timestep of 0.001 s was set and then calculated with automatic time step size at a Courant Number of 0.2. The relationship between the Courant Number and the time step size is described by Equation 3.11,

$$\Delta t \leq \frac{Cl_0}{v_{max}} \tag{3.11}$$

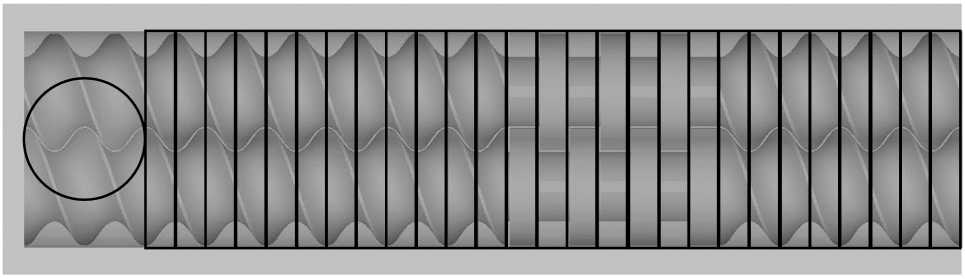

Figure 3.3: Division of the extruder into 27 sections to calculate the mean values of the quantities of interest. Each division has a width of 2.75 mm, corresponding to the width of a kneading disc.

where l_0 is the distance between particles and v_{max} is the maximum flow velocity. To further stabilize the simulation, a velocity limiter was activated. Particles with a calculated velocity higher than $0.4\,\mathrm{m\,s^{-1}}$ were slowed down to a velocity of $0.4\,\mathrm{m\,s^{-1}}$. The selected velocity is about 20 % higher than the maximum circumferential velocity of the rotating screws ($0.33\,\mathrm{m\,s^{-1}}$). In the results analysis, it was observed that only a few particles located in the gap between the two screws were throttled. The calculations were carried out on a Nvidia GeForce RTX 3090 graphics card of a workstation with 64 gb RAM. The calculations took between 2 hours for the setting with the largest particles (0.6 mm - 8,000 particles) to up to 25 days for the simulation with the smallest particles (0.1 mm - 3.5 million particles) (see figure 3.4).

3.2.3 Evaluation of the collected simulation data

In order to obtain values of the quantities of interest, the extruder was divided into 27 segments. When dividing the extruder, the first pair of conveying elements was disregarded, as this is where the particle inflow took place. The length of the divisions in the axial conveying direction corresponds to the length of a kneading disc. A representation of the division is given in figure 3.3. Quantities that are considered along the extruder are the degree of filling, the mean particle age, the mean stress tensor, and the mean temperature. The mean value of the quantities was formed by taking the average of all particles in a segment. The degree of filling was calculated according to Equation 3.12,

$$f = \begin{cases} \frac{N_P d_P^3}{V} \frac{n_0}{n_i} & n_i > n_{prim} \\ \frac{N_P d_P^3}{V} & n_i \leq n_{prim} \end{cases} \tag{3.12}$$

where N_P is the number of particles, d_p is the particle diameter, n_{prim} is the particle number density of a primitive ball pack, and V is the free volume. A correction with primitive ball pack is needed as particles sometimes shift slightly into each other resulting in an increased particle number density compared to the inflow particle number density (primitive ball pack).

The particle age corresponds to the time that a particle exists in the screw section after having been generated in the inflow. The local residence time in the kneading blocks was calculated from the difference between the particle age when flowing out of the kneading blocks (t_{out}) and the particle age when flowing into the kneading blocks (t_{in}). The stress tensor was used to consider the mechanical stress profile and is given by Equation 3.13,

$$\tau = 2 * \eta * \mathscr{D} \tag{3.13}$$

with

$$\mathscr{D} = 1/2 * (\nabla \mathbf{v} + \nabla \mathbf{v}^T) \tag{3.14}$$

where η is the dynamic shear viscosity, D is the deformation tensor and $\mathbf{v}$ is the velocity.

3.2.4 Extrusion experiments for physical reliability evaluation

Extrusion trials were performed on a laboratory-scale twin-screw extruder Process 11 (ThermoFisher Scientific Inc., Waltham, MA, USA). The screw diameter is 11 mm and the length-diameter (L/D) ratio of the extruder is 40. Since the die section was not of interest, no die was mounted in the die adapter. Commercial soy protein isolate (SPI) Supro ST from Solae LLC (St. Louis, MO, USA) was dosed via a gravimetrically controlled feeder of Brabender Technology GmbH (Duisburg, Germany) into the first barrel element. The water feed was pumped via a peristaltic pump Masterflex L/S of Cole Parmer (Vernon Hills, IL, USA) in the third barrel element. Three different screw configurations were investigated, consisting of forward elements as well as kneading blocks analogous to the simulated kneading blocks depicted in figure 3.1. The kneading blocks have a distance of 5 L/D to the last conveying element before the die adapter. The screw speed was held constant at 600 rpm. The mass flow rate of the dosed SPI and the pumped water was held constant at $0.7\,\mathrm{kg\,h^{-1}}$ each. The temperature profile of the barrel was 40 °C in the first zone, 60 °C in the second zone, 80 °C in the third zone, and 100 °C in the following 3 zones. Accordingly, the kneading blocks are located in a section that is tempered to 100 °C.

Deadstop experiments were carried out to obtain the degree of filling. After the extrusion process was in a stationary state, the extrusion process was stopped abruptly. The upper half of the barrel was then removed and a picture of the screws filled with material was taken.

3.3 Results and discussion

3.3.1 Particle size investigation

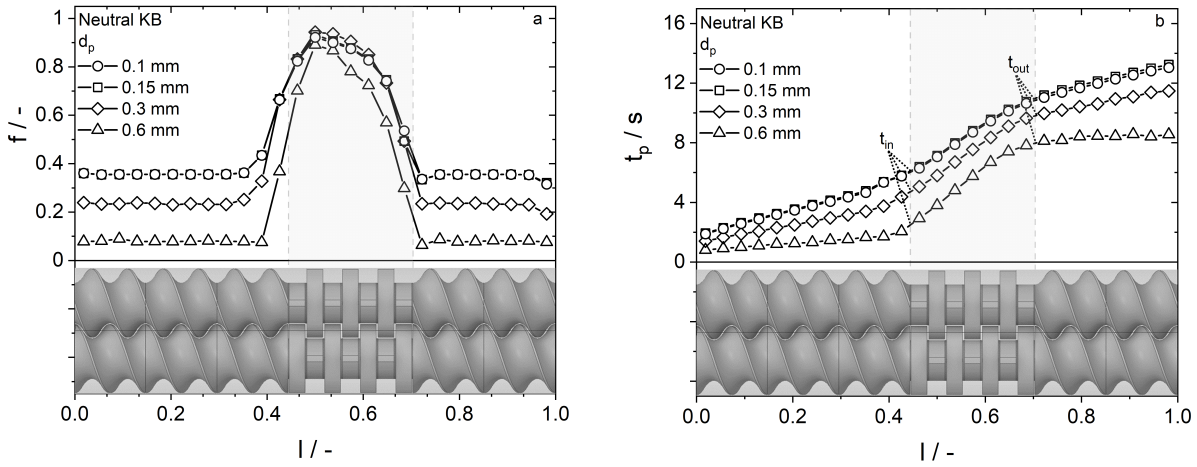

Figure 3.4: Influence of the MPS particle diameter on the conveying behaviour examined by the degree of filling (a) and the mean particle age (b).

Initially, the influence of the particle size on the conveying and filling behaviour in the twin-screw extruder model was investigated. The screw configuration with neutral kneading blocks was used for the investigation. It is known from literature that the use of neutral kneading blocks leads to a build-up of material due to a lack of conveying capacity (Kohlgrüber, 2019). In figure 3.4 a the degree of filling is plotted over the length of the screw for various particle sizes. It can be observed for all particle sizes, that a constant degree of filling is achieved in the area of the conveying elements and that the degree of filling rises in the area of the kneading blocks. The value of the degree of filling for the conveying elements increases with decreasing particle size and is the same for 0.15 mm and 0.1 mm. There are two possible reasons for this. Particles smaller than the gap between the barrel and the rotating screw (0.2 mm) are no longer force-conveyed by the rotation of the screw. This creates a layer of particles on the surface of the barrel, which contributes to an increase in the degree of filling. The neutral kneading block has no conveying capacity. This results in a build-up of particles regardless of the particle size. It can be observed that the degree of filling seems to be independent of the particle size, except in the case of a particle size of 0.6 mm. The highest degree of filling of 0.96 is found at the position of the second kneading disc. The flow restriction is highest at this point. Afterwards, the degree of filling decreases over the length of the remaining kneading blocks, until it reaches the constant level of the conveying elements again.

With a plot of the mean particle age over the length of the screw, shown in figure 3.4b, a correlation to the degree of filling can be observed. In the sections of the conveying elements, where the degree of filling was constant for each particle size, the increase in the mean particle age over the screw length is linear. As the particle size decreases, with the exception of particles with a size of 0.1 mm, the mean particle age increases in accordance with the degree of filling. In the

kneading blocks, where the degree of filling was almost constant for the different particle sizes, the mean particle age increases to about the same extent for all particle sizes ($t_{in} - t_{out} = 4.9\,\mathrm{s}$ (0.1, 0.15 mm), 5.1 s (0.3 mm), and 5.5 s (0.6 mm)). This can be attributed to the fact, that the mean residence time in a fully filled area is only defined by the given mass flow rate. For further simulations, a particle size of 0.15 mm was chosen, as the computing time was still acceptable (12 days) and the results considered were no longer influenced by the particle size. However, by choosing this particle size, only one particle fits into the narrowest gap. Accordingly, shear peaks can be shown, but the flow in the gap cannot be resolved more precisely. This problem is known and also accepted in simulations with SPH (Eitzlmayr and Khinast, 2015). Wittek et al. have shown that SPH is quite capable of adequately solving the gap if the particles are chosen small enough and correspondingly long computation times can be accepted (Wittek et al., 2018). However, the main objective of this work is to collect information about the degree of filling, residence time, and thermomechanical profile over a large section of the extruder, which would have made the computational effort prohibitive.

3.3.2 Variation of the kneading disc offset angle

It is known that a variation of the kneading block offset angle leads to changes in the residence time distribution and the degree of filling and thus influences the thermomechanical energy input (Sarhangi Fard and Anderson, 2013). Therefore, simulations with different kneading blocks were carried out to further test the simulation set up. Figures 3.5a and 3.5b plot the degree of filling and the mean particle age over the length of the screw under variation of the kneading block geometry. For the first conveying elements, up to a screw length of 0.24, the degree of filling is not influenced by the kneading blocks for any geometry, and the value is constant for all geometries. Subsequently, at 0.28, an increase in the degree of filling can be seen for the backward kneading blocks. For the neutral kneading blocks, an increase can be found at 0.34 and for the forward kneading blocks at 0.38. This result was to be expected, as it is known that backward kneading blocks restrict the flow to a greater extent than neutral kneading blocks and forward kneading blocks. In the kneading blocks, an effect of the conveying behaviour of the kneading blocks is evident. As the forward kneading block still has a conveying capacity, the degree of filling is only slightly increased compared to the classical conveying elements. For the backward kneading blocks, which have a negative conveying capacity, there is a more pronounced build-up of material in front of the kneading block compared to the neutral kneading block.

Also for the different geometries, a correlation between degree of filling and the mean particle age is evident. As the degree of filling increases in comparison to the classical conveying elements, the slope in the mean particle age over screw length increases. In the case of the forward kneading blocks, where the degree of filling is lowest, the slope changes only slightly and the mean particle age increases the lowest ($t_{in} - t_{out} = 3\,\mathrm{s}$). For the neutral and backward kneading blocks, where the degree of filling in the kneading blocks is almost equal, the increase in mean

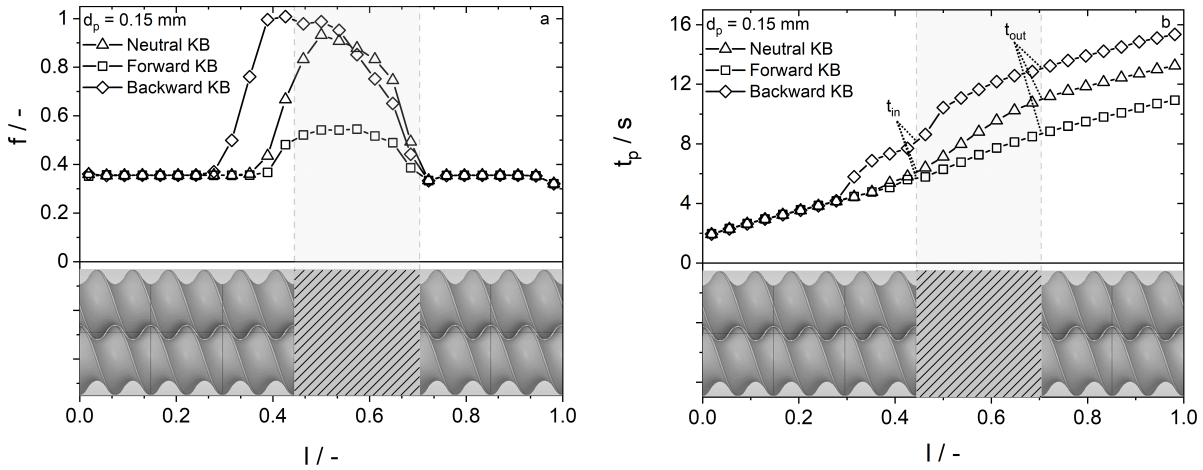

Figure 3.5: Influence of screw configuration with different kneading blocks on the conveying behaviour examined by the mean value of the degree of filling (a) and the mean residence time (b).

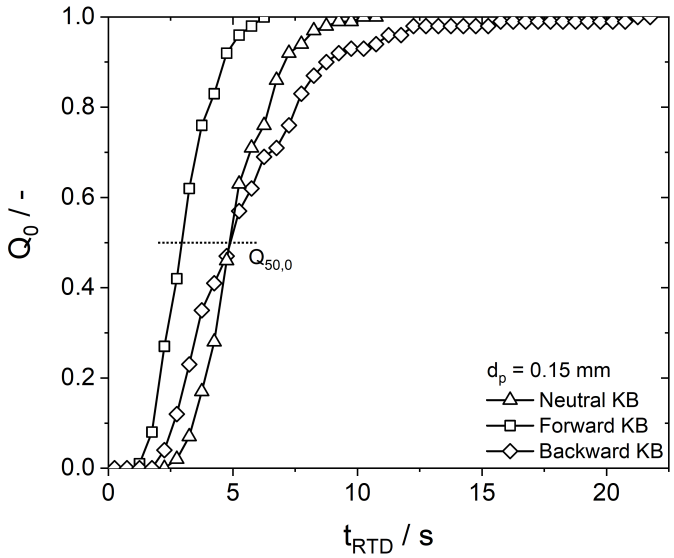

Figure 3.6: Local residence time distribution in the kneading blocks.

particle age is equal ($t_{in} - t_{out} = 4.9\,\mathrm{s}$), while the course differs. For the backward kneading blocks, there are two sharp steps. One at the first rise of the degree of filling ($l = 0.4$) and one after the first kneading disc ($l = 0.5$). These steps can be attributed to the flow restriction and backflow conveying behaviour of the backward kneading blocks. Tracking individual particles from the particle collective allows not only to form mean values of the particle age, but also to resolve the local residence time. Thus, the residence times of 100 particles flowing through the kneading blocks were determined, and a residence time distribution was formed. For each kneading block configuration, the residence time distribution is shown in figure 3.6. It can be seen that the mean residence time of the forward kneading blocks is lower ($Q_{50,0} = 3\,\mathrm{s}$) than the mean residence time of the neutral and the backward kneading blocks, which are the same size ($Q_{50,0} = 4.9\,\mathrm{s}$). Likewise, the width of the distribution is narrowest for the forward kneading blocks, followed by the neutral kneading blocks. The widest distribution is found for the backward kneading blocks.The differential distribution of the residence time for the different kneading blocks is also given in the supplementary material (figure 8.1). It is clear that the width

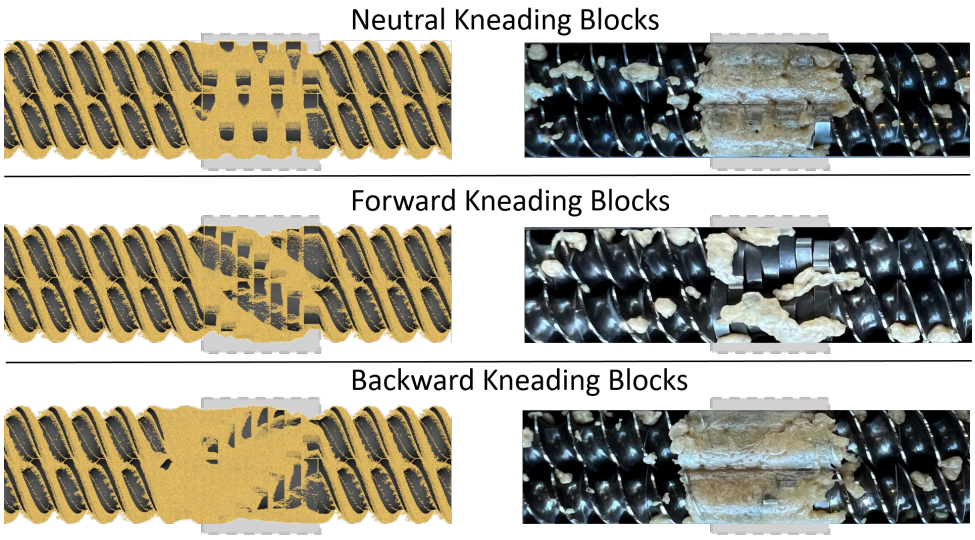

Figure 3.7: Comparison of the filling behaviour of the simulated domains (left) and deadstop experiments (right). The kneading blocks are highlighted in gray. Experiments and simulations were performed under the same process conditions (mass flow rate, screw speed).

of the distribution between the forward and the neutral kneading block differs only slightly, whereas the backward kneading block has a clearly broader distribution. The lower mean residence time of the forward kneading blocks and the coincidence of the mean residence time of the neutral kneading blocks and the backward kneading blocks can be attributed to the degree of filling. The degree of filling in the forward kneading blocks is lowest and almost identical for the neutral and backward kneading blocks. Taking into account that the mean residence time is determined by the set volume flow, which is constant for all geometries, the differences can be explained according to the accumulated volume. It becomes apparent from the different widths of the residence time distributions that an exclusive consideration of the mean residence time is not sufficient to adequately describe the extrusion process. For the extrusion of reactive materials, such as proteins, a broad residence time distribution means a broad variance in product properties.

3.3.3 Optical evaluation of physical reliability

To obtain experimental data for qualitative optical validation of the numerical simulations, extrusion trials with same processing conditions (massflow, screw speed, screw configuration) were carried out. Once a steady state of the extrusion process was reached, the extruder was turned off leading to an immediate stop of the screw rotation (deadstop). The upper barrel was removed, and a picture of the examined screw section was taken. Figure 3.7 compares the numerical results with the experimental pictures for the three investigated screw configurations. In the numerical simulations, a constant fluid volume can be found in the conveying section. The particles mainly accumulate in the area in front of the screw flight, close to the barrel wall. This can be explained as the viscous forces of the material dominate the gravitational forces (de Graaf et al., 1990). In contrast, in the experimental investigation, a lump formation of material in the

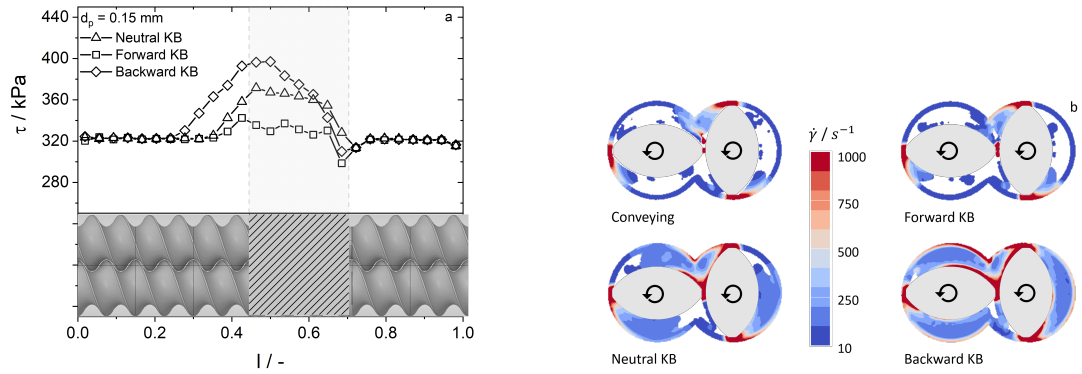

Figure 3.8: Representation of the mechanical stress in the form of the mean stress tensor over the length of the screw (a) as well as the velocity gradient distribution at selected positions (b).

area of the conveying elements can be seen. This is due to the fact, that the material is a visco-elastic fluid, which has a higher elastic than viscous content (Wittek et al., 2020). Embedding visco-elastic data is very challenging for two reasons. Firstly, the numerical computation of three-dimensional visco-elastic models takes a significant amount of time. Secondly, there are no measurement methods available to determine such data under extrusion-relevant conditions. Thus, a quantitative statement about the degree of filling is not possible.

For the kneading blocks, a good qualitative agreement is observed for all kneading block configurations. For the neutral kneading blocks, an apparently completely filled section can be seen, while for the forward kneading blocks, only an accumulation of the material along the disc flights can be seen. The backward kneading blocks have a reverse conveying capacity, causing a build-up of material in front of the kneading blocks. As a result, an apparently completely filled section can be observed in the kneading blocks and around half a conveying element in front of it.

3.3.4 Mechanical and thermomechanical stress profile

In extrusion processing, the thermal and mechanical energy inputs should not be considered separately from each other. Due to the high shear viscosity of extruded materials, viscous energy dissipation leads to not negligible heating. However, the numerical simulation allows to neglect the heating. Thus, it is possible to consider the pure mechanical energy input of different screw configurations, decoupled from the heating that leads to a change in shear viscosity. Figure 3.8a shows the mean stress tensor along the screw length for the screws with the different configurations of kneading blocks under isothermal conditions. The mean stress tensor for the different geometries is analogous to the course of the filling ratio, depicted in figure 3.5a. For the first conveying elements, the mean stress tensor has a constant value. Once the degree of filling changes, the mean stress tensor changes as well. The mean stress tensor is highest for the backward kneading blocks and is already increased upstream the kneading blocks at the conveying elements. In the other configurations, the mean stress tensor increases only slightly

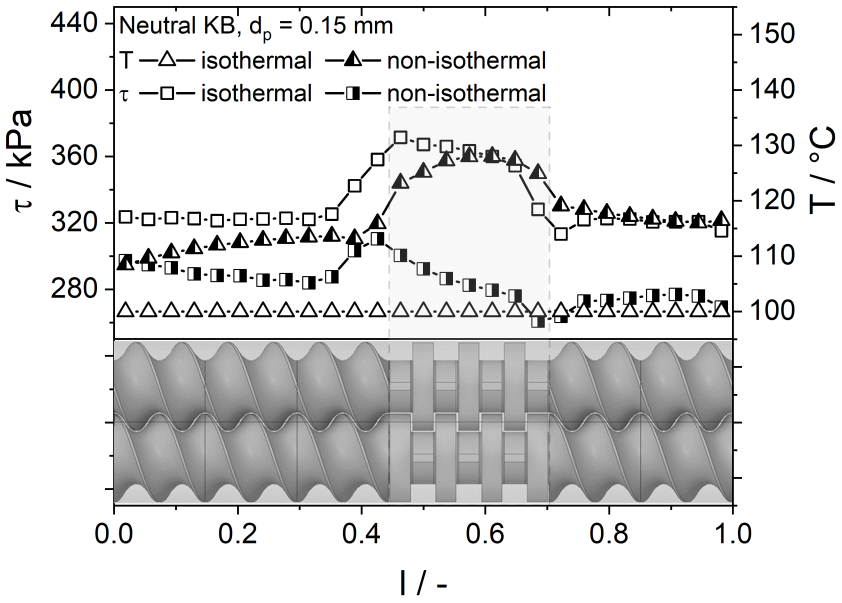

Figure 3.9: Mean value of the stress tensor and the temperature along the screw length for the screw configuration with neutral kneading blocks.

in front of the kneading blocks, but mainly in the kneading blocks themselves and is higher in the neutral kneading blocks than in the forward kneading blocks. The differences in the mean stress tensor can be attributed to different velocity gradient distributions resulting from a different degree of filling and flow restriction. The velocity gradient distribution in different cutting planes is depicted in figure 3.8b. As expected, for all elements, the highest velocity gradients ($\dot{\gamma} > 1000\,\mathrm{s}^{-1}$) can be found in the gap between the screw flight and the barrel, as well as between the screw flight and the neighbouring screw. For the conveying elements and the forward kneading blocks, these areas are the only ones where high velocity gradients can be observed. For the neutral kneading blocks and the backward kneading blocks, where the degree of filling is increased, larger areas with high velocity gradients are present at the barrel wall and the core of the screw. The increase in the mean stress tensor is thus due to the locations of increased velocity gradients. The increase in velocity gradient is due to the change in momentum transfer with increasing degree of filling as well as to the flow restriction of the subsequent kneading discs at the neutral and backwards kneading blocks.

For highly viscous materials, such as the soy protein isolated used in this study, viscous energy dissipation leads to a non-negligible temperature increase. Figure 3.9 plots the mean stress tensor and the material temperature over the screw length for the screw with neutral kneading blocks, with and without consideration of the energy equation. Taking the energy equation into account, as expected, a heating of the material takes place. The material in the conveying element section heats up only slightly, whereas the temperature in the kneading blocks rises abruptly by more than 10 K. After the kneading blocks, the material cools down again until it reaches an almost constant level. The local temperature peak in the kneading blocks can be attributed to two effects. On the one hand, it was shown in figure 3.8 that the mechanical stress increases in the kneading blocks. Accordingly, more heat is generated through viscous energy

dissipation. But more important is that the heat can be transferred more poorly to the barrel because the ratio of barrel surface to filled material is decreasing with increasing degree of fill. The increase in temperature results in a decrease in shear viscosity and consequently in a reduced mean stress tensor compared to the isotherm simulation. This clarifies that a separate consideration of the thermal and mechanical stress profiles in twin-screw extrusion is not expedient. At this point, however, it must be pointed out that the influence of the particle size on the viscous energy dissipation and correspondingly the temperature profile was not investigated further. We suspect that if the flow in the narrow gaps is not sufficiently resolved, the viscous energy dissipation is overestimated. The reason for this is that the velocity gradient is overestimated. Despite a potential reduction in shear viscosity, the dominance of the velocity gradient still governs the viscous energy dissipation ($\Delta e = \eta \dot{\gamma}^2$). Accordingly, it is recommended for future publications to investigate this issue in more detail, as it has not yet been sufficiently investigated.

3.4 Conclusion

In this work, the moving particle semi-implicit simulation method was successfully used to obtain information about local process conditions in the screw section of a twin-screw extruder. First, the influence of particle size on the simulation results of interest was investigated. It was shown that for varied particle sizes smaller than the gap between screw and barrel, there are no differences in the degree of filling and the mean residence time. Varying the offset angle of the kneading discs in the kneading blocks changes the conveying behaviour of the kneading blocks, resulting in different filling degrees and mean residence times. As expected, the degree of filling and the residence time increase from the forward kneading blocks, to the neutral kneading blocks, to the backward kneading blocks. By considering individual particle trajectories, it was possible to determine residence time distributions within the kneading blocks. It was found that the different kneading blocks have different broad distributions, but that the mean residence time of the neutral kneading blocks and the backward kneading blocks coincide. The mean residence time of the forward kneading blocks is lower because the degree of filling is lower. Considering the mechanical stress profile, it could be shown that within the kneading blocks, there are different degrees of stress, which was attributed to the degree of filling and the different flow restrictions due to the kneading discs, orientations. An optical comparison of the simulations with experimental deadstops showed a good agreement in the degree of filling for the different kneading blocks. The non-isothermal simulation has shown that viscous energy dissipation can cause local temperature peaks within the fully filled kneading blocks, which would not have been recorded if the temperature had been determined integrally. However, the simulation does not yet take into account the reactivity of the material, the narrowest gap in the extruder is only moderately resolved, and the elastic properties of the material are neglected. To further improve the simulation model, this should be taken into account in further research.

4 The Ramp Test From a Closed Cavity Rheometer

Chapter 4 is published as: F. Ellwanger, C. K. Georgantopoulos, H. P. Karbstein, M. Wilhelm, and M. A. Emin Application of the ramp test from a closed cavity rheometer to obtain the steady-state shear viscosity. *Applied Rheology 33(1): 20220149* (2023). doi: 10.1515/arh-2022-0149. Text, tables, figures and equations have been edited and reformatted for consistency.

Abstract

The steady-state shear viscosity η is required in controlling processing parameters for the extrusion processing of polymer melts. A new method, the so-called ramp test, is investigated in this study to obtain the steady-state shear viscosity with a closed cavity rheometer (CCR). To verify the method and the accuracy of the CCR data, three commercial polyolefin polymers, a low-density polyethylene (LDPE), a linear low-density polyethylene (LLDPE), and a polybutadiene (PBD), were used as model systems. Measurements of the magnitude of the complex viscosity $|\eta^*|$ were compared with the steady-state shear viscosity data obtained by capillary rheometer and CCR. Further, time–temperature superposition master curves of the magnitude of the complex viscosity and steady-state shear viscosity obtained by CCR were developed for LLDPE and PBD. The influence of the cavity sealing on the instrument's accuracy to obtain the steady-state shear viscosity was investigated using the finite element method simulations. Thus, it was shown that the ramp test performed by CCR is a practical method to determine reliable and reproducible data of the steady-state shear viscosity within a wide range of temperatures (50–180 °C) for low and high viscous materials (1.6–480 $kPa \cdot s$, 144–375 $kg \cdot mol^{-1}$).

4.1 Introduction

Screw extrusion processing is a common process used to produce films, chemicals, and tires as well as food products such as pasta, cereals, or meat substitutes. For all these processes, the rheological behavior of the material used has a crucial role at various levels. This includes process control and stability as well as product properties and mechanical performance. Therefore, there is a significant effort to measure the rheological properties of the materials used under processing conditions in shear and elongation flows. Among others, the steady-state shear viscosity η (also referred to as shear viscosity) is of high interest, as it determines the torque required for extrusion. In addition, the mechanical stress profile during extrusion and the temperature reached in the screw section depend on the shear viscosity due to viscous heating (Kohlgrüber, 2019). In the die section, the shear viscosity also determines the flow conditions. Therefore, shear viscosity is of great interest for the control of extrusion processing for polymers (Vittorias et al., 2011; Georgantopoulos et al., 2022; Hatzikiriakos, 2012) and for food products, i.e., meat replacers (Wittek et al., 2021a; Pietsch et al., 2019b; Guyony et al., 2022).

The viscosity of a fluid is the flow resistance force caused by the internal friction of the molecules (Mezger, 2021). Using a rotational rheometer, two different viscosities can be obtained depending on the measuring procedure. On the one hand, in the linear regime, the magnitude of the complex viscosity $|\eta^*|$ (also referred to as complex viscosity) can be obtained by applying a small amplitude oscillatory shear (SAOS) flow. The complex viscosity $|\eta^*|$ is defined as $|\eta^*| = \sqrt{G'^2 + G''^2}/\omega$ where G' is the storage modulus, G'' is the loss modulus, and ω is the angular frequency. On the other hand, in the nonlinear regime, the shear viscosity η is defined as $\eta = \sigma/\dot{\gamma}$, where $\dot{\gamma}$ is the shear rate and σ is the shear stress. The complex viscosity $|\eta^*|$ and the shear viscosity η are linked via the empirical Cox–Merz rule, which is widely used in the industry (Cox and Merz, 1958). The rule originally established by Cox and Merz showed that the complex viscosity $|\eta^*|$ obtained by a rotational rheometer is very close to the apparent shear viscosity η_{app} measured by capillary rheometer, for equality of the frequency ω and the shear rate $\dot{\gamma}$ ($|\eta^*| = \eta_{app}$ for $\dot{\gamma} = \omega$). The applicability of the Cox–Merz rule to the shear viscosity η and the complex viscosity $|\eta^*|$ has been established for many polymer melts, concentrated systems, and semi-dilute systems ($|\eta^*| = \eta$ for $\dot{\gamma} = \omega$). For example, a detailed investigation on the appraisal of the Cox–Merz rule for polyolefin melts can be found in the work of Snijkers and Vlassopoulos (Snijkers and Vlassopoulos, 2014).

Furthermore, the comparison of the shear stress σ and the complex shear modulus $|G^*|$ ($\sigma = |G^*|$ for $\dot{\gamma} = \omega$) proposed by Winter is used to draw an additional conclusion about the viscoelasticity of the investigated material (Winter, 2009). Since the Cox–Merz rule is an empirical rule for which no final justification has been provided, it is not recommended to use the complex viscosity to predict the shear viscosity for unknown materials. In the context of this publication, it is assumed that the Cox–Merz rule is typically valid within a 15% deviation between the complex viscosity and the shear viscosity. This assumption is made to cover possible measurement inaccuracies of the different devices and measurement routines used.

Table 4.1: Advantages, disadvantages, and typical limitations of open cavity rheometers, capillary rheometers, and CCR

	Open cavity oscillatory rheometer	**Capillary rheometer**	**Closed cavity oscillatory rheometer**
Advantages	Low amount of material needed (1 g), versatile in measuring procedures, fast temperature control (30 K/min)	Feasibility of high shear rates ($\dot{\gamma} > 100 s^{-1}$), comparable with actual extrusion processes	Low amount of material needed (4.5 g), versatile in measuring procedures, fast temperature control (80 K/min), no edge fracture, pressure regulation
Disadvantages	Wall slippage, secondary flow, edge fracture, loss of lubricant/solvent	Different flow types (Couette vs Poiseuille) to compare it with rotational rheometer, wall slippage, data correction needed, large amount of material needed (> 100 g), viscous heating, extrusion flow instabilities, not suitable for low shear rates	No continuous rotation, Not suitable for low viscous material, Wall slippage, Little variety of measurement geometries
Typical limitations (shear rate, temperature, torque/force)	$\dot{\gamma}$ = 0.001-1000 s^{-1}, T = -150- 600 °C, M = 0.1 μNm to 0.2 Nm	$\dot{\gamma}$ = 10-10000 s^{-1}, T = 25-600 °C, F = 10-50 kN	$\dot{\gamma}$ = 0.01-30 s^{-1}, T = 25-230 °C, M = 0.1 mNm to 25 Nm

Modern rheometers can provide reliable information on the complex viscosity, but it is still challenging to obtain reliable data on the shear viscosity for strongly viscoelastic materials. Typical advantages and disadvantages to obtain the shear viscosity are given in Table 4.1. In this context, it would be of interest, for both research purposes and industry, to have a fast and accurate method that requires the use of only a small amount of material to obtain the shear viscosity for strongly viscoelastic materials.

As Table 4.1 displays, closed cavity rheometers (CCRs) have a great potential for determining the shear viscosity compared to the capillary and open cavity rheometers. CCRs are usually equipped with a motor providing higher torque values, which enables the measurement of a high viscous material without using small geometries (r < 5mm). By applying and controlling pressure, and using plates with grooves, wall slippage can be prevented. The closed cavity set up of the CCR is eliminating the edge fracture. In addition, by the application of pressure in the closed cavity, the evaporation of solvents, i.e., water at high temperatures is avoided. A small chamber geometry (r $\approx$ 20 mm) allows a quick and accurate increase or decrease of test temperature. These rheometers are widely used to determine viscoelastic properties of rubbers and water-containing food samples (Wittek et al., 2021b; Schreuders et al., 2021b; Schwab

et al., 2016). A measurement of the shear viscosity with the CCR would therefore offer the possibility of carrying out quick, simple measurements without having to use a lot of material.

To the best of our knowledge, Buhrin et al. (2021), Buhrin and Rauschmann T. (2021), Buhrin et al. (2022) as well as Heyer et al. (2022) are the only authors to have published on determining shear viscosity data with CCR. In their work, the ramp test method, a method to obtain the shear viscosity via CCR, was introduced and mainly used to investigate the shear viscosity of rubbers. In addition, they used the ramp test in combination with a polished plate to obtain information about wall slippage. Most recently, Rauschmann et al. presented a new generation of CCR (Rubber Process Analyzer Ultra, Bareiss Prüfgerätebau GmbH, Oberdischingen, Germany), which enables continuous rotation at shear rates up to $500 s^{-1}$ (Rauschmann et al., 2022).

To further verify the ramp test method, this study presents data for a low-density polyethylene (LDPE), a linear low-density polyethylene (LLDPE), and polybutadiene (PBD). The specific choice of materials was made to present results from well-known, widely used polymers. Also, by choosing these polymers as samples, a wide range of average molecular weights and processing behaviors are investigated. Hence, in comparison to the filled system used in the previous studies, thorough conclusions by using simpler samples can be drawn about the ramp test method. First, data obtained by SAOS measurements were compared with steady-state data obtained by capillary measurements to validate the applicability of the Cox–Merz rule. The data of the complex viscosity for the three polymers were fitted by the Cross model (Morrison, 2001). The Cross model found for LDPE was used for numerical finite element simulations to investigate the theoretical influence of the cavity sealing on the CCR's accuracy. Subsequently, measurements were performed with the CCR to obtain the shear viscosity of the same LDPE, LLDPE, and PBD.

To demonstrate the potential of the ramp test and the accuracy of the CCR, SAOS and shear measurements were carried out for LLDPE and PBD at different temperatures. The data obtained were used to construct master curves using the time–temperature superposition (TTS) principle (Mavridis and Shroff, 1992). The horizontal a_T and vertical b_T shifting factors were chosen based on the SAOS measurements and could be used for both the complex viscosity and the shear viscosity data.

4.2 Materials

The materials used in this study were LDPE, LLDPE, and PBD. The melting temperature and the molecular characteristics (number average molecular weight M_n, average molecular weight M_w, and polydispersity Đ($\frac{M_n}{M_w}$) are listed in Table 4.2. The molecular characteristics of LDPE and LLDPE have been obtained by a high-temperature size exclusion chromatography (SEC) coupled with a multi-angle laser light scattering technique at 140 °C. Linear polyethylene (PE) standards were used for column calibration. The molecular weight distribution of the investigated PBD was detected by the size exclusive chromatography equipped with a differential refractive index detector. Homopolymer PBD standards with linear molecular architecture were used for column calibration.

Table 4.2: Melting temperature and molecular characteristics of the investigated LDPE, LLDPE, and PBD

	Melting temperature (°C)	**Glass transition temperature** (°C)	M_n $(kg \cdot mol^{-1})$	M_w $(kg \cdot mol^{-1})$	**Đ**
LDPE	114	-	23.7	146	6.16
LLDPE[1]	125	-	32.7	144	4.40
PBD[2]	-	-108	107	375	3.50

[1]Adapted from Georgantopoulos et al. (Georgantopoulos et al., 2023)
[2]Adapted from Georgantopoulos et al. (Georgantopoulos et al., 2022)

4.3 Experimental and computational rheological measurements

4.3.1 The magnitude of the complex viscosity

To determine the complex viscosity $|\eta^*|$, frequency sweep experiments were performed with a CCR, also called rubber process analyzer (RPA) flex, from TA Instruments, Inc. (New Castle, DE, USA), as shown in figure 4.1. The CCR is equipped with a grooved cone-cone geometry (r = 20.625 mm, $\theta = 7.16°$). The grooves in the cones are used to prevent wall slippage. The experiments were carried out within the linear viscoelastic regime (LVE) in an angular frequency range between 0.05 and 315 $rad \cdot s^{-1}$. The strain sweeps performed to determine the LVE range are shown in figure 9.3 in the supplementary material. For LDPE and LLDPE, a strain of 10%, and for PBD, a strain of 1% was chosen to obtain an accurate signal in the low-frequency range. Before each measurement, the material was held at the zero position for 3 min to ensure a homogenous temperature profile. Measurements were performed at least in duplicate to determine measurement errors.

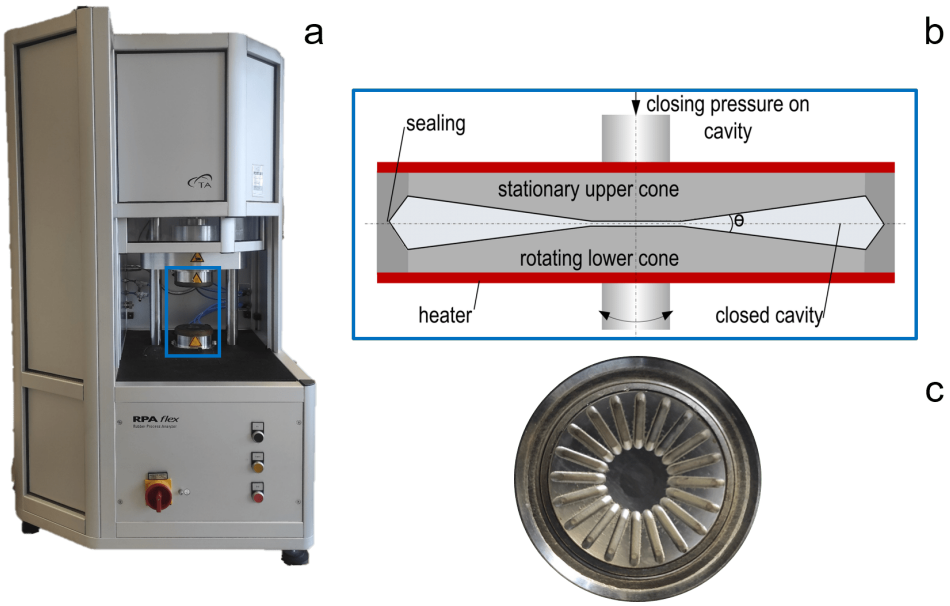

Figure 4.1: CCR named as RPA by TA Instruments. (a) CCR, (b) function sketch closed cavity (Emin et al., 2017), and (c) grooved lower cone.

4.3.2 Steady-state shear viscosity

To determine the shear viscosity η via different methods, experiments were performed with the aforementioned CCR and a capillary rheometer Göttfert RG 50 from Göttfert Werkstoff-Prüfmaschinen GmbH (Buchen, Germany).

For the capillary rheometer experiments, the sample was loaded in the capillary rheometer reservoir (30 mm reservoir diameter) and remained there for 15 min to ensure a homogenous temperature profile. In total, three commercial round capillary dies (with circular cross-section area) with a length of 30, 20, and 10 mm and a diameter of 2 mm were used. The raw data were corrected according to Bagley (Bagley, 1957) and Rabinowitsch (Rabinowitsch, 1929).

For the CCR, the material was held at a zero position for 3 min to ensure a homogenous temperature profile. The lower cone then deflects by a maximum of 50 (almost one rotation) at a constant rotational speed, while the torque is measured at the upper cone. This type of experiment is also known as a start-up shear experiment and is used to obtain the shear viscosity for open cavity rheometers (Snijkers et al., 2013a,c). After the full displacement, the lower cone rotates back into the zero position. The shear viscosity η can then be calculated by equation 4.1, where σ is the shear stress, $\dot{\gamma}$ is the shear rate, M is the torque at the upper cone, and r is the radius of the cone.

$$\eta = \frac{\sigma}{\dot{\gamma}} = \frac{3M}{2\pi r^3}\frac{1}{\dot{\gamma}} \tag{4.1}$$

This study has run two routines in which the shear viscosity of the sample is measured in 13 consecutive deflections. The rotational speed during deflection was chosen so that the shear rate was between 0.1 and 30 s^{-1}. Lower shear rates could not be achieved due to a poor signal-to-noise ratio. Higher shear rates could not be achieved due to limitations of the limited rotation velocity of the instruments motor. Measurements were made from low to high shear rate and in reverse. Due to the grooved plates of the geometry, it was initially assumed that slippage was prevented and that the true shear viscosity was directly obtained without any further correction.

4.3.3 Viscosity model

The complex viscosity $|\eta^*|$ as a function of angular frequency ω was fitted with a Cross model, given by equation 4.2:

$$|\eta^*| = \frac{|\eta_0^*|}{1+(\tau\omega)^n} \tag{4.2}$$

where η_0^* is the zero-shear viscosity, τ is the relaxation time, and n is the power-law index.

4.3.4 Numerical simulation

The calculation of the numerical equations was performed with ANSYS POLYFLOW ®2020 R2 by Ansys Inc. (Canonsburg, PA, USA), which provides a finite element solver for highly viscous media. The program is mainly used in the field of extrusion, for both screw extrusion and flow through dies (Wittek et al., 2021a; Avalosse, 1996; Avalosse and Rubin, 2000; Emin et al., 2017). The simulated computational domain represents the CCR; see figure 4.2 a-c. The geometric dimensions were taken from the publication of Leblanc and Mongruel (Leblanc and Mongruel, 2001). To verify the simulations and to further investigate the influence of the sealing, a simplified open cavity rheometer was also considered; see figure 4.2 d. The grooves of the geometry have been omitted to simplify mesh generation. The influence of the grooves on the shear rate may influence the accuracy, but it is not investigated in this study.

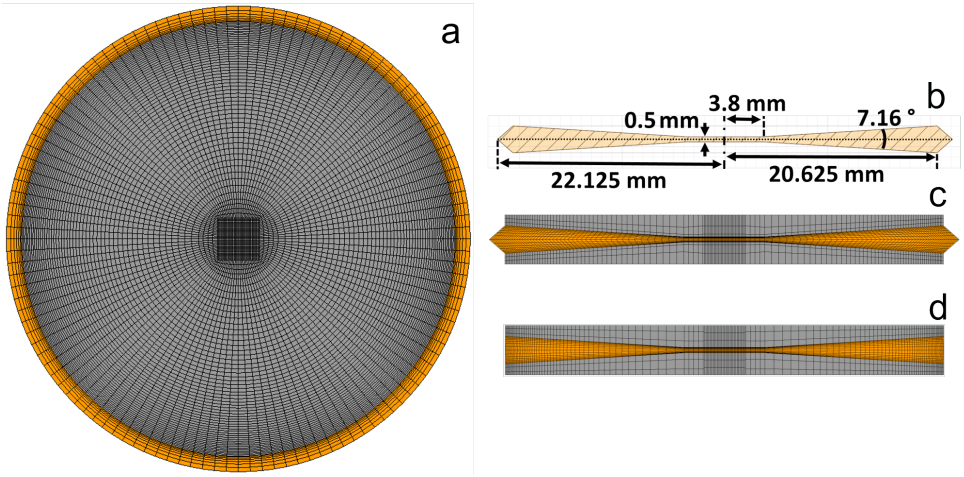

Figure 4.2: Geometry and mesh for the simulation of the CCR (orange = fluid domain, gray = rotating lower cone and stationary upper cone). (a) Top view, (b) technical drawing of the closed cavity, (c) cross-section CCR with the used computational mesh, and (d) cross-section simplified open cavity rheometer with the used computational mesh

The mesh is depicted in figure 4.2 a, c, and d and is a structured mesh, which becomes finer toward the two contact surfaces: polymer-cones and polymer-sealing. A computational mesh with 147,240 elements for the cavity and 22,140 elements for each cone was proven not to affect the simulation results numerically. To take the rotation of the lower cone and the torque measurement at the upper cone into account, the mesh superposition technique introduced by Avalosse was used (Avalosse, 1996). In this calculation technique, the mesh for the flow domain and the rotating/stationary parts are superimposed. For the CCR, the mesh of the lower rotating cone and the mesh of the upper stationary cone were superimposed on the mesh of the cavity. While solving the Navier–Stokes equations, a step function was added to check whether an element is in the flowed-through domain (cavity) or the rotating/stationary part (cone). If an element is in the flowed-through domain, the Navier–Stokes equations were solved. Otherwise, the velocity of the rotating/stationary body was assumed. Further information about this simulation method

can be found elsewhere (Avalosse, 1996; Avalosse and Rubin, 2000). A no-slip boundary condition was assumed at the surface between the cone and the cavity. This is justified due to the usage of grooved cones in the experimental investigation. For the surface between the cavity and the sealing, the no-slip boundary condition and the free-slip boundary condition were investigated. For the simplified open cavity rheometer, the open cavity surface was described as a free-slip boundary condition. The energy equation, and thus the temperature of the material, was not taken into calculation. Assuming that the Cox–Merz rule is valid for the investigated LDPE, the shear viscosity of the material is described by a Cross model (equation 4.2), which has been used to fit the experimental SAOS data (figure 4.3 a).

Mini-elements for velocity and linear pressure were chosen as interpolation settings. Iterations with a Picard scheme were performed, to take the shear viscosity implemented via a Cross model into account. To take the influence of the shear rate into account, a simulation with 25 different rotational speeds (10^{-3} to $10^{3}s^{-1}$) was carried out for the CCR at each boundary condition of the sealing-cavity surface and the simplified open cavity rheometer. The results were used to examine the actual shear rate distribution between the cones and near the sealing. In addition, the torque at the upper cone was determined, and the shear viscosity was calculated using equation 4.1. Simulations were performed on a cluster server, computing one node with 32 Intel Xeon Gold 6230 processors and 70 GB of RAM.

4.4 Results and discussion

4.4.1 Investigation of the magnitude of the complex viscosity and shear viscosity of the different polymers

The complex viscosity $|\eta^*|$ of the LDPE, LLDPE, and PBD samples was obtained by using the CCR. The data were then compared with data of the shear viscosity η obtained by a capillary rheometer Göttfert RG50. To obtain the complex viscosity, SAOS measurements were performed at typical processing temperatures of 180 °C for LDPE, 160 °C for LLDPE, and 100 °C for PBD in the linear viscoelastic region. In figure 4.3 a–c, the complex viscosity $|\eta^*|$ is plotted as a function of the angular frequency ω , and the shear viscosity η is plotted as a function of the shear rate $\dot{\gamma}$, black and red symbols, respectively. For the considered range of 0.05–315 $rad \cdot s^{-1}$, a shear-thinning behavior with a slope of 0.6 for LDPE, 0.55 for LLDPE, and 0.65 for PBD can be observed. In the low-frequency range ($\omega < 1\ rad \cdot s^{-1}$), a change in the slope can be observed, indicating the start of the zero shear viscosity plateau. The shear-thinning behavior is typical of polymers and is well known for LDPE, LLDPE, and PBD. The Cross model (equation 4.2) was suitable to describe the data of the SAOS measurements. The Cross model fitting parameters for LDPE, LLDPE, and PBD are listed in Table 4.3. The zero shear viscosity of the different polymers was estimated as it was not in the shear rate range studied and is not of interest for this investigation. To assess whether the Cox–Merz rule applies to the three commercial polymers, a 15% deviation was added to the Cross model (dashed gray lines). The assumption that the Cox–Merz rule applies despite a 15% deviation was made to consider possible measurement inaccuracies of the devices and measurement routines used. In particular, data obtained by the capillary rheometer can be affected by slippage, viscous heating, pressure effects, and other instabilities (Table 4.1).

Table 4.3: Fitting parameters of the Cross model under the following conditions: (a) LDPE at 180°C; (b) LLDPE at 140, 160, and 180°C; and (c) PBD at 50, 100, and 150°C

$$|\eta^*| = \frac{|\eta_0^*|}{1+(\tau\omega)^n}$$

	T (°C)	$\lvert\eta_0^*\rvert$ $(kPa \cdot s)$	τ (s)	n (-)
LDPE	180	52	7	0.6
LLDPE	140	36	0.7	0.55
	160	22.5	0.45	0.55
	180	17.5	0.32	0.55
PBD	50	2,790	155	0.65
	100	930	47	0.65
	150	413	19	0.65

To prove the applicability of the Cox–Merz rule, data for the shear viscosity of LLDPE and PBD were taken from the literature (Georgantopoulos et al., 2023, 2022). To obtain data for the shear viscosity of LDPE, measurements were carried out with a capillary rheometer. The data were corrected to Bagley and Weißenberg-Rabinowitsch correction as given in Hatzikiriakos and Migler (Hatzikiriakos and Migler, 2004) Consequently, the shear viscosity η is plotted against the shear rate $\dot{\gamma}$ in figure 4.3 a–c (red triangles). The steady-state data for the LDPE (figure 4.3 a) shows a shear thinning behavior with a slope of 0.6 for the entire measuring range. The values are about 15% higher than the values of the complex viscosity. Therefore, in the context of this investigation, it can still be assumed that the Cox–Merz rule applies in the investigated shear rate range. It is not a common observation that the shear viscosity exceeds the values of the complex viscosity, but this has been reported for LDPE samples in the literature (Snijkers and Vlassopoulos, 2014; Booij et al., 1983). However, there is experimental evidence that shows an agreement of the viscosities for a LDPE sample and thus validity of the Cox–Merz rule (García-Franco, 2013).

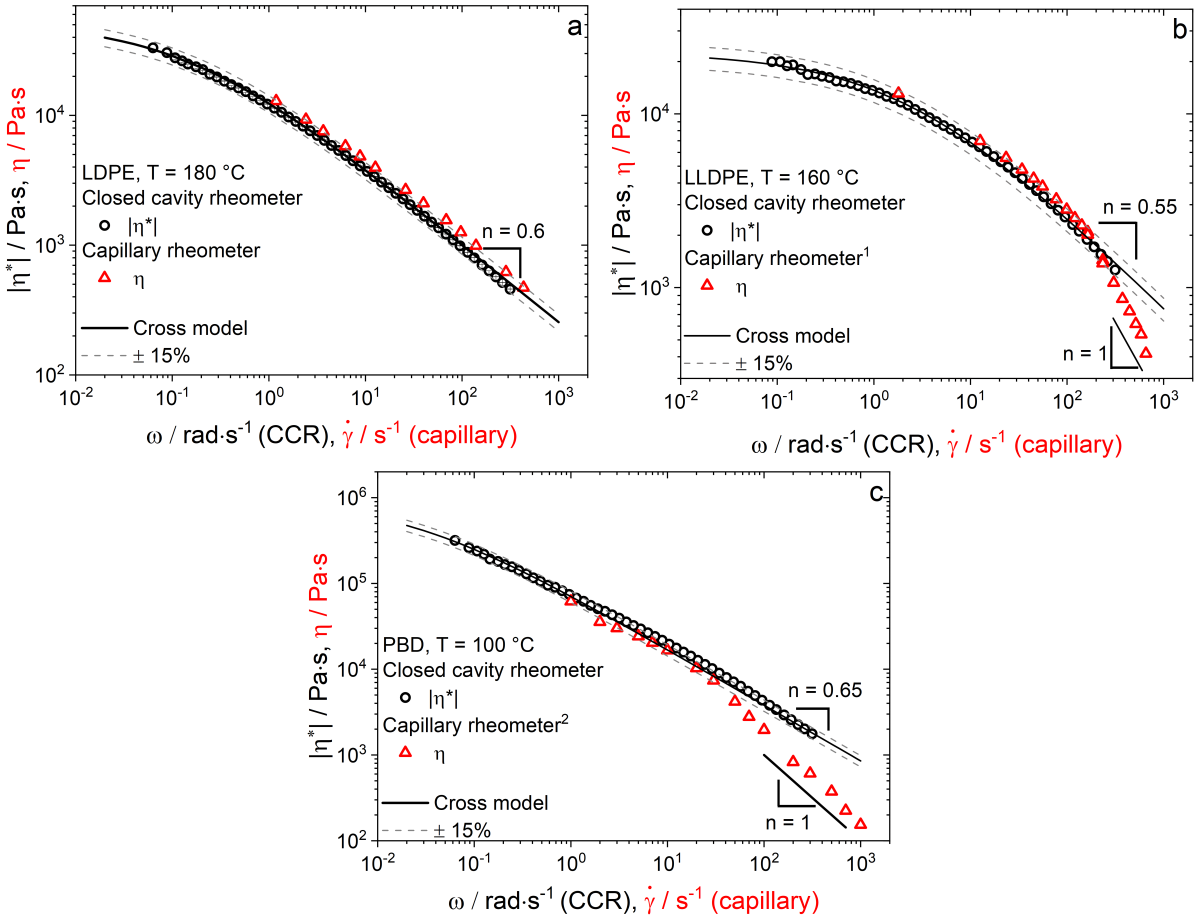

Figure 4.3: The complex viscosity $|\eta^*|$ as a function of angular frequency ω obtained by SAOS measurements with the CCR and the shear viscosity η as a function of shear rate $\dot{\gamma}$ obtained by the capillary rheometer, corrected by Bagley and Weißenberg-Rabinowitsch for (a) LDPE at180°C and (b) LLDPE at 160°C ([1] shear viscosity data adapted from Georgantopoulos et al. (Georgantopoulos et al., 2023); figure 7a) and (c) PBD at 100°C ([2] shear viscosity data adapted from Georgantopoulos et al. (Georgantopoulos et al., 2022); figure 9c).

For the LLDPE at 160 °C (figure 4.3 b), a shear thinning behavior with a slope of 0.55 can be found up to shear rates of 163 s^{-1}. In this range, the shear viscosity is within the 15 % deviation of the Cross model found for the complex viscosity. Thus, it can be assumed that the Cox–Merz rule is valid within a 15% deviation in the shear rate range of 2–163 s^{-1} at 160 °C. The shear viscosity for shear rates above 163 s^{-1} shows a decrease in the slope up to a slope of 1. A decrease in the slope of the shear-thinning behavior is often reported in the context of capillary rheometer measurements of polymer melts and is mainly related to wall slippage (Hatzikiriakos and Dealy, 1992; Hatzikiriakos, 2012; Ansari et al., 2011, 2013). Accordingly, it is assumed here that the deviation is due to wall slippage.

The steady-state data for PBD at 100 °C (figure 4.3 c) show a shear thinning behavior with a slope of 0.65 up to a shear rate of 20 s^{-1}. Up to this shear rate, the shear viscosity is below but within the 15% deviation of the Cross model found for the SAOS measurements, except for an outlier at 2 s^{-1}. For shear rates higher 20 s^{-1}, a decreasing slope up to a slope of 1 can be seen. As already described for the LLDPE, a decreasing slope can be related to wall-slippage. Thus, it is assumed that the Cox–Merz rule is applicable within a 15% deviation for the investigated PBD and the deviation at shear rates higher 20 s^{-1} is due to wall-slippage.

4.4.2 Numerical investigation of the influence of the cavity sealing on the accuracy of the CCR

To investigate the influence of the cavity sealing on the accuracy of the CCR to obtain the shear viscosity, numerical investigations were performed. The possible influence of the grooves on the accuracy of the instrument was neglected. First, a simplified open cavity rheometer (figure 4.2 d) was simulated at constant rotational speed (shear rate 1 s^{-1}). Then, simulations at different rotational speeds were performed. Since it is not clear whether the material adheres to the surface of the sealing or slides during experimental conditions, both the no-slip and free-slip boundary conditions were considered as two extremes for the simulation. In figure 4.4 a, the shear rate distribution between the cones is shown for (i) the open cavity rheometer, (ii) the CCR with no-slip conditions applied to the sealing, and (iii) the CCR with slip conditions applied on the sealing. The rotational speed was chosen so that a theoretical shear rate of 1 s^{-1} results. For the open cavity rheometer (figure 4.4 a(i)), a uniform shear rate distribution can be observed. Close to the rotation center, a decreasing shear rate can be found in all configurations in figure 4.4 a. This is typical for rotational rheometers equipped with cone and cone geometry.

The results of the CCR, shown in figure 4.4 a(ii) and (iii), indicate that the sealing can have an effect on the shear rate distribution, especially close to the sealing. For the simulation with no-slip conditions shown in figure 4.4 a(ii), an increase in the shear rate to a maximum of 10.2 s^{-1} can be observed at the edge of the rotating cone and seal. At the edge of the stationary upper cone, a decrease in the shear rate to a minimum of 0.02 s^{-1} is detected. The reduced shear rate extends to the tip of the sealing, where values of 0.02 s^{-1} can be observed. This influence of the sealing on the shear rate distribution has already been reported by Leblanc and

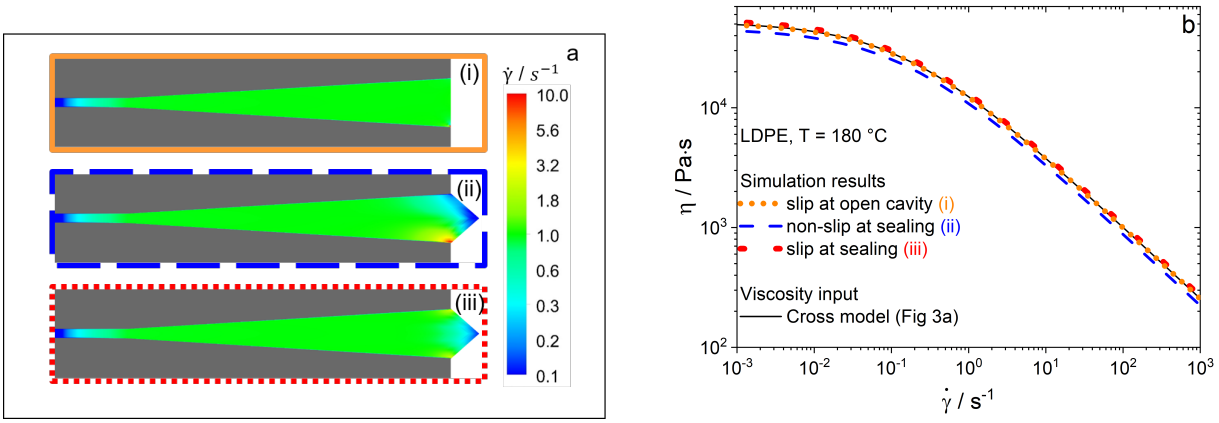

Figure 4.4: (a) Shear rate distribution between the rotating lower cone and stationary upper cone offset at 1 s^{-1} for (i) the simplified open cavity rheometer, (ii) the CCR with no-slip boundary conditions at the sealing, and (iii) the CCR with free-slip boundary conditions at the sealing. (b) Calculated shear viscosity η data for the simplified open cavity rheometer (orange dotted line), CCR with no-slip boundary conditions at the sealing (blue dashed line), and CCR with free-slip boundary conditions at the sealing (red dotted line).

Mongruel for a two-dimensional simulation of the CCR, and it is in agreement with our findings (Leblanc and Mongruel, 2001). However, the present simulation results are more detailed due to the three-dimensional simulation and additionally the use of a non-Newtonian fluid. Therefore, accurate information about the influence of the sealing is given. For the simulation with the free-slip boundary condition (figure 4.4 a(iii)), the shear rate distribution is less influenced by the sealing. At the edges of the rotating lower cone and stationary upper cone, an increase in the shear rate to a maximum of 2.3 s^{-1} can be found. At the tip of the sealing, a minimum of 0.1 s^{-1} can be detected. Accordingly, it can be observed for both simulations that the shear rate is influenced at the edge of the upper cone. Thus, an influence on the torque measurement and finally the viscosity measurement cannot be excluded and is considered in the next section.

In figure 4.4 b, the shear viscosity η determined in equation 4.1 is plotted against the shear rate $\dot{\gamma}$ for the different simulations. For the simulation with the open cavity rheometer (figure 4.4 a(i)), a deviation of less than 1% between the calculated shear viscosity and the implemented Cross model can be seen for all shear rates. This shows that the simulation is accurate enough to calculate the shear viscosity using equation 4.1. For the simulations with the no-slip boundary condition applied to the sealing, it can be observed that the shear viscosity is underestimated by equation 4.1. The deviation of the shear viscosity from the Cross model is between 11.5% for 10^{-3} s^{-1} and 12.2% for 10^{3} s^{-1}. The underestimation of shear viscosity is caused by the inhomogeneous shear rate distribution, which is a consequence of the no-slip conditions on the sealing. This reduces the shear stress close to the upper cone, resulting in a lower measured torque. The shear stress distribution between the cones can be seen in figure 9.1 in the supplementary material for the same conditions shown in figure 4.4 a. The findings of the lowered shear rate, and thus, the underestimation of the shear viscosity are in agreement with the data of LeBlanc and Mongruel (Leblanc and Mongruel, 2001).

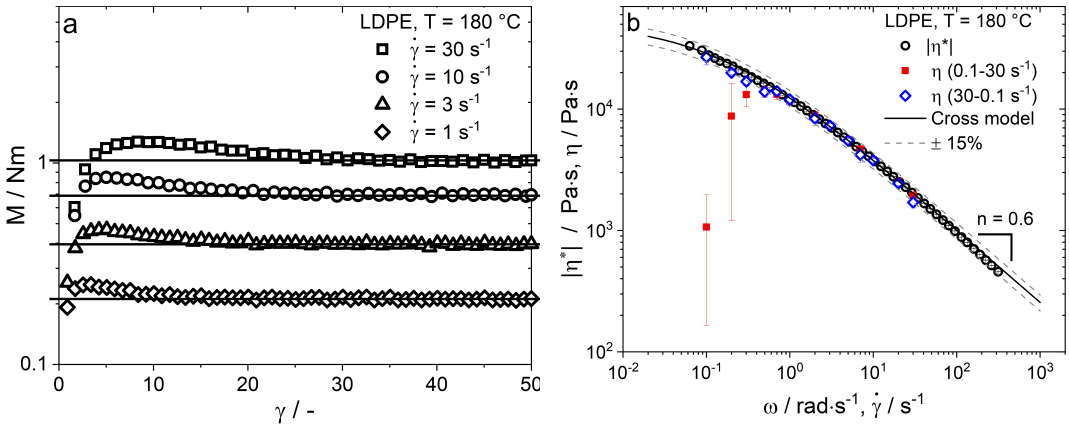

Figure 4.5: (a) Torque M as a function of strain γ for LDPE at the shear rate of 1, 3, 10, and 30 s^{-1} and (b) the complex viscosity $|\eta^*|$ as a function of angular frequency ω obtained by oscillatory shear frequency sweep experiments with rotational CCR and the shear viscosity η as a function of shear rate $\dot{\gamma}$ obtained by rotational CCR.

The shear viscosity η calculated by equation 4.1 for the simulation data with the free-slip boundary condition at the sealing resulted in an overestimation of the shear viscosity of 5.9%. These findings can be attributed to the increased shear rate and correspondingly increased shear stress at the edges of the upper cone. In conclusion, the simulations with the different boundary conditions show that the error in the calculation of the shear viscosity with equation 4.1 should not exceed 12.2% due to instabilities caused by the sealing. Slippage effects at the rotating cone were not investigated in the simulation, but it can be assumed that these influence the accuracy of the results to a greater extent than slippage at the sealing.

4.4.3 Steady-state shear viscosity obtained by a CCR

The shear viscosity η for the LDPE at a temperature of 180 °C was obtained by experimental measurements with the CCR. By setting up different deflection times, different shear rates could be measured. In figure 4.5 a, the torque measured at the upper cone during one full deflection of 50 is shown for the shear rates of 1,3,10, and 30 s^{-1}. For all four shear rates, an increase in torque can be observed at the beginning (below 15), leading to an overshoot before finally reaching a steady state. The overshoot is often observed in polymer melts and is attributed to the alignment of the polymer chains (Snijkers et al., 2013b). To determine the value of the plateau, the mean value of the torque in the range between 30 and 50 is calculated. To check whether this approach is legitimate, the mean value of the torque is determined for a window of every $\Delta\gamma$ = 5 deflection. We define the steady state to have been reached when the average value does not deviate by more than 1% compared to the previous value. Accordingly, for the curves shown in figure 4.5 a, the steady-state condition is reached after deflections of 30 for 30 s^{-1}, 25 for 10 s^{-1}, = 20 for 3 s^{-1}, and 15 for 1 s^{-1}. These steady-state values were used to calculate the shear viscosity according to equation 4.1. Figure 4.5 b presents the shear viscosity η and the complex viscosity $|\eta^*|$

for the investigated LDPE at 180 °C obtained by the CCR. In addition, the Cross model obtained by fitting the complex viscosity in figure 4.3 a is also depicted. To be able to estimate the deviation of the shear viscosity from the complex viscosity, a 15% deviation was added to the Cross model. The data of the shear viscosity, measured from low shear rates to high shear rates, overlaps with the Cross model for shear rates higher 0.5 s^{-1} (red squares). The obtained data for shear rates of 0.1, 0.2, and 0.3 s^{-1} have deviations between 20 and 85% and are below the Cross model. For these data, a steady-state plateau could not be reached. Examples of using the measured torque for the triple determination at a shear rate of 0.3 s^{-1} are shown in the supplementary information. To calculate the shear viscosity for these shear rates, the mean value of the torque between a strain of 30 and 50 was determined, regardless of whether a steady state was reached. Using the reversed measurement routine from high to low shear rates, the data of the shear viscosity are within the 15% deviation of the Cross model (blue rhombus). Based on these measurement data, the validity of the Cox–Merz rule can be assumed within a 15% deviation for the investigated LDPE. The data thus confirm the results of the measurements from the capillary rheometer (figure 4.3 a) and extend the measured shear rate range by a decade toward low shear rates.

We therefore selected the measuring routine from high to low shear rates for further measurements. The reason why the measurement routine from low to high shear rates is error prone in the low shear rate range has not yet been clarified. A possible influence on the measurement could be the protective film used, which is inserted between the polymer and the measurement geometry.

4.4.4 Verification of the ramp test by the temperature dependence viscosity of the LLDPE and PBD

To further verify the ramp-test method, the lowest viscosity and highest viscosity polymers were tested at different temperatures. The ramp-test method was used to obtain the shear viscosity η of LLDPE and PBD at temperatures of 140, 160, and 180 °C and 50, 100, and 150 °C, respectively (figures 4.6 and 4.7). TTS of the complex viscosity and the shear viscosity was investigated. The horizontal a_T and vertical b_T shifting factors were obtained by constructing the master curve using the complex viscosity from SAOS measurements. The same shifting factors were then used to shift the shear viscosity data obtained by the ramp test (figures 4.8 and 4.9).

Figure 4.6 a–c presents the complex viscosity $|\eta^*|$ and the shear viscosity η of LLDPE at 140, 160, and 180 °C. At a temperature of 140 °C (figure 4.6 a), the shear viscosity data are below the complex viscosity for the applied shear rate range. Up to a shear rate of 10 s^{-1}, this deviation is within the 15% deviation of the found Cross model. At temperatures of 160 °C and 180 °C, the shear viscosity data are within the 15% deviation of the corresponding Cross model for the applied shear rate range. On closer inspection, a change in the slope of the shear viscosity up to a slope of 0.6 can be seen for shear rates above 10 s^{-1} for all temperatures. It is speculated that

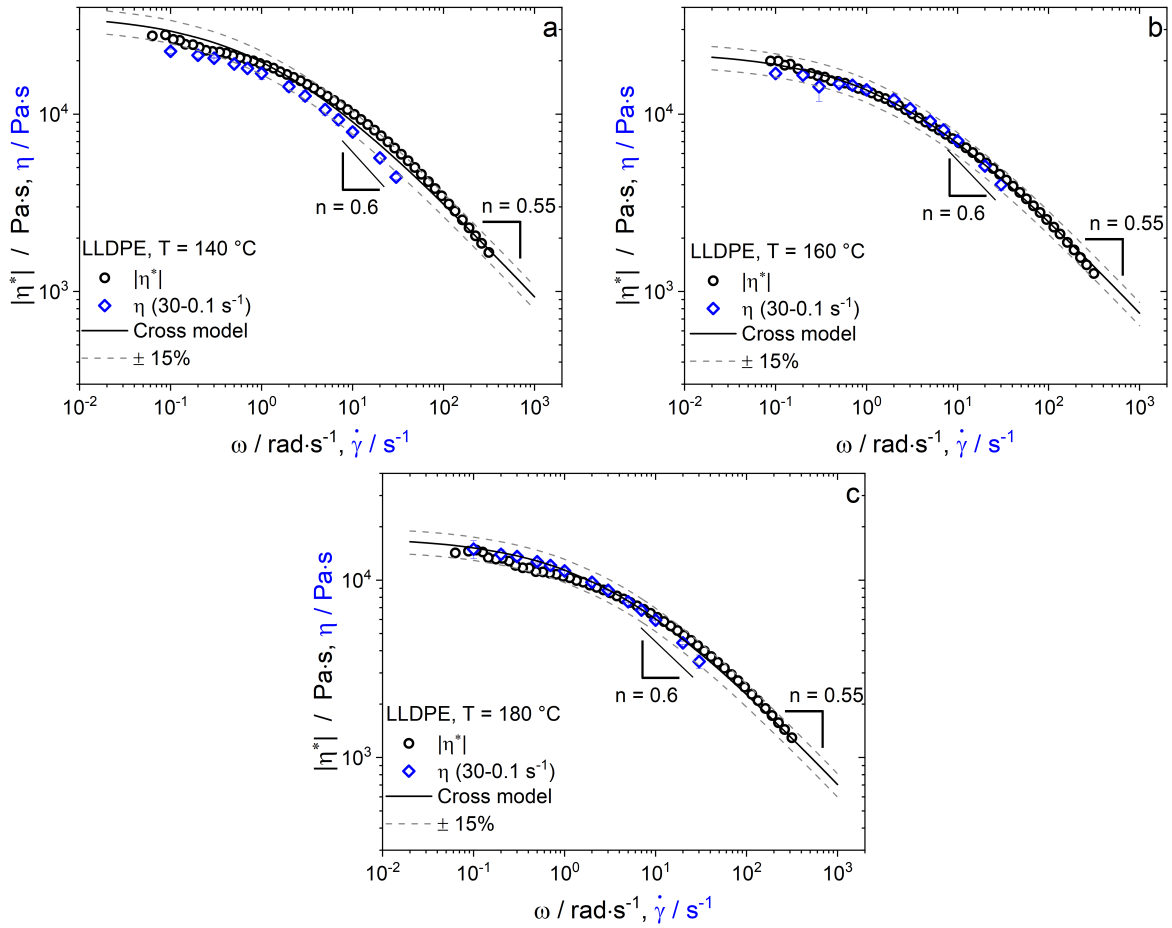

Figure 4.6: The complex viscosity $|\eta^*|$ as a function of angular frequency ω obtained by oscillatory shear frequency sweep experiments with rotational CCR and the shear viscosity η as a function of shear rate $\dot{\gamma}$ obtained by rotational CCR for LLDPE at (a) 140°C, (b) 160°C, and (c) 180°C

this change in slope can be linked to wall slippage, whether we use grooved plates. Heyer et al. have presented similar observations for slippage speculations of high elastic materials with a CCR and grooved plates (Heyer et al., 2022).

For the LLDPE, it can be assumed that the Cox–Merz rule is applicable within a 15% deviation up to the investigated shear rate of 30 s^{-1}. These findings are consistent with the results obtained by the capillary rheometer (figure 4.3 b).

The complex viscosity $|\eta^*|$ and the shear viscosity η for PBD are shown in figure 4.7 a–c at 50, 100, and 150 °C. For all temperatures, the shear viscosity data are below the data of the complex viscosity. Apart from the data for the shear rate of 30 s^{-1} for all three temperatures, and the data for the shear rates of 0.1–0.3 s^{-1} for a temperature of 150 °C, the shear viscosity data are within the 15% deviation of the corresponding Cross model.

Starting at a shear rate of 2 s^{-1} for 50 °C, a shear rate of 5 s^{-1} for 100 °C, and a shear rate of 10 s^{-1} for 150 °C, a decrease in the slope of the shear viscosity up to a slope of 0.75–0.8 can be seen. Even if the data are within the defined 15% deviation, this change in slope indicates that wall slippage may occur, as reported for LLDPE previously.

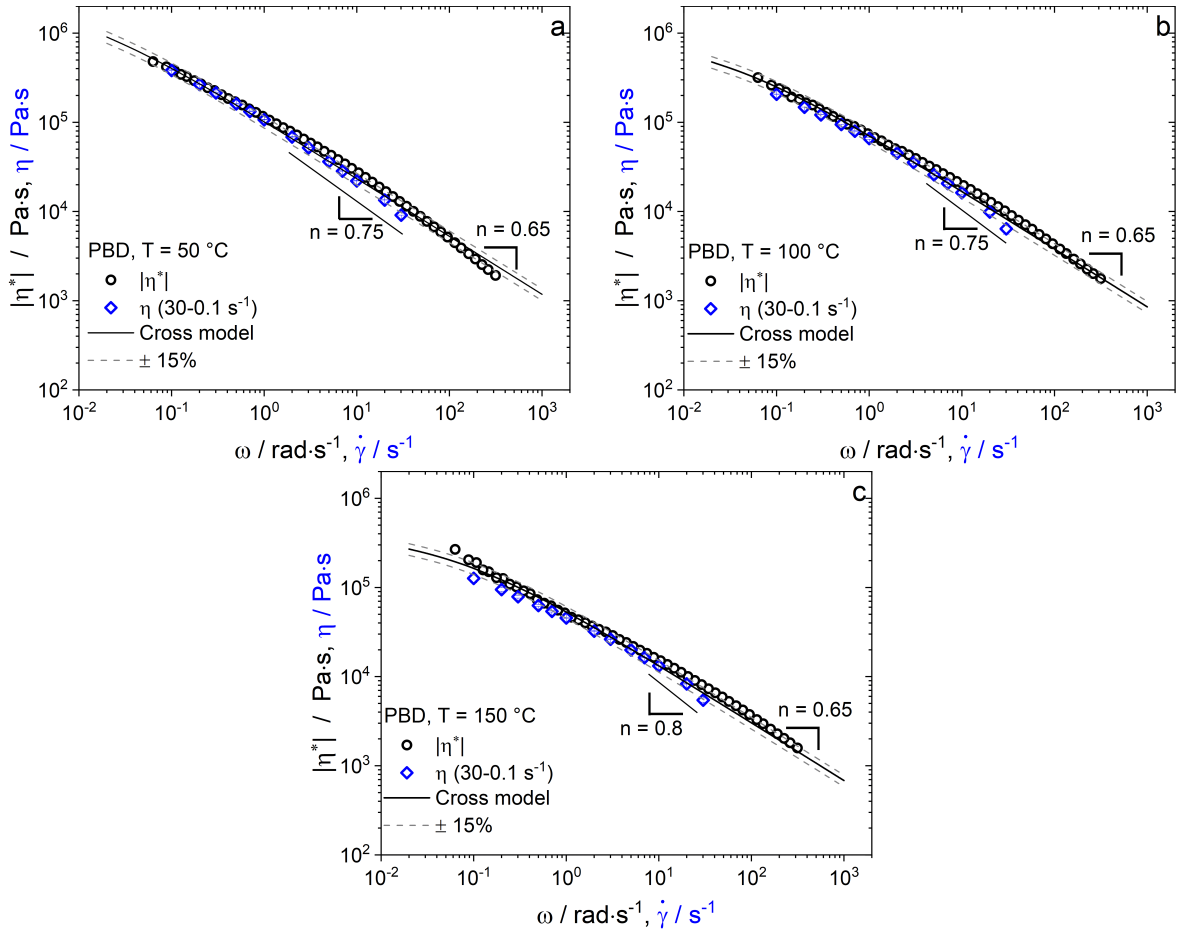

Figure 4.7: The complex viscosity $|\eta^*|$ as a function of angular frequency ω obtained by oscillatory shear frequency sweep experiments with rotational CCR and the shear viscosity η as a function of shear rate $\dot{\gamma}$ obtained by rotational CCR for PBD at (a) 50°C, (b) 100°C, and (c) 150°C.

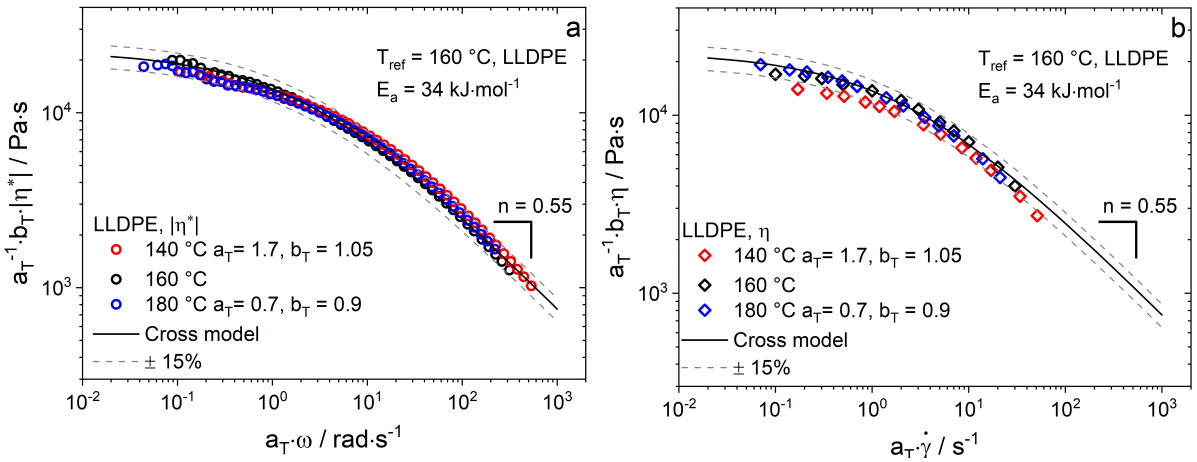

Figure 4.8: TTS of LLDPE based on results of figure 4.6 at a reference temperature of 160°C for (a) the complex viscosity $|\eta^*|$ and (b) the shear viscosity η.

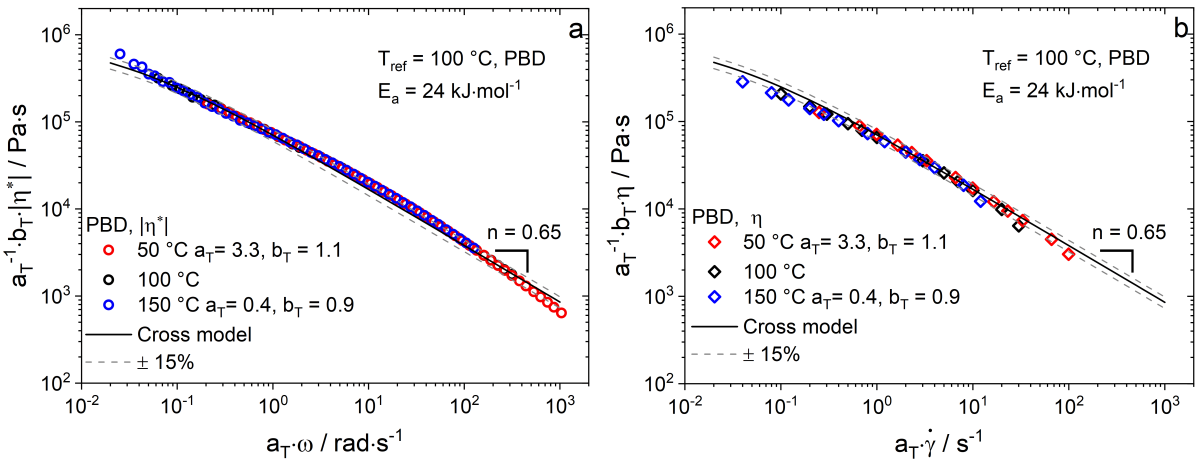

Figure 4.9: TTS of PBD based on results of figure 4.7 at a reference temperature of 100°C for (a) the complex viscosity $|\eta^*|$ and (b) the shear viscosity η.

The data measured at different temperatures were used to generate a master curve by a TTS. A detailed description of this method is given by Mavridis and Shroff (Mavridis and Shroff, 1992). As shown in figure 4.8 a, the complex viscosity $|\eta^*|$ for LLDPE at the different temperatures can be superimposed by shifting them vertically and horizontally, resulting in one master curve. Using an Arrhenius approach, the activation energy can be determined from the horizontal shifting factors $(a_T = (E_a R)(\frac{1}{T} - \frac{1}{T_{ref}}))$(Mavridis and Shroff, 1992). For LLDPE, an activation energy 34 $kJ \cdot mol^{-1}$ was found. This value is higher than values reported in the literature, e.g., $E_a \approx 29\ kJ \cdot mol^{-1}$ in the work of Stadler et al. (Stadler et al., 2007) and Keßner et al. (Keßner et al., 2009). However, an activation energy of $31 kJ \cdot mol^{-1}$ was reported for the same LLDPE in the previous work by Georgantopoulos et al. (Georgantopoulos et al., 2023). Therefore, it can be assumed that the deviation can be attributed to the instruments accuracy, the number of investigated temperatures, and different molecular characteristics (monomer and additives).

As the steady-state shear data should have the same temperature dependence as the SAOS data, the same horizontal a_T and vertical b_T shifting factors were used for the set of shear viscosity data (Markovitz, 1975). The resulting master curve for the shear viscosity η is shown in figure 4.8 b. The superposition of the data of the shear viscosity confirmed that the temperature dependence is equal for both viscosities measured.

Also for the PBD, the shifting factors found for the SAOS data, shown in figure 4.9 a, can be used to superimpose the shear viscosity η data, shown in figure 4.9 b. The activation energy found for PBD is 24 $kJ \cdot mol^{-1}$. By using the same horizontal a_T and vertical b_T shifting factors, it is also confirmed for PBD that the temperature dependence is equal for both viscosities measured.

The ability to find the same temperature dependence for two polymers for two different measurement routines shows that the ramp test method from CCR is capable of accurately determining the shear viscosity. In addition, the TTS can also be used to gather further evidence about the slippage behavior. As no wall slippage occurs in SAOS measurements, shifting factors are

found that are not influenced by slippage. If these are used to superimpose the shear viscosity, a deviation can be observed at high shear rates, indicating wall slippage.

4.5 Conclusion

Within this work, we applied and verified the so-called ramp test method, a method used with a CCR to obtain the shear viscosity η. By using LDPE, LLDPE, and PBD as model systems, it was shown that the CCR is capable to provide accurate and reliable data in a broad range of temperatures (50-180 °C) for low and high viscous materials (144-375$kg \cdot mol^{-1}$) over more than 2 decades in shear rate (30-0.1 s^{-1}). First, data of the complex viscosity $|\eta^*|$ obtained by CCR have been compared to shear viscosity data obtained by a capillary instrument. Thus, it was shown that the Cox–Merz rule is valid within a 15% deviation for the investigated samples. Subsequently, finite element methods simulations have been performed to investigate the influence of the CCR's sealing on the accuracy of the instrument. By numerical investigations, it was shown that the error due to the sealing cannot exceed 12.2%, and that is only at unlikely conditions of complete no slip at the sealing. Performing the ramp test, the validity of the Cox–Merz rule within a 15% deviation could be confirmed for the three investigated materials. By doing measurements at different temperatures for LLDPE and PBD, it was shown that the CCR is accurate enough to do TTS with SAOS data and with shear viscosity data. At high shear rates, a decreasing slope of the shear viscosity became apparent. We speculate that the decreasing slope indicates wall slippage, which has been reported recently (Heyer et al., 2022). Overall this study shows that CCR can measure shear viscosity at extrusion-like conditions in a defined manner and through a relatively easy measurement procedure. Beyond that, the ramp test could be used to obtain the shear viscosity η for solvent sensitive materials due to the closed cavity and the regulated pressure.

5 The Apparent Flow Behavior of a Soy Protein Isolate Dough

Chapter 5 is published as: F. Ellwanger, R. Kádár, and M. A. Emin Observations from capillary and closed cavity rheometry on the apparent flow behavior of a soy protein isolate dough used in meat analogues. *Applied Rheology 35(1): 20250036* (2025). doi: 10.1515/arh-2025-0059. Text, tables, figures and equations have been edited and reformatted for consistency.

Abstract

Twin-screw extrusion of plant proteins for meat analogue production has gained significant attention. However, understanding the underlying mechanisms remains challenging due to the complex flow behavior of protein doughs and limited measurement techniques. This study investigates the temperature-dependent flow behavior of a soy protein isolate dough 55 wt% under extrusion-relevant conditions. Apparent shear viscosity was measured between 95 °C and 140 °C using a capillary rheometer and, for the first time in protein doughs, by performing a ramp test in a closed cavity rheometer (CCR). The Bagley correction was applied, and the resulting correction factors were analyzed and discussed. Flow curves from both methods were fitted with a power-law model. The ramp test resulted in higher consistency indices (K = 3,412 – 32,237 $Pa \cdot s^n$) and lower flow behavior indices (n = 0 – 0.43) at all temperatures than the uncorrected data from the capillary rheometer (K = 708 – 13,013 $Pa \cdot s^n$, n = 0.1 – 0.48). Visual analysis of extruded strands and CCR samples revealed ongoing reactions, stick-slip-like surface patterns, and melt-fracture-like appearances in the extruded strands. In the CCR samples, bulk fracture was evident at 95 °C and 110 °C. At 125 °C, deformations of the sample were visible, which could be attributed to partial flow, limited relaxation, or rearrangements within the protein network. Both methods were affected by protein reactions and water evaporation at 140 °C, which partially falsified the measurements. Thus, this publication presents two methods for examining shear viscosity under extrusion-relevant conditions, demonstrating their potential and challenges, and discusses how they contribute to understanding high moisture extrusion for meat analogue production.

5.1 Introduction

High moisture extrusion of plant proteins to produce meat analogues is considered a promising technology for providing alternatives to meat. The growing demand for sustainable and animal-free meat analogues is driving research in this area. While the products available on the market are satisfactory to a degree, many lack the textural variability that meat products offer. Flavor also remains a major challenge, especially when it comes to meeting consumer demand for less processed or locally available protein sources. Therefore, a more detailed understanding of the high moisture extrusion process is crucial to achieve improved control and targeted enhancements, both in the technology and the products. A recent review summarizing the current understanding of the mechanism of formation of fiber-like structures and related hypotheses can be found in the work of van der Sman and van der Goot (van der Sman and van der Goot, 2023).

During the production of meat analogues via high moisture extrusion, protein-rich powder formulations are mixed with water, and the resulting protein dough is subjected to thermomechanical treatment in the screw section, before being pushed through a cooling die, where the protein dough is structured and cooled. Protein doughs used for manufacturing meat analogues can be viewed as biopolymer gels (McClements, 2024). Thus, depending on the milieu (temperature, pH, water content, shear rate, and others), these systems behave somewhere between solid and liquid-like. To complicate matters, the protein doughs are heterogeneous, leading to multiphase systems that include filled networks (lipid droplets, fibers, and others), phase-separated networks (different protein types, water-rich and water-pour phases), and co-gelled networks (McClements, 2024; Wittek et al., 2021d; Opaluwa et al., 2024; Wittek et al., 2021b; Saavedra I. et al., 2023; Wagner and Ganjyal, 2024). Consequently, the heterogeneity of the protein dough can be regarded as a multiphase system, composed of domains with varying degrees of compatibility, which ultimately influence the overall flow behavior. In general for gels, depending on the applied shear stress and temperature, bulk fracture can occur, leading to separated gel pieces that slide past each other (Skrzeszewska et al., 2010; Thornell et al., 2014). Van der Sman and van der Goot hypothesize that the protein dough, depending on the temperature and shear stress, can be described as a transient network in which intermolecular bonds can break and rearrange (van der Sman and van der Goot, 2023). Thus, understanding the structuring mechanisms of the protein doughs during high moisture extrusion remains challenging. Nevertheless, extensive experimental (Wittek et al., 2021d; Pietsch et al., 2017, 2019c; Kendler et al., 2021) and numerical (Wittek et al., 2021a; Ellwanger et al., 2023b; Kaunisto et al., 2024; Li et al., 2024) studies have significantly improved process-level understanding. However, despite these advances, the flow behavior of protein doughs under extrusion-relevant conditions (steady shear, 25 - 150 °C, 40 - 70 wt%, 5 - 40 bar) remains insufficiently characterized, which limits experimental control and predictive modeling.

While changes in the flow behavior can be influenced by complex biopolymer interactions, this study does not seek to resolve the underlying molecular mechanisms. IInstead, the focus is on evaluating and comparing rheological methods that are suitable for measuring shear viscosity

under extrusion-relevant conditions, in order to assess the flow behavior within an extruder. A soy protein isolate dough was used as the model protein system, as it is assumed to behave as a physical gel (Ellwanger et al., 2024) (no covalent bonds formed) with a transient network structure as described by van der Sman and van der Goot (van der Sman and van der Goot, 2023). As it is unclear how the transient network responds to steady shear, the terms apparent shear viscosity and apparent flow behavior are used throughout this study.

In general, conventional rotational rheometers are not particularly suitable for investigating protein doughs under extrusion-relevant conditions, as the required torque is often insufficient to quantify these highly viscous systems at relevant shear rates. Additionally, issues such as water loss, pressure effects, wall slippage, edge fracture, and sample loss may complicate the measurements. Nevertheless, such rheometers are used to obtain information about doughs for meat analogues. for example, they can be used to measure at lower temperatures (Tsegaye et al., 2025), to measure at higher water contents and then extrapolate to relevant extrusion conditions (van der Sman et al., 2024), or to measure by using pressure cells (Sägesser et al., 2025).

Closed cavity rheometers (CCR), also known as rubber process analyzers (RPA), are made for such challenging measurements. They are designed with a sealed, pressurized measuring chamber (preventing water evaporation, edge fracture and sample loss), grooved geometries (preventing slippage), and a motor capable of providing high torque. This enables the measurement of protein doughs closer to extrusion-like conditions, which is why the instrument is widely used by researchers in the field of meat analogues (Emin et al., 2017; Wittek et al., 2020; Schreuders et al., 2021a; Opaluwa et al., 2024). However, due to inherent construction limitations, the maximum strain of many of these instruments is restricted to a single rotation, and thereby precluding the performance of steady-rotational tests. Furthermore, the potential impact of the grooves on a steady flow is not accounted for in their theoretical framework. Recently, researchers have demonstrated that a start-up shear test of CCRs up to one rotation (referred to as ramp test) is sufficient to achieve a steady-state for the flow of polyolefin polymers and rubber compounds, thereby enabling the reliable acquisition of data for shear viscosity (Ellwanger et al., 2023a; Buhrin and Rauschmann T., 2021; Buhrin et al., 2021; Kleinschmidt et al., 2023).

In addition to rotational rheometers, capillary rheometers provide the capability to assess shear viscosity under conditions relevant to extrusion. Such rheometers may be attached inline to the extruder or used as offline instruments. To obtain true shear viscosity data, corrections for entrance effects (Bagley, 1957), non-Newtonian flow profiles (Rabinowitsch, 1929), and wall slippage (Mooney, 1931) must be made. An additional challenge is that the temperature control is less precise and slower than in rotational rheometers, which makes it more difficult to examine reactive protein doughs accurately.

Soy protein isolate is commonly used to produce meat analogues. Compared to other protein sources, such as wheat gluten, SPI is expected to have a lower reactivity (Ellwanger et al., 2024). Depending on the processing conditions, it may even appear as if time-temperature effects on the properties of SPI may appear negligible (Wittek et al., 2021d). However, at temperatures of 140 °C, it has been demonstrated that the time-temperature history influences SPI doughs,

potentially due to thermal degradation (Hayashi et al., 1992).As the measurement of the apparent flow behavior is challenging, only limited data on shear viscosity are available in the literature. In addition, protein isolates and concentrates from different manufacturers (Wittek et al., 2021c), and even different batches from the same manufacturer, can vary in composition and functionality, further complicating the comparability of rheological data. In the early 1990s, Fujio et al., and Hayashi et al. used a customized capillary rheometer to investigate soy protein isolate doughs with water contents between 17 and 70 wt% at a temperature of 140 °C (Hayashi et al., 1991; Fujio et al., 1991; Hayashi et al., 1993). The data may be described with the Herschel-Bulkley model, and it was found that with decreasing water content, the yield stress, the consistency coefficient and the flow behavior index decrease. The visual appearance of the samples is not provided in this study, meaning that no conclusions can be drawn regarding flow instabilities and wall slip phenomena, which can be of significant importance and represent a research gap.

In this study, we investigate the apparent flow behavior, with a specific focus on the apparent shear viscosity of a soy protein isolate dough containing 55 wt% water at temperatures ranging from 95 °C to 140 °C. We compare data obtained from a conventional capillary rheometer and the ramp test, applied for the first time to protein doughs, using a closed cavity rheometer. Additionally, samples collected during rheological measurements are visualized for the first time to identify potential volume instabilities. Observed flow irregularities are examined and discussed, with speculative insights into their possible relevance for structure formation in meat analogues. This work aims to provide a methodological contribution by evaluating and contrasting rheological techniques suitable for extrusion-relevant conditions.

5.2 Materials and methods

5.2.1 Materials

Soy protein isolate (SPI) Supro ST from Solae LLC (St. Louis, Mo, USA) was used for this study. According to the manufacturer, the protein content of SPI was > 90 %, the fat content < 1 %, and the ash content < 5 %. The water content was determined gravimetrically and was 3 %.

5.2.2 Sample Preparation

In order to produce homogeneous protein doughs that are easy to handle (insertable, no air pockets) for the capillary rheometer and closed cavity rheometer, a twin screw extruder (Brabender TwinLab F 20/40, Duisburg, Germany) with an attached 13 mm diameter cylindrical die was used. An SPI dough with a gravimetrically determined water content of 55 wt% was produced at a set barrel temperature of 30 °C and a total mass flow of 4 kg/h. The extruded samples with an average length of 20 cm were vacuum-sealed and kept at −32 °C until further usage. To thaw the sample, the material was removed from the freezer and allowed to thaw in its sealed form at 20 °C room temperature.

5.2.3 Capillary rheometry

To investigate the apparent flow behavior, a Göttfert RG 20 capillary rheometer (Buchen, Germany) was used. The apparent shear viscosity η_{app} can be calculated from the pressure signal obtained for the set apparent shear rate $\dot{\gamma}_{app}$:

$$\eta_{app} = \frac{\sigma_{app}}{\dot{\gamma}_{app}}, with\ \sigma_{app} = \frac{\Delta p}{4\frac{L}{D}}\ and\ \dot{\gamma}_{app} = \frac{32Q}{\pi * D^3} \tag{5.1}$$

where σ_{app} is the apparent shear stress, Δp is the measured pressure, L and D the length and diameter of the used die, and Q the volumetric flow rate. To correct the pressure for possible entrance effects, the Bagley correction can be applied (Bagley, 1957). In order to use this correction, three capillary dies with the same diameter and different length/diameter ratios of 40/1, 20/1, and 10/1 were used. Drawing the so-called Bagley plot, a shear-rate dependent end pressure correction factor p_{end} can be found to further calculate the true wall shear stress σ_w according to equation (5.2):

$$\sigma_w = \frac{\Delta p - p_{end}}{4\frac{L}{D}} \tag{5.2}$$

Thus, the Bagley corrected apparent shear viscosity $\eta_{app,Bagley}$

$$\eta_{app,Bagley} = \frac{\sigma_w}{\dot{\gamma}_{app}} \tag{5.3}$$

The prepared doughs were inserted into the rheometers reservoir and compressed by the piston as fast as possible to a pressure of 5 bar to minimize potential water loss/drying effects. Subsequently, the sample was held 300 s at the investigation temperature (95 °C, 110 °C, 125 °C, and 140 °C), to ensure uniform material temperature. We note that all three temperature zones of the capillary rheometer were set at the same temperature. The doughs were extruded from apparent shear rates of 1000 s^{-1} to 10 s^{-1} in 11 steps with 120 s for 1000 s^{-1} and 60 s for the other shear rates. The pressure to calculate the shear stress was determined as last 15 s of each shear rate step. To investigate possible time-temperature effects, a measurement was performed with a 300 s preheating step, a 120 s and 1000 s^{-1} step, followed by a 480 s step at a constant shear rate of 150 s^{-1}. The time–temperature effect was investigated once using the 20/1 die, whereas all other measurements were performed in triplicate, and the deviation of the average value was calculated and is shown in the figures.

5.2.4 Ramp test in closed cavity rheometer

To perform the ramp test (in literature aswell known as step shear rate test (Stokes and Telford, 2004)) a Rubber Process Analyzer (RPA flex, TA Instruments, Inc., New Castle, DE, USA), also called closed cavity rheometer (CCR) was used. To obtain the apparent shear viscosity, the lower cone of the CCR deflects by a maximum of 5000 % (almost 1 rotation) at a constant rotational speed while the torque is measured at the upper cone. More information about the ramp test can be found in our previous publication, where the method was validated for polyolefin polymers (Ellwanger et al., 2023a). For each deflection and thus each individual shear rate, a new sample piece weighing approximately 5 grams was taken for measurement. After the dough was inserted into the rheometer, the measurement was started as fast as possible. Before the actual ramp starts, the dough is held for 90 s at the selected temperature (95 °C, 110 °C, 125 °C, and 140 °C) in the basic position to ensure uniform material temperature.
All measurements were performed in triplicate, and the deviation of the average value was calculated and is shown in the figures.

5.2.5 Sample optical visualization

To visualize the surface of the extrudate strands and the samples from the CCR, a visualization system consisting of a Canon EOS 90D DSLR camera (Tokyo, Japan) equipped with a Canon L-series 100 mm macro lens and an LED (Kaiser slimlite plano 5000 K, Buchen, Germany) was used. Before visualization, the extrudates and CCR samples were air dried at room temperature.

5.3 Results

5.3.1 Capillary rheometry measurements

The effect of time-temperature history in the capillary rheometer reservoir on the stability of SPI doughs is shown in figure 5.1, where measured pressure is plotted against time at different temperatures under constant shear rate in isothermal conditions. The pressure fluctuates at 95 °C, 110 °C, 125 °C, and 140 °C, but the fluctuation decreases as the temperature increases. The pressure at 95 °C falls between that at 110 °C and 125 °C. At 140 °C, the pressure decreases with increasing time.

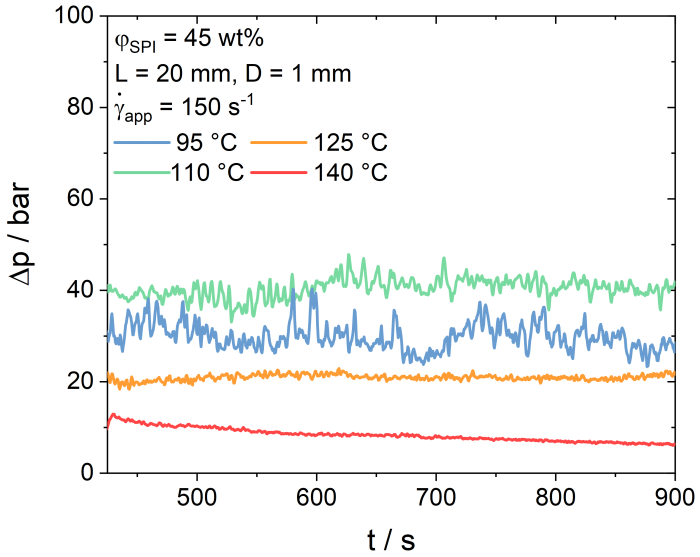

Figure 5.1: Measured pressure at constant apparent shear rate of 150 s^{-1} for t = 480 s at temperatures of 95 °C, 110 °C, 125 °C, and 140 °C as function of time.

Figure 5.2 shows the apparent viscosity for different dies at various temperatures. At all temperatures, shear thinning behavior is found and the apparent shear viscosity increases as die length decreases. The apparent shear viscosity values at a temperature of 95 °C are within the same range as at a temperature of 110 °C (also see figure 5.9a). With further increasing temperature, the apparent shear viscosity decreases. After applying the Bagley correction (Bagley, 1957) (figure 5.3), the Bagley-corrected apparent shear viscosities for each temperature largely overlap, however, there are a few exceptions. The shear thinning behavior is observed at all temperatures; however, at 140 °C, it only occurs between 250 s^{-1} and 1000 s^{-1}, while at lower shear rates, it appears as a plateau.

The found (Bagley) pressure correction factors are plotted in figure 5.4 over apparent shear rates for different temperatures. At 95 °C, the factor remains constant at approximately 17 bar across all apparent shear rates. At 110 °C, it stays constant at around 27 bar up to 100 s^{-1}, then rises

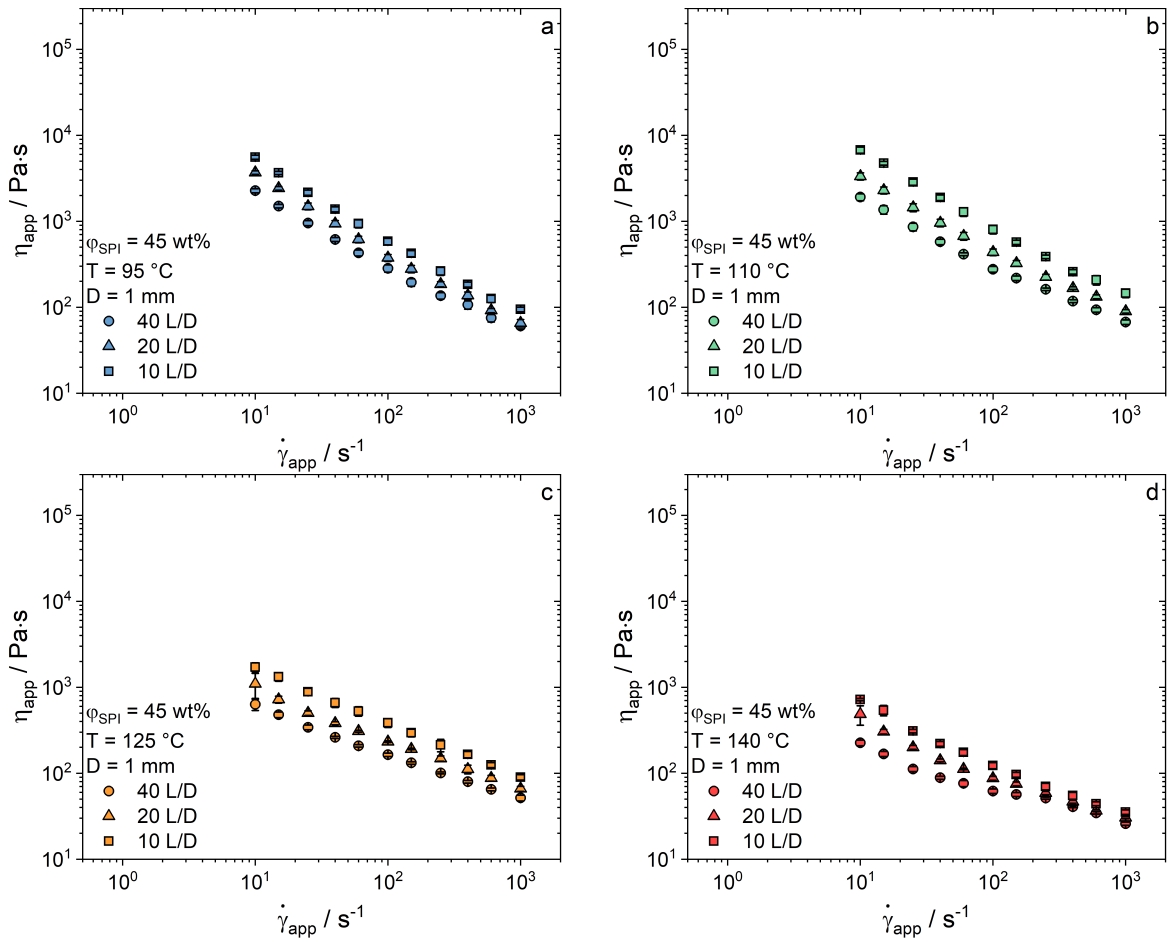

Figure 5.2: Apparent shear viscosity plotted over apparent shear rate for dies with the same diameter and different length for a temperature of 95 °C (a), 110 °C (b), 125 °C (c), and 140 °C (d).

to 39 bar. At 125 °C, it rises across the entire apparent shear rate range, increasing from 6 bar to 20 bar, while at 140 °C, it remains constant at 3 bar, except for a slight increase at 1000 s^{-1}.

Samples were taken during the capillary rheometer measurements to visually examine whether flow instabilities or wall slip phenomena could be observed. Figure 5.5 shows the capillary extruded strands produced at different temperatures and subsequently air-dried. For temperatures of 95 °C, 110 °C, and 125 °C across all shear rates, no smooth surfaces over the entire strand length are observed. Instead, the shapes are mainly random and discontinuous, appearing most similar to melt fracture or spurt in synthetic polymers (Koopmans et al., 2010; Georgantopoulos et al., 2021). At 125 °C, a stick-slip-like behavior is evident at apparent shear rates of 10 s^{-1} and 15 s^{-1}, as detailed in figure 5.6 for an apparent shear rate of 10 s^{-1} (Burghelea et al., 2010). At 140 °C, the strand is not smooth at higher apparent shear rates, but it appears partially smooth at a shear rate of 150 s^{-1}. At lower shear rates, bubble formation at the surface are clearly visible. A browning of the extruded strands with decreasing apparent shear rate (and increasing residence time in the reservoir) at 140 °C is also observed.

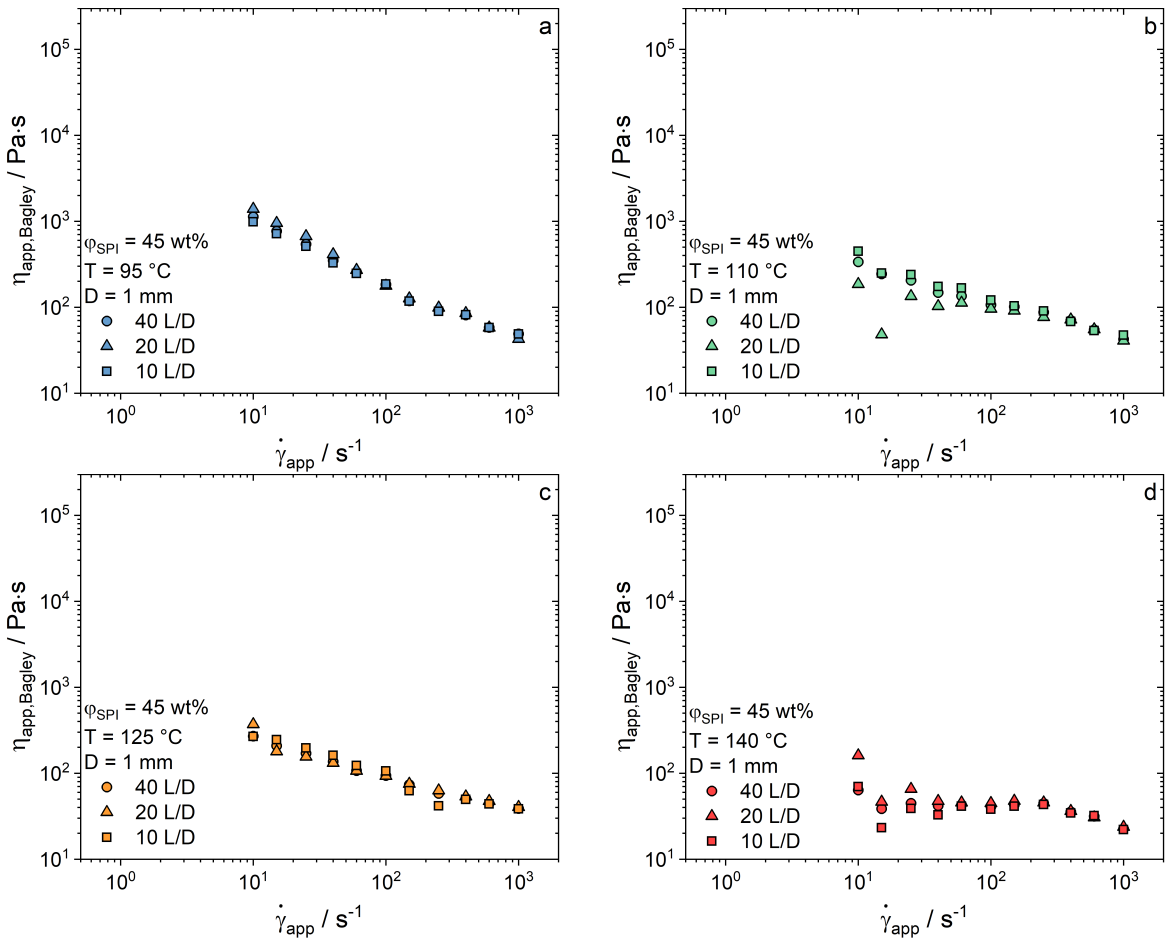

Figure 5.3: Bagley-corrected apparent shear viscosity plotted over apparent shear rate for dies with the same diameter and different length for a temperature of 95 °C (a), 110 °C (b), 125 °C (c), and 140 °C (d).

5.3.2 Ramp test method

The apparent shear viscosity measured during a full rotation with the closed cavity rheometer (CCR) is shown in figure 5.7 for different apparent shear rates at all temperatures. The apparent shear viscosity increases up to an overshoot, which can be seen as yielding point of a fluid, after which it decreases toward a lower "post-yield" value (Skadsem et al., 2019; Mujumdar et al., 2002). The overshoot slightly shifts towards higher strains with increasing shear rate and temperature.

At all temperatures, shear-thinning behavior is evident, except for the measurement at 140 °C and 1 s^{-1}. At 95 °C and 110 °C, the apparent shear viscosity tends to stabilize to an almost steady value in the post-yield area. As already observed in the capillary rheometer measurements, the apparent shear viscosity values at 95 °C and 110 °C are within the same range (also see figure 5.9c). At 125 °C, the apparent shear viscosity decreases compared to lower temperatures and reaches a steady state, though it oscillates around this value. Similarly, at 140 °C, apparent shear viscosity decreases further, with oscillations still present, while showing a slight

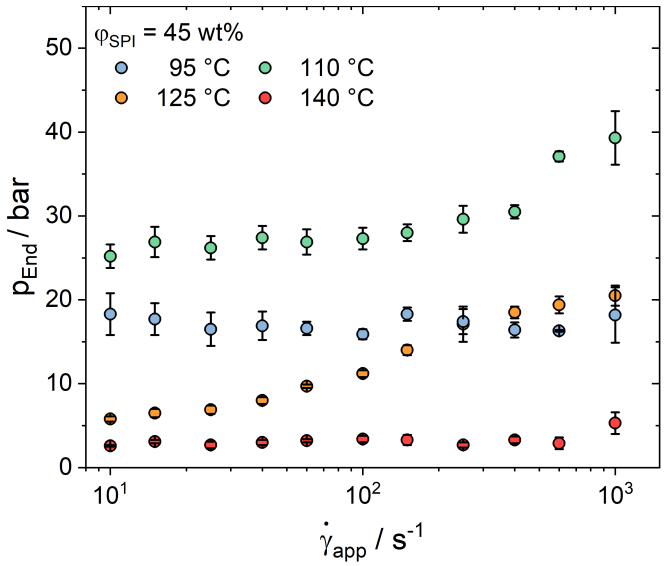

Figure 5.4: Pressure (Bagley) correction factor plotted over apparent shear rate for temperatures of 95 °C, 110 °C, 125 °C, and 140 °C as function of time.

decline with increasing strain. Comparing the number of oscillations to the number of grooves in the cone of the CCR reveals a match.

The visualization of the CCR samples after performing the ramp tests is shown in figure 5.8. The bottom view displays the closed cavity rheometers rotating cone while the top view reveals the surface of the closed cavity rheometers fixed cone.

At 95 °C the bottom view reveals bulk fracture. It looks like fracture is happening near the grooves, causing some gel pieces to remain stuck in the instrument and therefore not being visualized. The top view of the samples reflects the grooved surface of the fixed cone.

Irregular, deformed samples are presented at 110 °C. The bottom view shows that the gel that was previously in the grooves appears to have detached from the surrounding sample matrix, but no gel pieces have adhered to the grooves of the instrument. The top view shows that the gel that was in the grooves still adheres to the sample but is partially deformed.

At 125 °C it does not appear as if bulk fracture was happening, but the samples are deformed. At apparent shear rates of 50 s^{-1}, 25 s^{-1} and 10 s^{-1}, the material that was in the grooves is deformed. At apparent shear rates of 5 s^{-1}, 2.5 s^{-1} and 1 s^{-1}, the view from below shows that the material in the grooves has been pressed flat.

At 140 °C, the shape of the sample reflects the intact shape of the grooved measuring geometry, but holes and bubbles due to water expansion are visible on the surface.

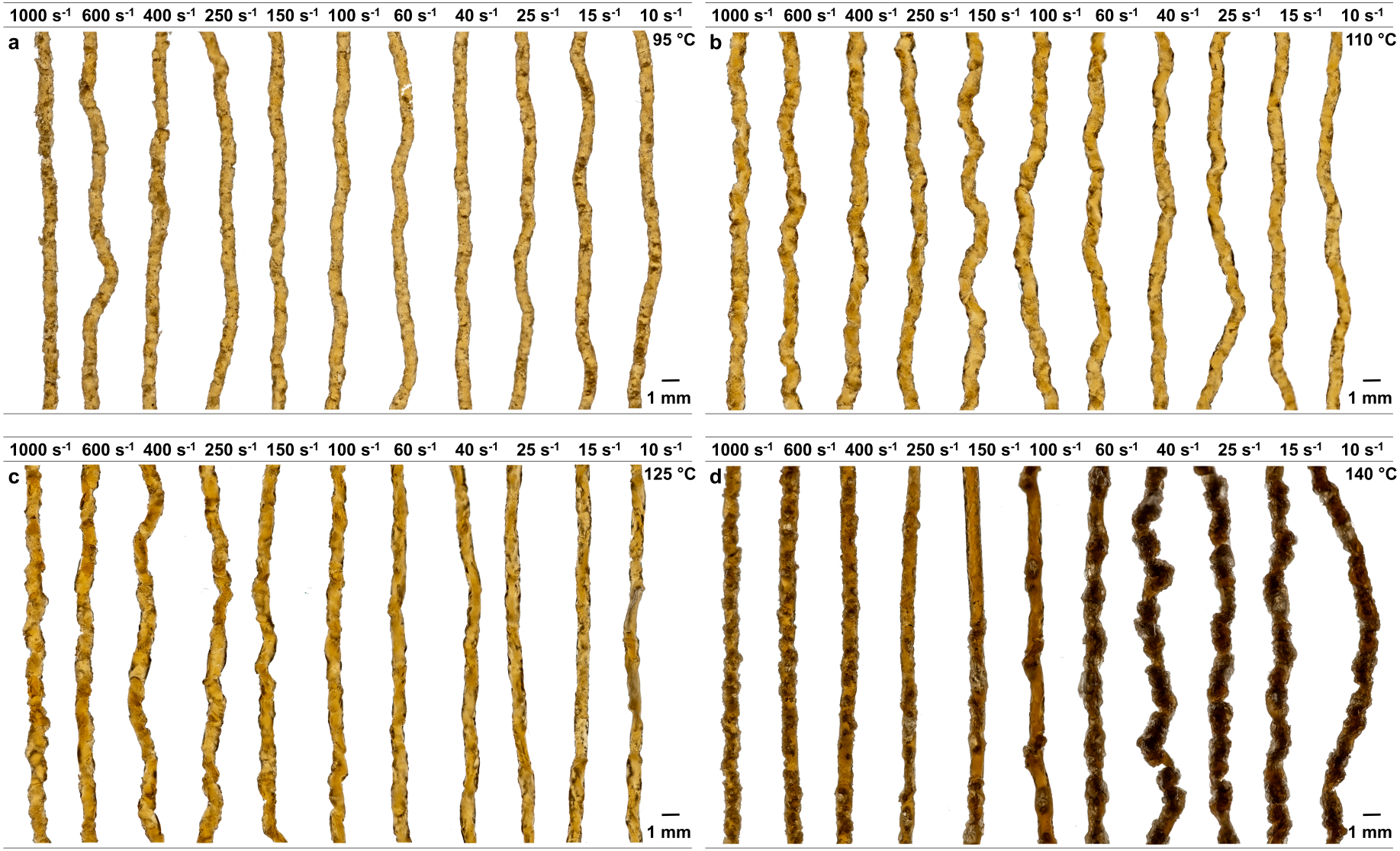

Figure 5.5: Offline visualization of the extrudate strands extruded at different apparent shear rates using the L = 40 mm, D = 1 mm die at a temperature of 95 °C (a), 110 °C (b), 125 °C (c), and 140 °C (d).

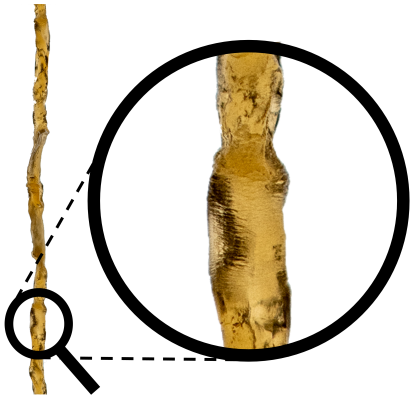

Figure 5.6: Offline visualization of the possible stick-slip effect at an apparent shear rate of $10\,s^{-1}$ at a temperature of 125 °C.

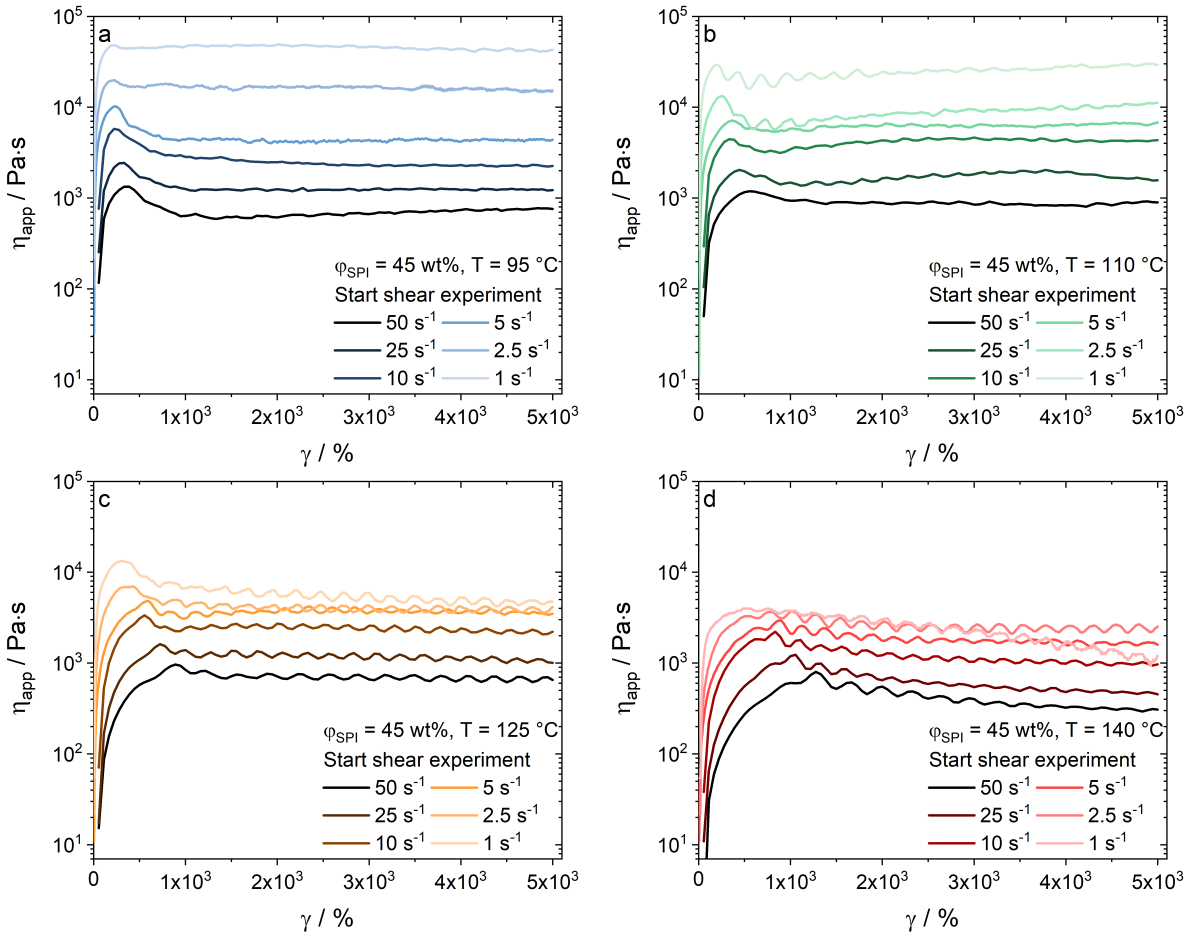

Figure 5.7: Apparent shear viscosity plotted over strain while performing the ramp test (start shear experiment) with a closed cavity rheometer at a temperature of 95 °C (a), 110 °C (b), 125 °C (c), and 140 °C (d).

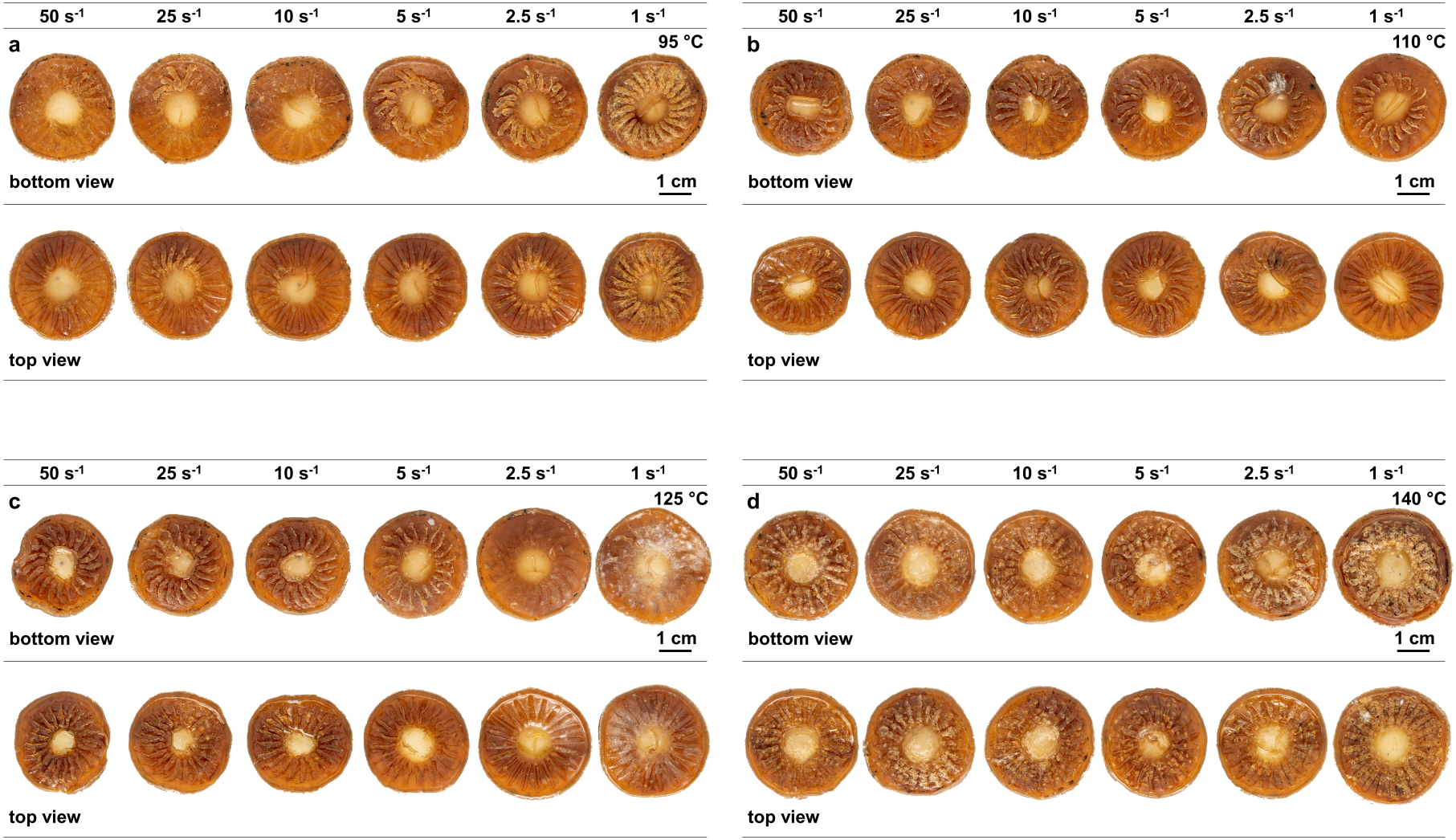

Figure 5.8: Offline visualization of the CCR pellets at different apparent shear rates using the ramp test at a temperature of of 95 °C (a), 110 °C (b), 125 °C (c), and 140 °C (d).

5.4 Discussion

To further compare and discuss the differences in shear viscosity measurements, the results from the different techniques were compiled and plotted in figure 5.9. The measured shear viscosity data at various temperatures were fitted using a Power-Law model, and the corresponding fitting parameters, including the consistency index and flow behavior index, are provided in Table 5.1. However, these flow curves and fits should be interpreted with caution, as the previously presented results indicate significant influences of ongoing reactions, bulk fracture, and potential flow instabilities on the measurements.

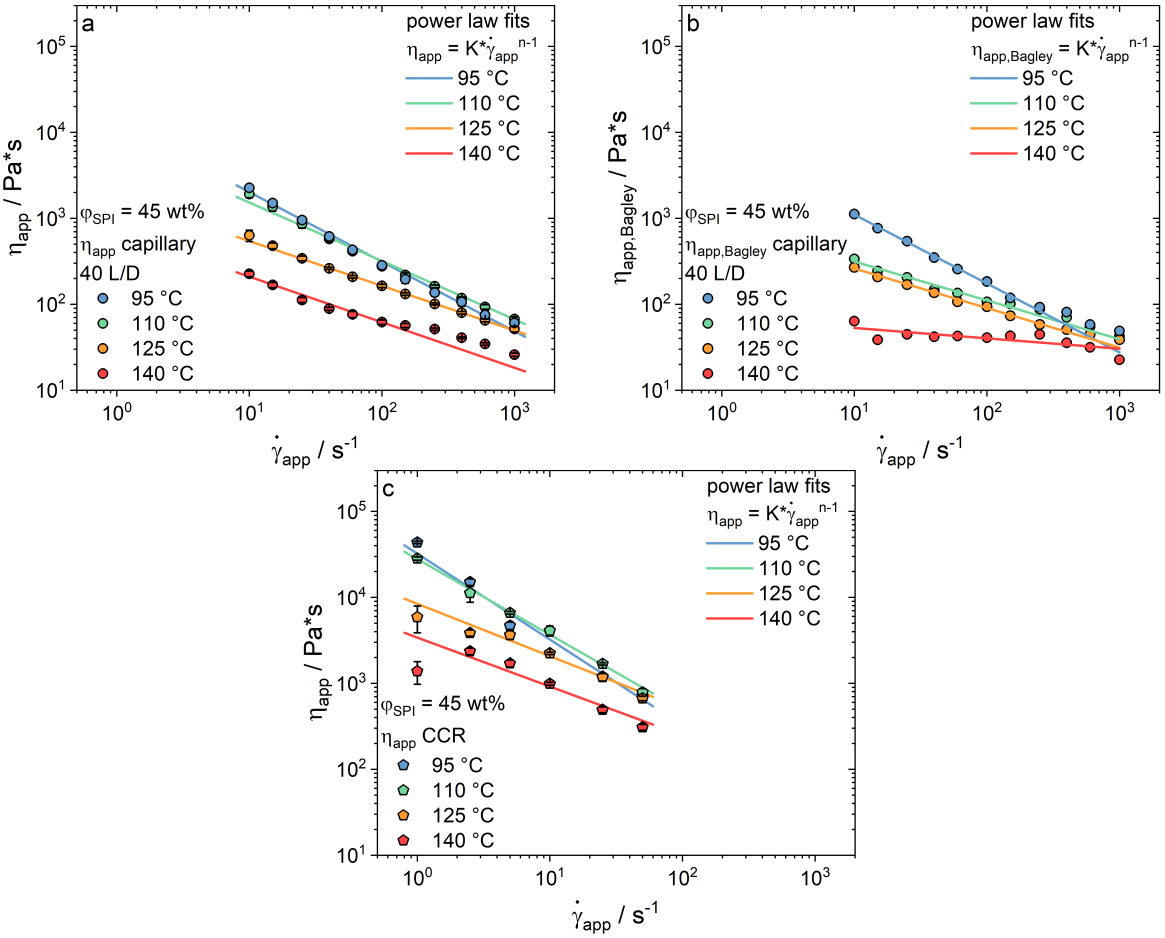

Figure 5.9: Comparison and power law fitting of the measured shear viscosities at different temperatures for (a) the apparent shear viscosity measured with the capillary, (b) the Bagley corrected apparent shear viscosity measured with the capillary, and (c) the apparent shear viscosity measured with the closed cavity.

5.4.1 Method-specific observations

Both rheometers confirmed shear-thinning behavior across the temperature range (95 °C to 140 °C); however, substantial differences in the resulting flow curves and fitted parameters were observed depending on the measurement technique.

Table 5.1: Consistency index K and flow behavior index n of the fitted shear viscosity data obtained with different methods at different temperatures.

$\eta_{app} = K * \dot{\gamma}_{app}^{n-1}$, $\eta_{app,Bagley} = K * \dot{\gamma}_{app}^{n-1}$

	95 °C			110 °C			125 °C			140 °C		
	K / $Pa \cdot s^n$	n / -	R^2	K / $Pa \cdot s^n$	n / -	R^2	K / $Pa \cdot s^n$	n / -	R^2	K / $Pa \cdot s^n$	n / -	R^2
Capillary												
η_{app}	13013	0.19	0.98	7303	0.32	0.98	1794	0.48	0.99	708	0.48	0.97
$\eta_{app,Bagley}$	6985	0.2	0.99	890	0.55	0.98	752	0.54	0.99	70	0.88	0.57
Closed Cavity Rheometer												
η_{app}	32237	0	0.88	27928	0.12	0.99	8441	0.39	0.95	3412	0.43	0.88

Capillary rheometry data indicated lower apparent shear viscosity values at higher temperatures but also exhibited strong signs of flow instabilities, including melt fracture and stick-slip patterns (figures 5.6 and 5.6). These instabilities complicate data interpretation and may arise from interactions between the protein matrix and capillary wall, potentially intensified by water evaporation or bulk fracture near the die entrance. Further, the Bagley correction (figure 5.4) revealed atypical behavior at 95 °C, 110 °C, and 140 °C. While the nearly constant correction factors at 140 °C may be attributed to proximity to the water vapor pressure, the trends at 95 °C (approximately constant correction factors) and 110 °C (approximately constant up to a shear rate of 100 s^{-1}) remain difficult to explain. It is particularly unclear why the apparent shear viscosity data before Bagley correction partly overlap at these two temperatures, while the Bagley correction factor at 110 °C is noticeably higher. One possible contributing factor could be temperature-dependent changes in network formation or intermolecular bonding, though this remains speculative and requires further investigation.

In contrast, the CCR method yielded higher apparent shear viscosity values and displayed a yield-like overshoot followed by shear viscosity decay, consistent with stress-induced bulk fracture. This overshoot could indicate a structural transition, possibly related to bond breakage in the protein network, as has been observed in other complex biopolymer systems (Mujumdar et al., 2002; Hicks and See, 2010). Notably, at 95 °C and 110 °C, bulk fracture was observed in CCR samples, as evidenced by detachment from the groove structures (figure 5.8). Once bulk fracture has occurred, it is conceivable that the lower cone will simply slip down the rest of the sample. This would result in a slipping measurement between the two surfaces rather than a measurement of stationary flow. At 125 °C and 140 °C, an oscillating torque signal was observed, the origin of which remains unclear. One possible explanation is that the material within the grooves does not fracture under stress; instead, the cone may slip over the sample surface. This would be consistent with the fact that the number of oscillations matches the number of grooves in the geometry.

The discrepancies between the capillary and CCR methods are not merely methodological artifacts but reflect the inherent challenges of measuring how SPI dough responds to thermomechanical stress. While capillary rheometry approximates extrusion flow more directly, it is prone to water evaporation, entrance effects, and flow instabilities, even when applying Bagley

corrections. CCR, on the other hand, offers better control over evaporation but is limited by its strain range and the potential for geometry-induced flow distortions.

5.4.2 Influence of temperature on flow behavior

Investigation of the influence of temperature on the stability of SPI doughs (figure 5.1) revealed that between 95 °C and 125 °C, the pressure signal remained relatively stable over time, with fluctuations decreasing as temperature increased. This reduction in fluctuations could also be related to changes in the transient network structure, which was suggested by the atypical trends seen in the Bagley correction factors. However, at 140 °C, a clear decrease in pressure over time was observed, indicating ongoing reactions. This reactions were also visually evident through the browning of the samples. These findings align with previously reported results, demonstrating that soy protein isolate remains stable up to 120 °C but becomes unstable at 140 °C (Wittek et al., 2021d; Hayashi et al., 1992).

The temperature dependence of material behavior became clearly evident in both measurement methods. At 95 °C and 110 °C, the transient protein network responded to shear stress more like a solid, as evidenced by the bulk fracture observed in the CCR measurements.

At 125 °C, transitional behavior was observed, with capillary data suggesting emerging wall slip and stick-slip effects. CCR measurements revealed that the material reaches a state where bond breaking and rearranging could play a crucial role, as evidenced by the deformed and flattened appearance of the samples, indicating partial flow but limited relaxation. This temperature range may represent a critical processing window for fine-tuning meat-like structure formation during extrusion.

Notably, signs of water expansion were only observed at a temperature of 140 °C, despite the expectation that expansion would occur at temperatures above 100 °C. This may be because the water is bound in the protein network and is therefore not freely available in the sample. The formation of bubbles and sample browning at 140 °C indicate chemical and physical transformations that likely alter the network structure and thus the flow behavior.

Interestingly, the flow behavior index at 125 °C and 140 °C changes only slightly between the apparent shear viscosities obtained by the capillary method without Bagley correction ($n = 0.48$ at 125 °C and 140 °C) and the CCR ramp test ($n = 0.39$ at 125 °C and $n = 0.43$ at 140 °C). Additionally, the relative decrease in the consistency index ($\frac{K(140°C)}{K(125°C)}$) is comparable for both methods (0.39 for capillary measurement, 0.4 for ramp test). This indicates that, despite their different limitations, both methods capture a similar temperature-dependent change in the material behavior between 125 °C and 140 °C.

5.4.3 Potential for meat analogues structuring

Flow instabilities such as intermittent slippage and bulk fracture were observed across both methods and temperature ranges. Notably, these instabilities occurred within the same temperature range (95 °C to 140 °C) in which the soy protein isolate used here has previously been shown to form fibrous structures at comparable moisture contents (Wittek et al., 2021a; Ellwanger et al., 2024). While these phenomena are typically regarded as undesirable artifacts in polymer processing, they may provide important insights into the mechanisms underlying fibrous structure formation during high moisture extrusion of meat analogues. The interplay between localized stress, shear deformation, and transient network structure (breaking and rearranging) could be a prerequisite for the development of anisotropic structures in meat analogues.

Moreover, Guan et al. recently proposed that flow instabilities, including sharkskin and melt fracture, may actually facilitate fiber formation (Guan et al., 2024). In our study, we observed sharkskin-like surface patterns in the capillary rheometer and signs of bulk fracture in the CCR, lending support to this hypothesis even though a different protein dough was used.

Finally, the overshoot observed in the CCR ramp test, which may be interpreted as the fracturing point of the protein network, could serve as a useful marker for the onset of structural transitions. It could potentially act as a fingerprint for predicting fibrous structure formation or be used for material screening.

5.4.4 Future directions

Future work should focus on understanding the presented artefacts and minimizing measurement inaccuracies by adapting rheological measurement techniques This could enable flow instabilities and bulk fracture to be linked more directly to structure formation mechanisms in meat analogues, and set these in correlation with the underlying biopolymer mechanics and the multiphase nature of the system. Particular attention should be given to identifying the relaxation dynamics and critical shear rates that determine whether the material undergoes bulk fracture. Additionally, understanding how thermomechanical history influences rheological behavior and protein conformation will be essential for optimizing processing conditions. Another key area is the identification of shear viscosity measures that are most relevant for experimental control, prediction of product characteristics, and improvement of predictive modeling.

5.5 Conclusion

This study examined the apparent flow behavior of soy protein isolate dough (55 wt% water) between 95 °C and 140 °C using a capillary rheometer and by performing a ramp test in a closed cavity rheometer (CCR). The two methods showed clear differences, mainly due to flow instabilities, and material-specific behavior like bulk fracture and protein reactions, which were not analyzed in detail. Visual inspection of the samples helped to interpret the measurement results. The capillary extrudates showed irregular surface patterns resembling melt fracture, stick-slip-like behavior at 125 °C and low shear rates (10 s^{-1} and 15 s^{-1}) and signs of browning reactions and water evaporation at 140 °C. Bagley correction factors showed atypical behavior at 95 °C, 110 °C and 140 °C, possibly linked to the transient network and vapor pressure, but yet could not be fully explained. In the CCR, bulk fracture occurred at 95 °C and 110 °C, while at 125 °C, deformed and flattened samples pointed to bond breaking and rearrangement in the protein network. While both rheological methods have limitations, they provide complementary insights into the apparent flow behavior of protein doughs under extrusion-relevant conditions. The capillary rheometer better mimics flow in the extrusion process, while the CCR ramp test may serve as a useful tool for material screening and potentially offer a fingerprinting approach for structuring protein doughs. Future work should aim to link these flow behaviors to structure formation and improve methods for predicting extrusion outcomes.

6 Method Application and General Discussion

chapter 6 includes unpublished data. The methods used to obtain the presented results can be found in chapter 2 (dough preparateion and extrusion process), 5 (ramp test in closed cavity rheometer), and 3 (simulation setup, evaluation of the collected simulation data)

6.1 Introduction

Twin-screw extrusion is the key technology for producing meat analogues. As outlined in the introduction, the formation of meat-like structures arises, among other things, from the interaction between the thermomechanical stresses generated in the screw section and the response of the material. Because plant proteins undergo both favorable and unfavorable transformations under these conditions, a mechanistic understanding of the underlying process–structure–function relationships remains essential yet incomplete.

This thesis contributes to closing this gap by developing and applying complementary experimental and numerical methods that resolve local processing conditions and the corresponding material behavior. First, model products were produced using the structure modulation method, which enables the systematic variation of product structures without changing the protein source or the overall processing parameters.

To access local process conditions in the screw section, a computational fluid dynamics model based on the Moving-Particle Semi-implicit (MPS) method was established. Unlike conventional continuum approaches, this particle-based method enables the simulation of a relevant screw-section length without assuming full filling. By implementing a literature-based rheological model and solving the energy equation, local quantities such as degree of fill, residence time distributions, shear rate distributions, and temperature profiles were obtained.

Because these local process conditions directly influence the flow behavior of protein doughs, a rheological method, the ramp test, was introduced to measure shear viscosities at extrusion-relevant temperatures. After validating the method using polyolefin model systems between 50 and 180 °C, it was applied to protein doughs and compared to conventional capillary rheometry to establish its suitability for plant protein extrusion processing.

The following general discussion critically evaluates the conventional control parameters that are recorded when using structural modulation methods. As outlined in the introduction, these variables alone cannot fully explain the structural changes observed during extrusion. Therefore, the additional investigation methods developed in this work, the ramp test and the MPS simulation, are used to deepen the mechanistic understanding of twin-screw extrusion and to interpret the experimental observations. The main findings of each method, their limitations, and implications for further research are discussed.

6.2 Method application

6.2.1 Structure modulation of high-moisture meat analogue

A successful chemical structure modulation was conducted in chapter 2. This was achieved by adding acids to adjust the pH of the formulation, thereby altering protein–protein interactions and thus modifying the resulting product structure. The extrusion processing conditions (screw speed, mass flow rate, barrel and die temperatures) were kept constant. The method was applied to soy protein isolate, which predominantly forms non-covalent networks, and to wheat gluten, whose network formation also involves covalent bonding. To illustrate why the conventional control parameters are insufficient for explaining the structural differences obtained through structure modulation, the recorded processing data for the SPI trials are presented and evaluated below.

Results

The control parameters commonly monitored during SPI extrusion were recorded for trials with water, 0.25 M and 0.5 M acetic acid (AC), 0,25 M and 0.5 M citric acid (CT). Figure 6.1 shows the motor torque (a), pressure before the cooling die (b), and material temperature before the cooling die (c). Decreasing pH generally increased torque, although the 0.5 M CT trial showed only a slight rise compared to the water reference. Torque fluctuations ranged from 7 and 16 %. In contrast, the pressure before the cooling die decreased with acid addition, accompanied by large fluctuations between 21 to 56 %. The material temperature changed only marginally, decreasing from 117 °C with water addition to 115 °C with decreased pH.

Discussion

The investigation presented in chapter 2 linked differences in product structure directly to variations in protein crosslinking density. This relationship was established through mechanical characterization of the final products and protein solubility analysis in selective buffer systems. While these analytical methods offer important insights into the resulting product properties, they remain offline measurements and therefore do not capture the material behavior under the actual thermomechanical conditions of extrusion. In addition, the complex viscosity of the corresponding protein doughs was measured at extrusion-relevant temperatures.

An increase in the complex viscosity with decreasing pH was observed for all soy protein isolate formulations processed acids (see figure 2.4). Based on the assumption that the Cox–Merz rule holds, as previously applied by Wittek et al. (2021a), higher torque demands and higher pressures during extrusion would be expected when the shear viscosity increases Akdogan (1996). As shown in Fig. 6.1a, a pH-dependent rise in torque was indeed observed. However, the 0.5 M CT trial, which exhibited the highest complex viscosity, did not follow this trend. Its torque value remained below those of the other acid trials and only slightly exceeded that of the water

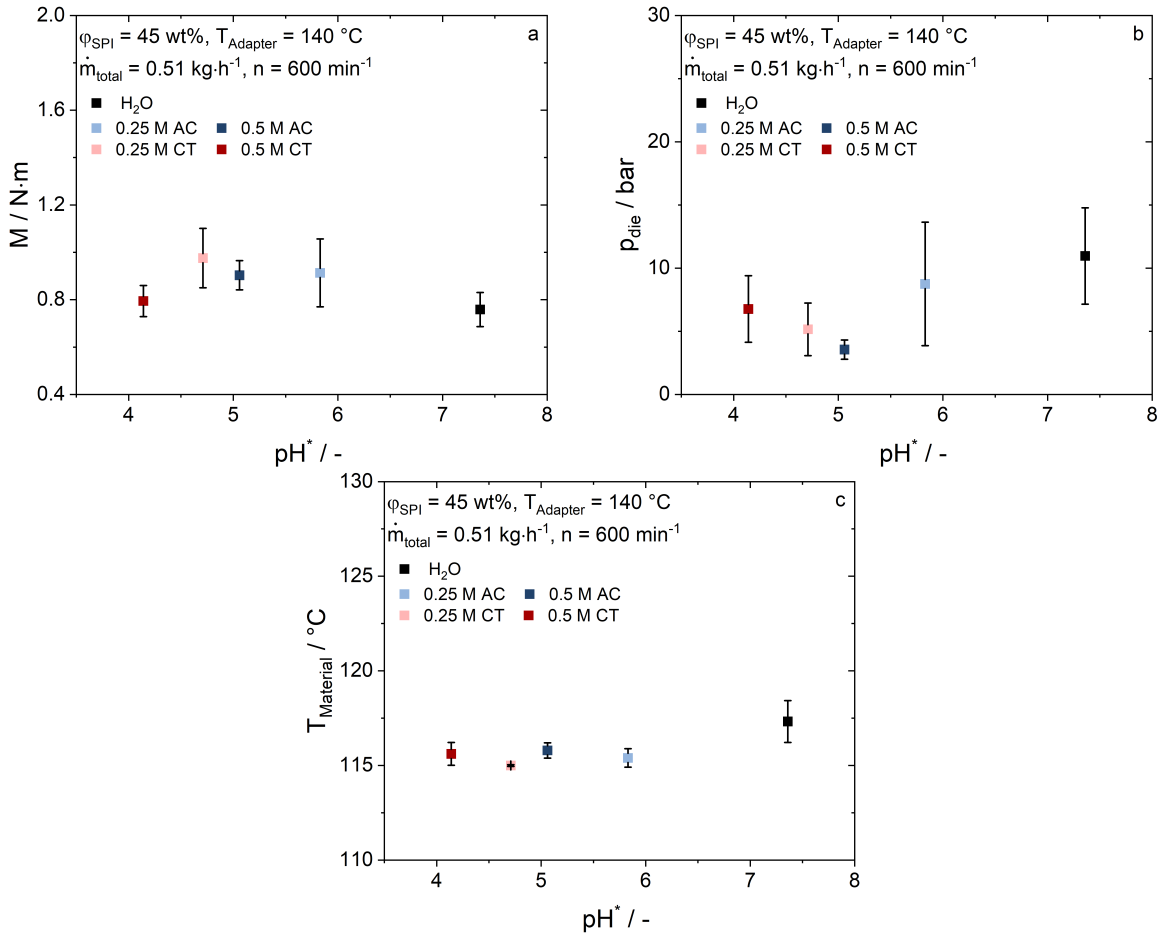

Figure 6.1: Integral process parameters measured while producing meat substitutes with pH modulation: (a) torque of the extrusion motor, (b) pressure in the die adapter, and (c) material temperature in the die adapter.*pH values taken from 2.

reference. There are several possible reasons for this deviation. Process-related reasons include changes in the flow field, such as the degree of fill or temperature. Material-related reasons include the inapplicability of the Cox–Merz rule to these protein systems and changes in water holding and syneresis, which could alter lubrication behavior within the screw section.

Pressure, which is commonly interpreted as an indirect indication of shear viscosity (Akdogan, 1999), also behaved unexpectedly. The addition of acids resulted in a decrease in die pressure, which would suggest a lower shear viscosity. As with torque, this observation may indicate that the complex viscosity measured in oscillatory shear does not straightforwardly translate to shear viscosity under extrusion conditions, or that the flow at the die entrance is influenced by additional factors such as wall slip or other flow instabilities. Temperature effects can be excluded as the primary cause for these discrepancies, as the measured material temperature in the die adapter remained nearly constant across all trials (figure 6.1c).

Taken together, these findings clearly demonstrate that the interpretation of conventional processing parameters alone is insufficient for explaining the structural differences exemplary induced through chemical structure modulation. To advance the mechanistic understanding of protein extrusion for meat analogue production, additional methods are required. Specifically,

methods capable of probing shear viscosity at extrusion-relevant temperatures and methods that can resolve local process conditions in the screw section. The ramp test and the MPS simulation method directly address these requirements and are therefore applied to deepen the mechanistic understanding and explain the observations presented above.

6.2.2 Investigation of apparent flow behavior

The ramp test method was first introduced and validated for polyolefin polymers in chapter 4 and later applied to soy protein isolate doughs in chapter 5. It was designed to quantify shear viscosity at temperatures representative of extrusion processing. Consequently, this method can be used to investigate the flow behavior of the pH-modified doughs and assess whether their response under steady shear differs from their behavior under oscillatory shear.

Results

Figure 6.2 shows the results of the ramp test performed at an apparent shear rate of $10\,s^{-1}$ and a temperature of 140 °C for the water-based and pH-modified doughs. The characteristic curve shape previously described in chapter 5 is observed for all doughs. The apparent shear viscosity first increases, then exhibits a pronounced overshoot, and finally decays towards a plateau. With decreasing pH, the overshoot shifts to higher apparent shear viscosities, occurs at lower strain values, and the plateau shear viscosity increases.

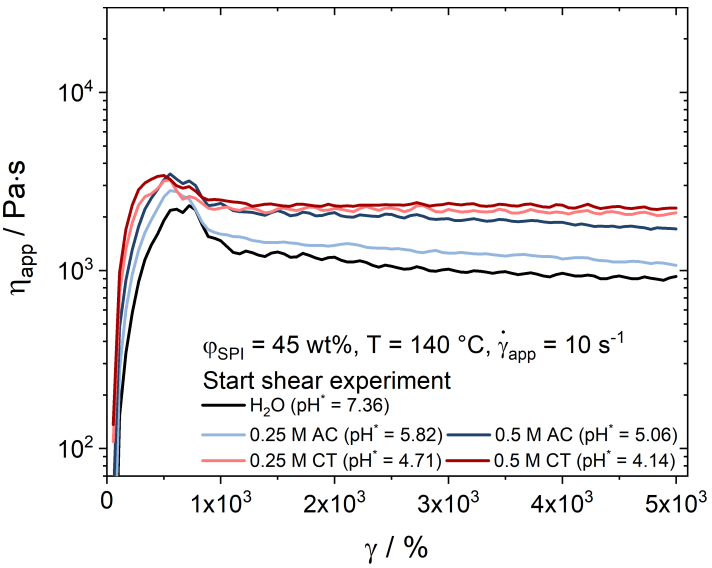

Figure 6.2: Apparent shear viscosity plotted over strain while performing the ramp test at a temperature of 140 °C, and at an apparent shear rate of $10\,s^{-1}$ for pH-shifted doughs. *pH values taken from chapter 2

Conducting the ramp test at various temperatures and apparent shear rates and assuming steady-state behavior at the end of each ramp yields apparent flow curves. These are shown in figure 6.3 for the water-based dough (a) and the dough prepared with 0.5 M CT (b). For both formulations, the apparent shear viscosity decreases with increasing temperature and shear rate. While the

overall temperature dependence is comparable across both doughs, the apparent shear viscosity of the 0.5 M CT dough is consistently higher. Interestingly, for both formulations, the curves at 95 °C and 110 °C partially overlap.

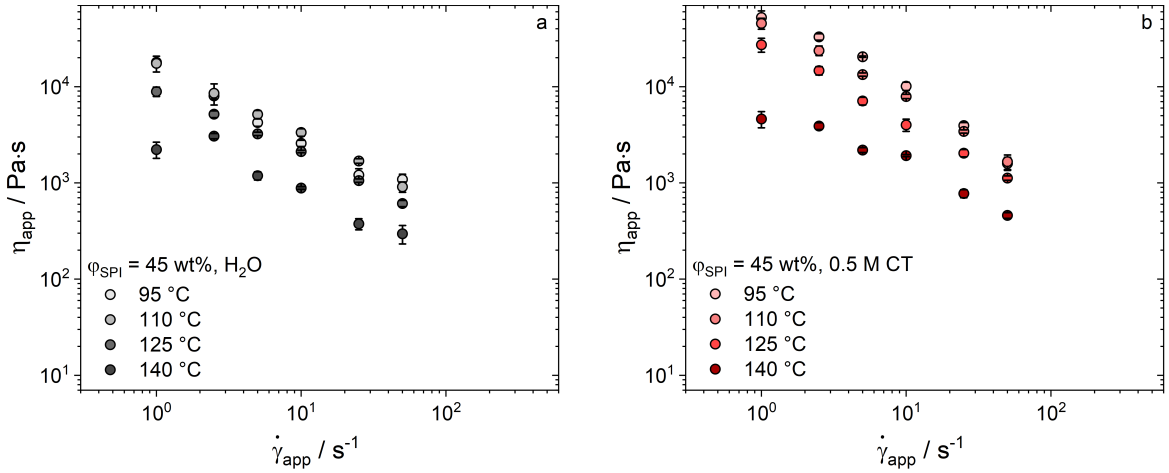

Figure 6.3: Apparent shear viscosity plotted over apparent shear rate at different temperatures for a dough prepared with (a) water, and (b) 0.5 M citric acid.

Because the strain at which the overshoot occurs depends on both temperature and apparent shear rate, the peak strain values were plotted against the corresponding apparent shear rates at different temperatures in figure 6.4. For the water-based dough, the peak strain increases with both temperature and apparent shear rate, with a more pronounced temperature effect at low apparent shear rates. In contrast, the dough containing 0.5 M CT shows no clear dependence on temperature. Below 10 s^{-1}, the peak strain increases with temperature, whereas above 10 s^{-1} it increases with decreasing temperature. Overall, the peak strain of the pH-modified dough is lower and the differences between conditions are less pronounced compared to the water dough.

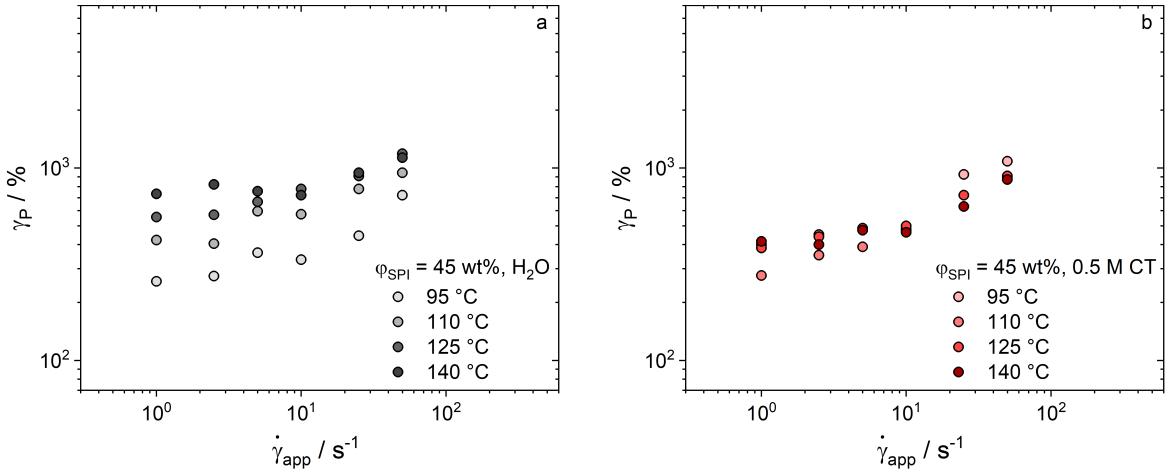

Figure 6.4: Strain at structural breakdown plotted over apparent shear rate while performing the ramp test at a different temperatures for a dough prepared with (a) water, and (b) 0.5 M citric acid.

Discussion

The results obtained for motor torque (figure 6.1a) and die pressure (figure 6.1b) could not be correlated with the complex viscosity data presented in chapter 2. The nearly constant material temperatures observed throughout the trials suggest that the total viscous energy dissipation in the extruder remained essentially unchanged. This indicates that the overall shear viscosity likely did not vary significantly. However, this does not rule out the possibility of local variations in viscosity or energy dissipation that the available measurements in this trials cannot resolve. Thus, the ramp test was introduced to determine the apparent shear viscosity under steady-shear conditions, as these conditions more closely resemble the deformation that occurs during extrusion.

However, as shown in figure 6.2, the apparent shear viscosity obtained from the ramp test exhibits the same qualitative dependence on pH as the complex viscosity data (figure 2.3). With decreasing pH, both the complex and the apparent shear viscosity increase. Furthermore, for the dough prepared with 0.5 M CT, which had the lowest pH and produced the poorest product structure, the temperature and shear-rate dependencies of the apparent shear viscosity (figure 6.3) is comparable to those of the water-based dough. Although the absolute apparent shear viscosities differ, the trends remain similar. Extrapolating these observations to the higher shear rates within the screw section reinforces the conclusion that the contradictory torque and pressure measurements cannot be explained by shear viscosity behavior.

A notable difference between the dough prepared with water and that prepared with 0.5 M CT emerges in the overshoot behavior (figure 6.4). The strain-at-peak, associated with the onset of structural breakdown (Mujumdar et al., 2002; Hicks and See, 2010), occurs at systematically lower strains and higher stresses in the pH-reduced dough. While this phenomenon does not resolve the inconsistencies observed in torque and pressure, it provides valuable information regarding the structural strength of the doughs and may relate to structure formation within the cooling die.

As discussed in chapter 2, decreasing pH leads to an increase in physical cross-link density in SPI systems, resulting in meat analogues that are more brittle and rigid. The ramp test data extend this interpretation to temperatures relevant for extrusion. Enhanced cross-linking increases the stress required for structural breakdown, reflected in higher apparent shear viscosities, but simultaneously reduces the strain the material can withstand before breakdown. The same qualitative relationship was observed upon decreasing temperature. Lower temperatures shift structural breakdown to lower strains and higher stresses. Considering that structure formation in SPI becomes more pronounced with increasing temperature (Wittek et al., 2021a), it may infer that greater elongational deformability prior to breakdown could facilitate protein alignment and structure formation within the cooling die. Consequently, the ramp test may serve as a rapid and effective tool for assessing the structural development potential of protein doughs under extrusion-relevant conditions.

6.2.3 Investigation of local processing conditions

To further clarify the contradictory observations in torque and pressure, it is necessary to investigate whether differences in the local flow field within the screw section could explain the processing behavior of the pH-modified doughs. Therefore, the MPS simulation approach was employed to access local processing conditions, such as degree of fill, shear-rate distribution, and local residence-time distributions, which cannot be measured experimentally. Simulations were carried out for a 7.75 L/D screw configuration equipped with a 1.75 L/D neutral kneading block. To reflect the effects of chemical structure modulation, the simulations used viscosity models derived from the ramp-test data of doughs prepared with water and 0.5 M CT (figure 6.3). Although flow instabilities were observed in chapter 5, the ramp test was considered the most suitable method for approximating extrusion-relevant flow behavior. As both doughs showed comparable temperature dependence, simulations were simplified by assuming an isothermal condition of 140 °C. The resulting apparent shear viscosities were fitted using the power-law model, and the corresponding consistency and flow-behavior indices are summarized in Table 6.1.

Table 6.1: Values of the power-law viscosity model ($\eta_{app} = K \cdot \dot{\gamma}_{app}^{n-1}$) describing the apparent shear rate dependency of the apparent shear viscosity measured with the ramp test for doughs prepared with water and 0.5 M CT.

	Variable	water	0.5 M CT	Unit
Consistency index	K	3,895	7,584	$Pa \cdot s^n$
flow behavior index	n	0.35	0.35	-

Results

Figure 6.5 shows the results of the MPS simulations conducted with the two shear viscosity datasets. The left side illustrate the filling behavior, while the right side show the shear-rate distribution in the first kneading disc. At first glance, the simulation results appear nearly identical. A closer inspection, however, reveals that the simulation using the rheological data of the 0.5 M CT dough exhibits a slightly higher degree of fill in the kneading section. The visualization of the shear-rate field likewise shows only minimal differences.

To enable a quantitative comparison, the mean degree of filling and the mean shear rate were computed along the dimensionless screw length and are presented in figure 6.6. As shown, the degree of filling is marginally higher for the 0.5 M CT case in both the conveying section and the kneading block. The difference is less than 0.02 in the conveying elements and less than 0.14 in the kneading elements. No meaningful difference in the average shear rate can be identified between the two simulations. The values remain very similar, with approximately 350 s^{-1} in the conveying section and 250 s^{-1} in the kneading block for both shear viscosity datasets.

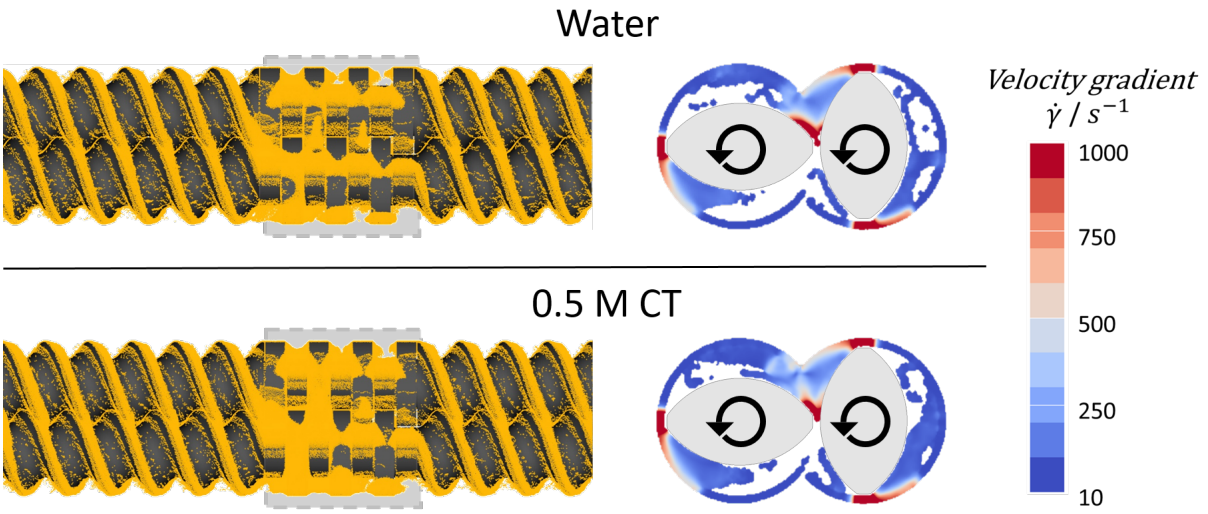

Figure 6.5: Filling behavior of the simulated domains (left) and shear rate distribution on a cutting plane through the first kneading disc (right) for simulations with rheological data from the ramp test for doughs prepared with water and 0.5 M CT.

The influence of shear viscosity on the local residence-time distribution is shown in figure 6.7. Both simulations exhibit the same overall trend. A gradual increase in the conveying elements and a steeper rise in the kneading block. The simulation based on the 0.5 M CT shear viscosity data shows slightly higher slopes in both regions, resulting in a total mean residence time of 8.6 s, only 1.2 s longer than that of the water-based dough.

Discussion

The simulations presented in chapter 6 do not reproduce the exact operating conditions of the structure-modulation trials described in chapter 2, as both the screw configuration and mass flow rate differed between experiment and simulation. The extrusion trials were conducted using a 40 L/D screw profile with only conveying elements and a short kneading block after the liquid-feeding port, whereas the simulations were performed with a 7.75 L/D screw featuring

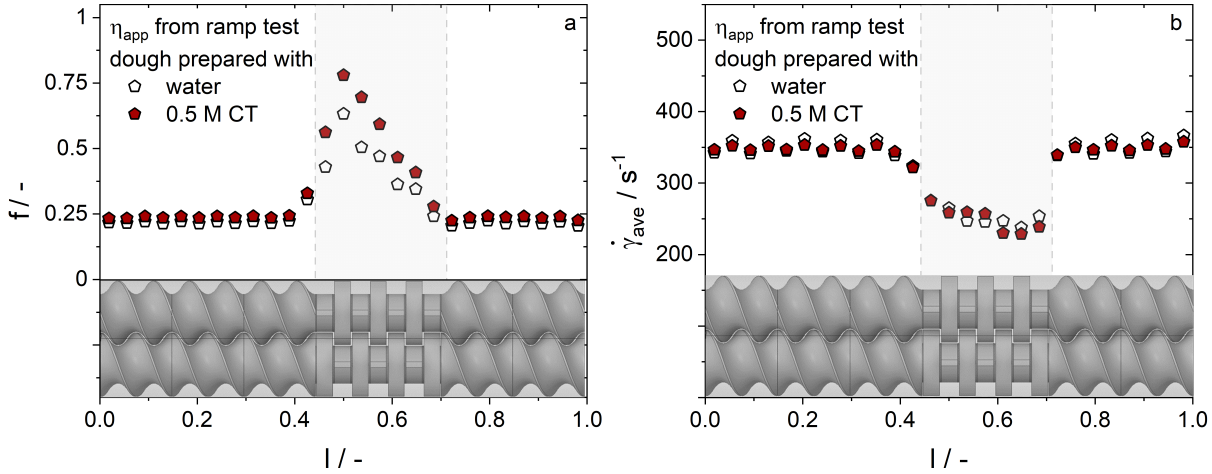

Figure 6.6: Influence of rheological data on the conveying behaviour examined by the mean value of the degree of filling (a) and the shear rate (b).

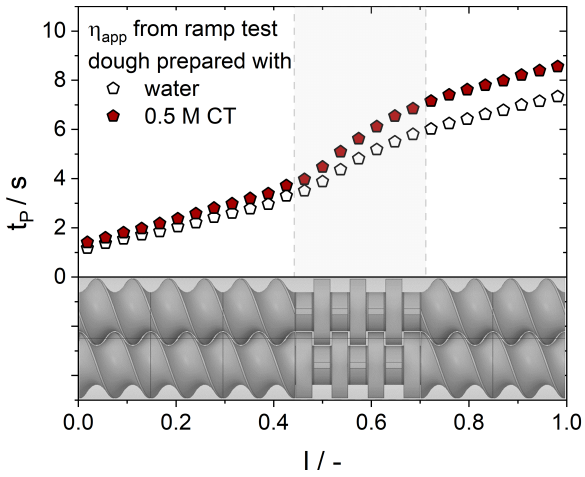

Figure 6.7: Influence of rheological data on the conveying behaviour examined by the mean value of the residence time.

a 1.75 L/D neutral kneading block. In addition, the experimental mass flow rate ($0.51\,\mathrm{kg\,h^{-1}}$) was substantially lower than that used in the simulation ($1.41\,\mathrm{kg\,h^{-1}}$). Nevertheless, the simulations using the two shear viscosity datasets provide valuable insights into the underlying local processing conditions and allow drawing parallels to the experimental observations.

The simulations show that the degree of filling is only marginally affected by the different shear viscosity inputs and remains generally low. Given that the experimental mass flow rate was even smaller and that the screw configuration consisted primarily of conveying elements, it is reasonable to assume that large parts of the extruder operated at degrees of fill below 0.25. A noticeable increase in degree of fill is expected only shortly before the die adapter, where back-pressure develops due to the geometric contraction and the attached cooling die, an aspect not captured in the current simulations. Under such low-fill conditions, torque measurements may be governed more strongly by screw friction and lubrication than by material transport. If acid addition promotes the presence of unbound water, which in turn lubricates the screws, this could explain the atypically low torque observed for the pH-reduced trials. Similarly, if water also lubricates the die, potentially caused by syneresis, slippage may occur at lower shear stresses, contributing to the lack of a clear pressure trend.

The low degree of filling may also explain the pronounced pressure fluctuations. These fluctuations suggest an unstable, cyclic process. Material accumulates in front of the die until sufficient pressure is generated to push it through. Once discharged, the fill level drops, pressure decreases, and insufficient material remains to sustain constant discharge. This repeated accumulation–release cycle results in the strong pressure oscillations seen experimentally.

The shear-rate distribution and average shear rate are largely unaffected by the choice of shear viscosity data, reflecting the minimal changes in degree of fill. More importantly, both datasets exhibit similar shear-thinning behavior. A fluid with a lower shear-thinning exponent would generate higher shear rates near the screw surface, especially at the screw tip, as illustrated in figure 3.8. For structure-modulation trials, shear stress scales primarily with the consistency

index K, resulting (in the absence of wall slip) in higher shear stresses for the acid-modified formulations.

Higher shear stress would typically lead to increased temperatures due to greater viscous energy dissipation. In the experiments, however, no temperature rise was observed upon acid addition. This discrepancy can plausabily be related to either wall slippage being present, or the very low degree of fill and short residence times in the conveying section (figure 6.7). Under such conditions, the dominant heat source is the barrel temperature rather than viscous dissipation, resulting in nearly identical material temperatures across all trials.

6.3 Main conclusions

In summary, the combined experimental and simulation results indicate that the unusual torque, pressure, and temperature trends observed during structure-modulated extrusion are primarily driven by formulation-dependent effects rather than by substantial changes in local processing conditions. The simulations suggest that the screw section operated at a low degree of fill, implying that lubrication effects likely dominated torque behavior, while limited material accumulation and discharge cycles may explain the pronounced pressure fluctuations. Since shear-rate distributions were largely unaffected by shear viscosity differences, the influence of acid addition was mainly evident through changes in shear stress rather than altered flow fields. However, temperature-dependent changes in the flow behavior index could modify shear-rate distributions. Taken together, these findings show that local processing conditions remained relatively stable and that formulation-induced lubrication or syneresis effects, leading to slippage in the cooling die, provide the most consistent explanation for the observed process behavior. The methods developed and applied in this thesis were essential in generating this process understanding, and each method, independent of this specific study, offers valuable standalone contributions for improving mechanistic insight into extrusion processing.

The **structure modulation method** provides a controlled and systematic way to alter protein network formation by adjusting pH through acid addition, without modifying process parameters. Beyond its use for method testing, this method represents a versatile tool for adjusting meat analogue texture, enabling targeted modulation of fibrousness, firmness, and elasticity by influencing protein–protein interactions at the molecular level.

The **ramp test method** offers a rapid and direct measurement of the shear viscosity under extrusion-relevant conditions. Although protein doughs may display discrepancies compared to capillary rheometry due to wall slip or gel fracture, the ramp test remains uniquely capable of providing shear viscosity data at high temperatures without water loss, making it highly valuable for evaluating flow behavior under conditions representative of the screw and die section.

The **moving-particle semi-implicit simulation method** enables the analysis of partially filled extruder screw section. This capability provides crucial insight into realistic local processing conditions, such as degree of fill, local residence time distributions, shear rate fields, and local temperature distributions. Thereby supporting more accurate interpretation of local processing conditions and process–structure relationships.

6.4 Limitations and recommendations

The goal of this thesis was to improve the mechanistic understanding of the twin-screw extrusion process of plant proteins for producing meat analogues. To this end, the structure modulation method, the MPS simulation method, and the ramp test method were presented, applied, and discussed. Together, these methods helped to interpret unusual observations of the common extrusion control parameters and revealed formulation-dependent effects that would otherwise have remained unclear. However, each method also carries specific limitations and offers opportunities for future work, which are summarized below.

6.4.1 Structure modulation

The structure modulation method has proven useful for modifying the structure of meat analogues made from soy protein isolate and wheat gluten by adding acetic and citric acids. To build a broader materials understanding, additional protein sources and acids should be investigated. For generating meat-like structures, acid addition was counterproductive. Therefore, exploring increases in pH could be an interesting complementary approach. Increasing the pH may soften the protein network via electrostatic repulsion, but this could be counteracted by the accelerated formation of disulfide bonds, particularly in gluten. The interplay between these strengthening and weakening mechanisms requires systematic investigation.

Moreover, shifting the pH in both the acidic and alkaline directions not only modulates structure but also affects the formation of covalent and non-covalent protein–protein interactions. Thus, controlled pH modification could be used to study fundamental mechanisms underlying protein structurability. Adjusting processing parameters, such as temperature, in parallel with pH changes might further reveal how structure formation can be stabilized or improved. Finally, the point of acid or alkali addition along the extruder could have a pronounced influence on the resulting structures. For example, pre-moistening proteins with water and adjusting pH shortly before the cooling die may allow the formation of novel structures.

6.4.2 The ramp test

The ramp test presented in this thesis accurately measures the shear viscosity of molten polyolefin polymers. When applied to protein doughs, however, instabilities and unusual results were observed. One limitation of the method is its restriction to shear rates up to $50\,\mathrm{s}^{-1}$ and one rotation. Because higher shear rates are present in extruder screw sections, extrapolation was required. A newly developed version of the closed-cavity rheometer capable of reaching $500\,\mathrm{s}^{-1}$ and performing continuous rotations could therefore provide a valuable extension for future steady-shear investigations.

Since the ramp test was only applied to soy protein isolate, applying it to other protein systems would help determine whether the observed instabilities are material-specific or method-related. To confirm whether protein doughs truly reach a flowing state, relaxation times could be correlated with the applied shear rate. Additionally, while this study focused on extrusion-relevant thermal and mechanical conditions, the influence of thermomechanical pretreatments on shear viscosity remains unknown and should be explored. To investigate lubrication or slippage effects more systematically, the rotating grooved part of the rheometer could be replaced with a polished plate, as has been done in rubber investigations Buhrin et al. (2022). Beyond these limitations, the ramp test has considerable potential for assessing the structurability of protein doughs, which should be explored in future work.

6.4.3 MPS simulatuon

The MPS simulation approach used in this thesis showed good qualitative agreement for the degree of filling in the kneading section when using a literature shear viscosity model for soy protein isolate. Nevertheless, full validation of the extrusion process simulation remains outstanding. Since the accuracy of the simulations strongly depends on the implemented shear viscosity data, validation should first be performed using a simpler model system such as molten polyolefins. The degree of fill, residence time distribution, pressure build-up, and temperature profile should all be compared against experimental measurements. If successful, the method could deliver quantitative information about the thermomechanical history of the material.

At present, only shear viscous properties of the SPI formulation have been included. Elastic effects and surface tension, which may influence conveying behavior, have been neglected. Alternatively, representing SPI as a solid in a discrete-element-method simulation may better capture its gel-like nature. Effects of slippage were also not implemented, despite several indications that slippage could occur in the screw section and significantly influence conveying behavior, shear stress, and temperature.

Furthermore, the simulated domain in this thesis covered only part of the screw section and examined only one operating parameter. It would be valuable to extend simulations to the full screw section, particularly when using a die adapter and associated pressure buildup. However, this would require material models spanning a large temperature range (25 °C to 150 °C). Finally, an inverse-engineering approach could be promising. Fitting particle size and slippage parameters until the simulated residence-time distribution matches the experimental one. Such an approach could deliver additional insight into the experiment, enable more robust validation, and deepen understanding of the flow behavior.

7 Appendix to Fibrous Structures of Protein Gels With Different Network Types

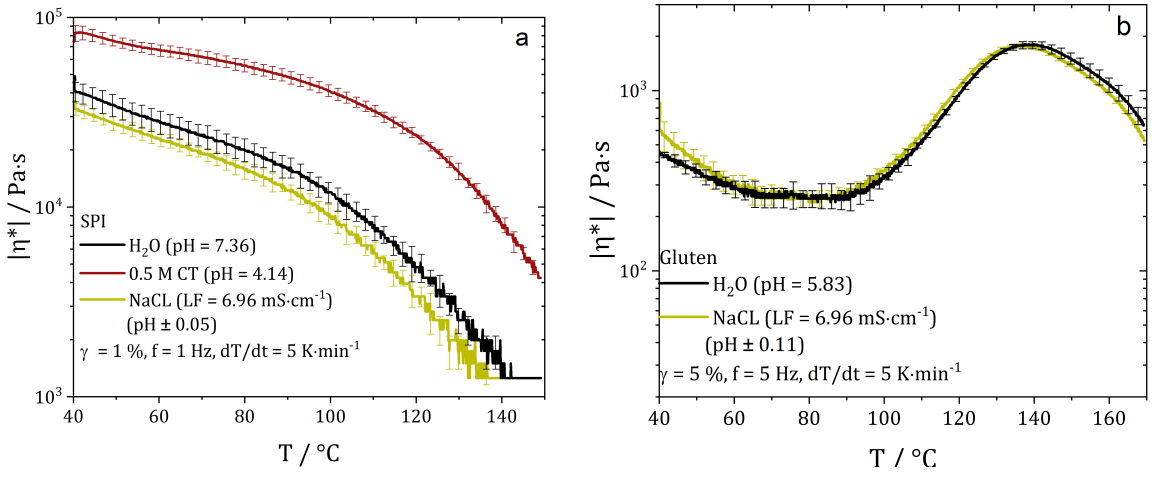

Figure 7.1: Temperature ramp of SPI (a) and gluten (b) doughs prepared with water, sodium chloride solution, and 0.5 M citric acid.

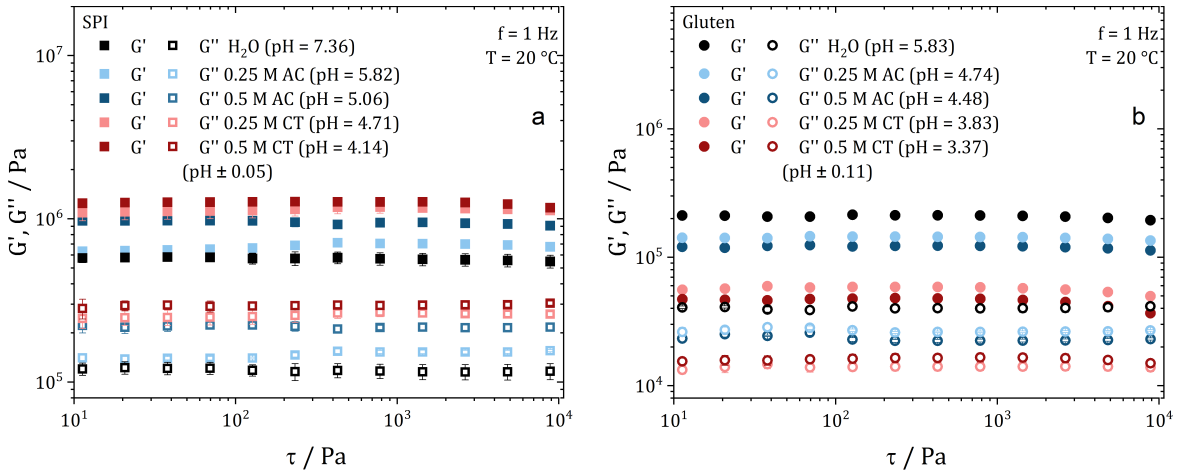

Figure 7.2: Amplitude tests of (a) soy protein isolate extrudates and (b) gluten extrudates produced with water, 0.25 M acetic acid, 0.5 M acetic acid, 0.25 M citric acid, and 0.5 M citric acid.

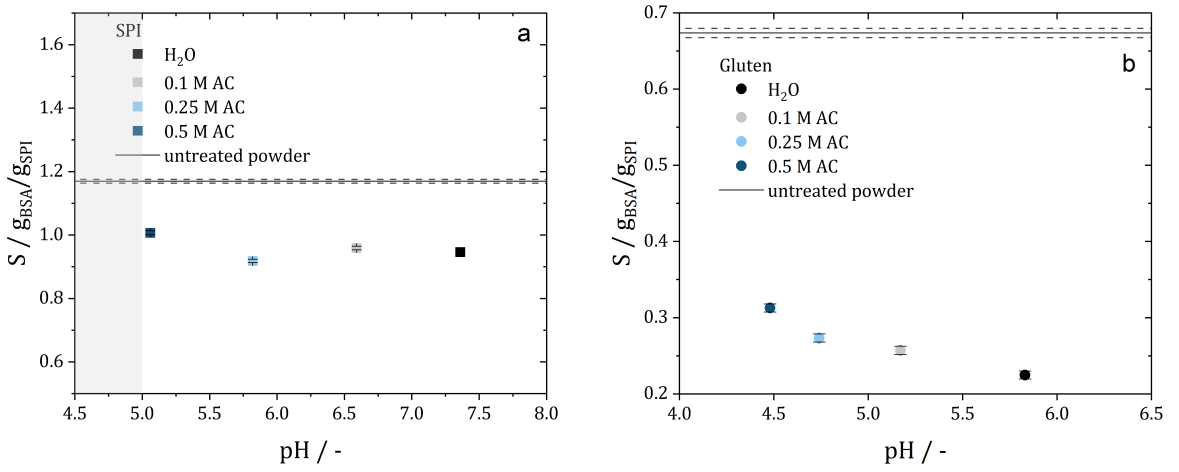

Figure 7.3: Solubility tests in reducing buffer of (a) soy protein isolate extrudates and (b) gluten extrudates produced with water, 0.25 M acetic acid, 0.5 M acetic acid, 0.25 M citric acid, and 0.5 M citric acid.

8 Appendix to Local Residence Time and Thermomechanical Stress Profile in Twin-Screw Extrusion

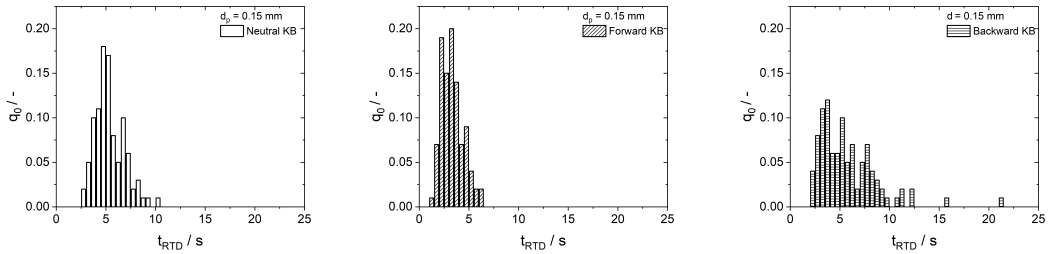

(a) Neutral. **(b)** Forward. **(c)** Backward.

Figure 8.1: Local residence time distribution in the different kneading blocks.

9 The Ramp Test From a Closed Cavity Rheometer

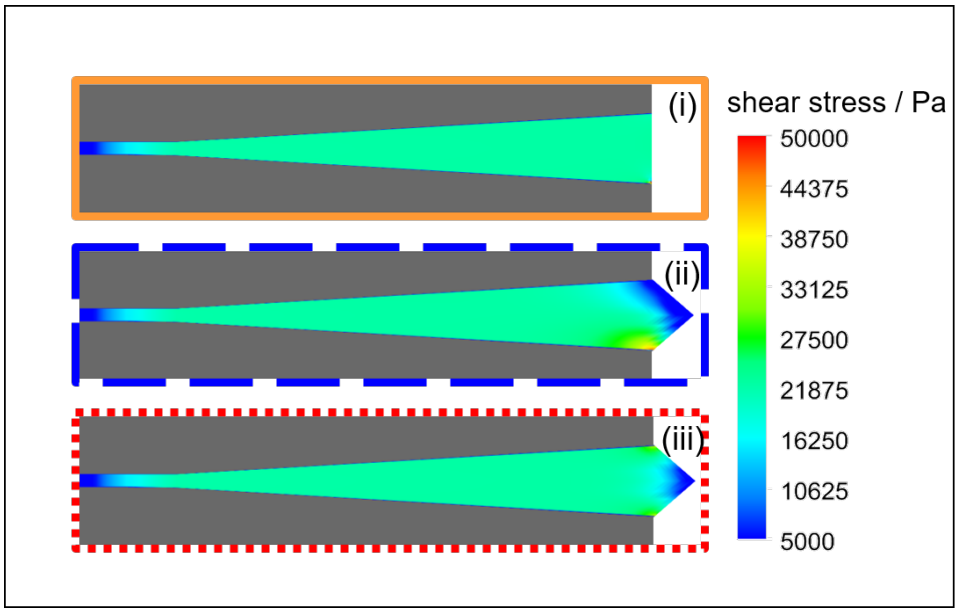

Figure 9.1: Shear stress distribution between the rotating lower cone and stationary upper cone offset at $\dot{\gamma}$ = 1 s^{-} −1 for (i) the simplified open cavity rheometer, (ii) the closed cavity rheometer (CCR) with no-slip boundary conditions at the sealing and (iii) the CCR with free slip boundary conditions at the sealing.

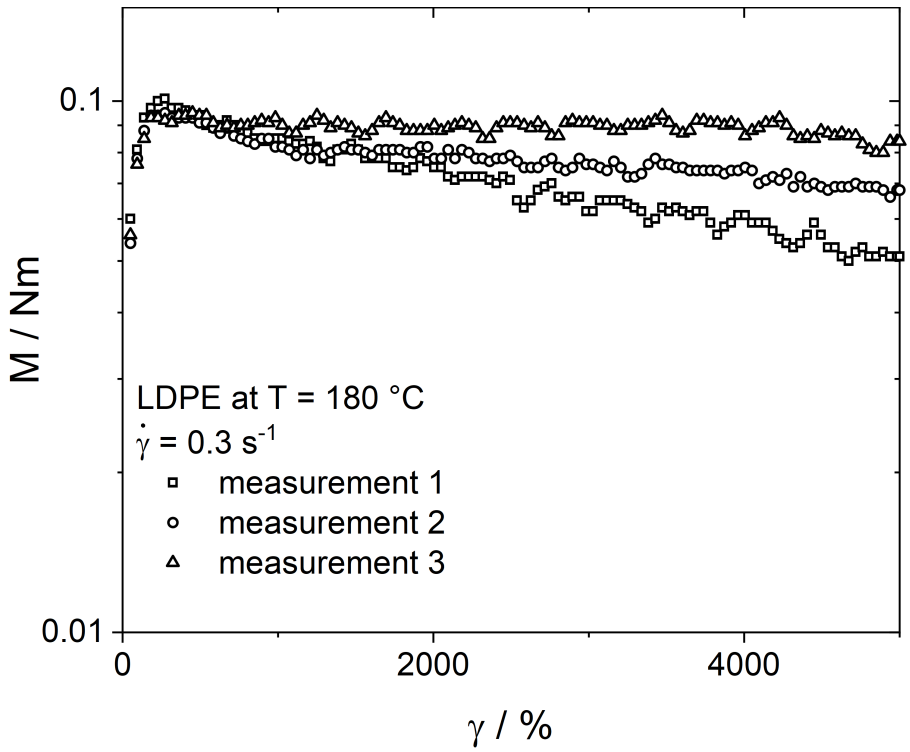

Figure 9.2: Triple determination of the torque M_{up} as a function of strain γ for LDPE at T = 180 °C at the shear rate of $\dot{\gamma} = 0.3\ s^{-}-1$. Torque decreases continuously after the overshoot, therefore no plateau value can be determined.

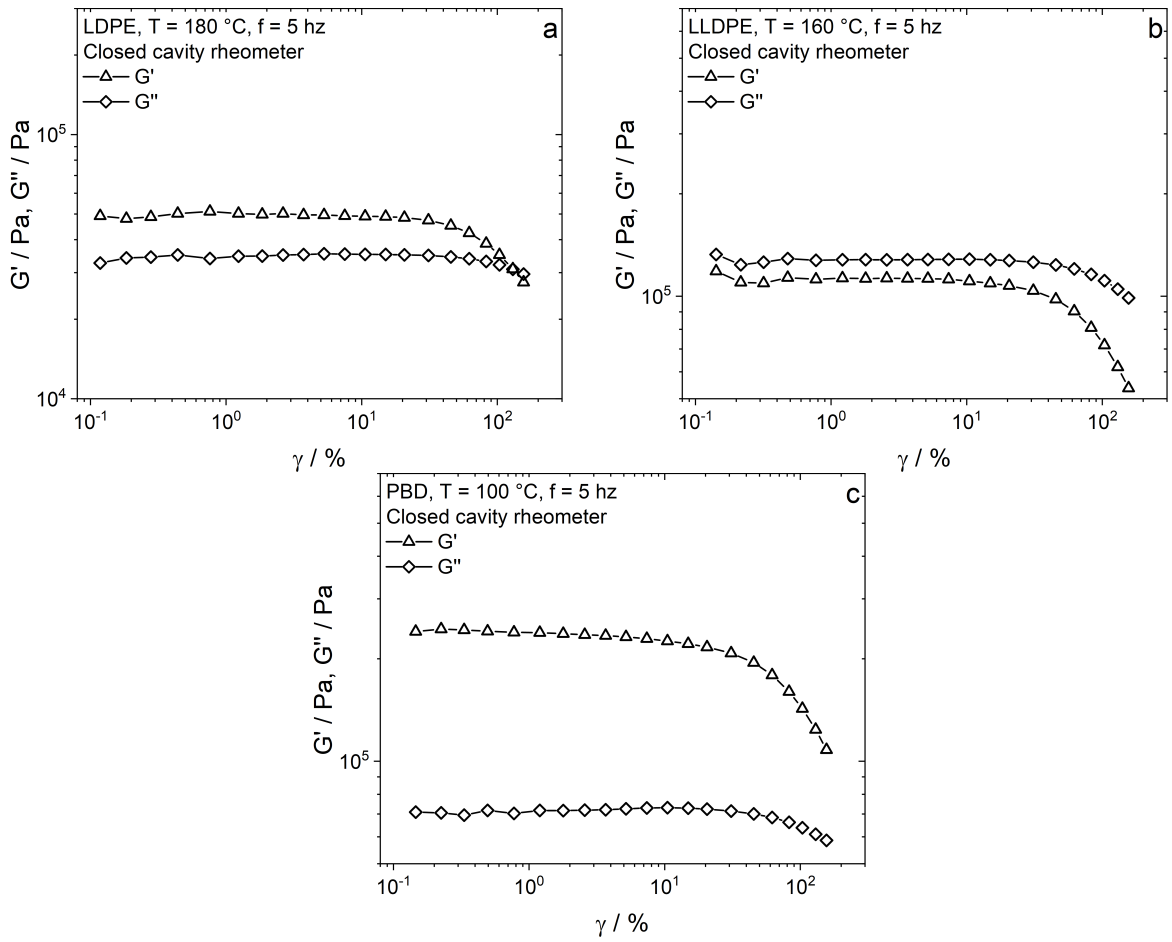

Figure 9.3: Storage modulus G' and loss modulus G'' as a function of strain γ obtained by strain sweep experiments with rotational closed cavity rheometer (CCR) for LDPE at T = 180 °C, b) LLDPE at T = 160 °C, and c) PBD at T = 100 °C

References

Abeykoon, C., Martin, P., Kelly, A., and Brown, E. (2012). A review and evaluation of melt temperature sensors for polymer extrusion. *Sens. Actuators A:Phys.*, 182:16.

Akdogan, H. (1996). Pressure, torque, and energy responses of a twin screw extruder at high moisture contents. *Food Res. Int.*, 29:423.

Akdogan, H. (1999). High moisture food extrusion. *Int. J. Food Sci. Technol.*, 34:195.

Ansari, M., Hatzikiriakos, S. G., Sukhadia, A. M., and Rohlfing, D. C. (2011). Rheology of Ziegler–Natta and metallocene high-density polyethylenes: broad molecular weight distribution effects. *Rheol. Acta*, 50:17.

Ansari, M., Inn, Y. W., Sukhadia, A. M., DesLauriers, P. J., and Hatzikiriakos, S. G. (2013). Wall slip of HDPEs: Molecular weight and molecular weight distribution effects. *J. Rheol.*, 57:927.

Apostolidis, C. and McLeay, F. (2016). Should we stop meating like this? Reducing meat consumption through substitution. *Food Policy*, 65:74.

Arêas, J. A. (1992). Extrusion of food proteins. *Crit. Rev. Food Sci. Nutr.*, 32:365.

Avalosse, T. (1996). Numerical simulation of distributive mixing in 3-D flows. *Macromol. Symp.*, 112:91.

Avalosse, T. and Rubin, Y. (2000). Analysis of mixing in corotating twin screw extruders through numerical simulation. *IPP*, 15:117.

Bagley, E. B. (1957). End corrections in the capillary flow of polyethylene. *J. Appl. Phys.*, 28:624.

Baig, M., Ajayi, F., Hamdi, M., Baba, W., Brishti, F., Khalid, N., Zhou, W., and Maqsood, S. (2025). Recent Research Advances in Meat Analogues: A Comprehensive Review on Production, Protein Sources, Quality Attributes, Analytical Techniques Used, and Consumer Perception. *Food Rev. Int.*, 41:236.

Bauer, H. and Khinast, J. (2022). Detecting mixing barriers in twin-screw extruder elements via lagrangian coherent structures. *Chem. Eng. Sci.*, 263:118069.

Bauer, H., Matić, J., Evans, R. C., Gryczke, A., Ketterhagen, W., Sinha, K., and Khinast, J. (2022). Determining local residence time distributions in twin-screw extruder elements via smoothed particle hydrodynamics. *Chem. Eng. Sci.*, 247:117029.

Belitz, H.-D., Grosch, W., and Schieberle, P. (2001). *Lehrbuch der Lebensmittelchemie*. Springer-Lehrbuch. Springer Berlin Heidelberg, Berlin, Heidelberg.

Beniwal, A. S., Singh, J., Kaur, L., Hardacre, A., and Singh, H. (2021). Meat analogs: Protein restructuring during thermomechanical processing. *Compr. Rev. Food Sci. Food Saf.*, 20:1221.

Booij, H. C., Leblans, P., Palmen, J., and Tiemersma-Thoone, G. (1983). Nonlinear viscoelasticity and the Cox–Merz relations for polymeric fluids. *J. Polym. Sci. Polym. Phys. Ed.*, 21:1703.

Bouvier, J.-M. and Campanella, O. (2014). *Extrusion Processing Technology: Food and Non-Food Biomaterials*. Wiley, 1 edition.

Buhrin, H. G., Rauschmann, T., and Graf, H.-J. (2022). New and highly efficient method to meaure steady shear viscosity and wall slip of rubber compounds: Closed-boundary rheometer (RPA). *Rubber Chem. Technol.*, 95:413.

Buhrin, H. G. and Rauschmann T. (2021). Viscosity measurement of filled rubber compounds—new insight for error free measurements. *Kautsch. Gummi Kunstst.*, 74:39.

Buhrin, H. G., Rauschmann T., and Graf H. J. (2021). Wall slip in processing rubber compound revisited. *Kautsch. Gummi Kunstst.*, 74:61.

Bundesminisrium für Ernährung und Landwirtschaft (2024). Deutschland, wie es isst. Technical report, BMEL, Berlin.

Burghelea, T. I., Griess, H. J., and Muenstedt, H. (2010). Comparative investigations of surface instabilities ("sharkskin") of a linear and a long-chain branched polyethylene. *J. Nonnewton. Fluid Mech.*, 165:1093.

Calumby, R. B. R. and Canevarolo, S. V. (2002). Residence Time Distribution Curves of Screw Elements in Twin-Srew Extruder. *Int. Poly. Process.*, 17:183.

Camire, M. (1991). Protein functionality modification by extrusion cooking. *J. Am. Oil Chem. Soc.*, 68:200–205.

Camire, M. E., Camire, A., and Krumhar, K. (1990). Chemical and nutritional changes in foods during extrusion. *Crit. Rev. Food Sci. Nutr.*, 29:35.

Cheftel, J. C., Kitagawa, M., and Quéguiner, C. (1992). New protein texturization processes by extrusion cooking at high moisture levels. *Food Rev. Int.*, 8:235.

Chen, F. L., Wei, Y. M., and Zhang, B. (2011). Chemical cross-linking and molecular aggregation of soybean protein during extrusion cooking at low and high moisture content. *LWT*, 44:957.

Chen, J. and Dickinson, E. (1999). Effect of surface character of filler particles on rheology of heat-set whey protein emulsion gels. *Coll. Surf. B: Biointerfaces*, 12:373.

Choi, H., Hahn, J., Kim, H.-S., and Choi, Y. (2025). The influence of cooling die temperature gradients on the texture of high-moisture meat analogs. *Food Chem.*, 468:142403.

Cox, W. P. and Merz, E. H. (1958). Correlation of dynamic and steady flow viscosities. *J. Polym. Sci.*, 28:619.

Dalle Fratte, E., D'hooge, D., Eeckhout, M., and Cardon, L. (2022). Principles and Guidelines for In-Line Viscometry in Cereal Extrusion. *Polymers*, 14:2316.

De Angelis, D., Van Der Goot, A.-J., Pasqualone, A., and Summo, C. (2024). Advancements in texturization processes for the development of plant-based meat analogs: a review. *Curr. Opin. Food Sci.*, 58:101192.

de Graaf, R. A., Woldringh, D. J., and Janssen, L. P. (1990). Material distribution in the partially filled zone of a twin-screw extruder. *Adv. Polym. Technol.*, 18:293.

Deng, X., Wang, S., Hammi, Y., Qian, L., and Liu, Y. (2020). A combined experimental and computational study of lubrication mechanism of high precision reducer adopting a worm gear drive with complicated space surface contact. *Tribol. Int.*, 146:106261.

Dickinson, E. (2012). Emulsion gels: The structuring of soft solids with protein-stabilized oil droplets. *Food Hydrocoll.*, 28:224.

Durin, A., De Micheli, P., Nguyen, H.-C., David, C., Valette, R., and Vergnes, B. (2014). Comparison between 1D and 3D Approaches for Twin-Screw Extrusion Simulation. *Int. Poly. Process.*, 29:641.

Eitzlmayr, A. and Khinast, J. (2015). Co-rotating twin-screw extruders: Detailed analysis of conveying elements based on smoothed particle hydrodynamics. Part 1: Hydrodynamics. *Chem. Eng. Sci.*, 134:861.

Ellwanger, F., Fuhrmann, M., Karbstein, H. P., and Saavedra Isusi, G. I. (2024). Influence of lowering the pH value on the generation of fibrous structures of protein gels with different network types. *Gels*, 10:173.

Ellwanger, F., Georgantopoulos, C. K., Karbstein, H. P., Wilhelm, M., and Azad Emin, M. (2023a). Application of the ramp test from a closed cavity rheometer to obtain the steady-state shear viscosity. *Appl. Rheol.*, 33:20220149.

Ellwanger, F., Pernice, L., Karbstein, H. P., and Emin, M. A. (2023b). Investigating local residence time and thermomechanical stress profile in twin-screw extrusion of plant proteins by using the moving particle semi-implicit simulation method. *J. Food Eng.*, 359:111665.

Emin, M. and Schuchmann, H. (2013). Droplet breakup and coalescence in a twin-screw extrusion processing of starch based matrix. *J. Food Eng.*, 116:118.

Emin, M. and Schuchmann, H. (2017). A mechanistic approach to analyze extrusion processing of biopolymers by numerical, rheological, and optical methods. *Trends Food Sci. Technol.*, 60:88.

Emin, M. A., Quevedo, M., Wilhelm, M., and Karbstein, H. P. (2017). Analysis of the reaction behavior of highly concentrated plant proteins in extrusion-like conditions. *Innov. Food Sci. Emerg. Technol.*, 44:15.

Emin, M. A., Teumer, T., Schmitt, W., Rädle, M., and Schuchmann, H. P. (2016). Measurement of the true melt temperature in a twin-screw extrusion processing of starch based matrices via infrared sensor. *J. Food Eng.*, 170:119.

Emin, M. A., Wittek, P., and Schwegler, Y. (2021). Numerical analysis of thermal and mechanical stress profile during the extrusion processing of plasticized starch by non-isothermal flow simulation. *J. Food Eng.*, 294:110407.

Fischer, T. (2004). Effect of extrusion cooking on protein modification in wheat flour. *Eur. Food Res. Technol.*, 218:128.

Foo, S. K. (2004). *Effect of temperature and pH on the solubility of soy protein*. B. Sc., School of Engineering, Queensland.

Fraeye, I., Colle, I., Vandevenne, E., Duvetter, T., van Buggenhout, S., Moldenaers, P., van Loey, A., and Hendrickx, M. (2010). Influence of pectin structure on texture of pectin–calcium gels. *Innov. Food Sci. Emerg. Technol.*, 11:401.

Fujio, Y., Hayashi, N., and Hayakawa, I. (1991). Effect of moisture content on flow behaviour of molten soy-protein isolate under an elevated temperature. *IJFST*, 26:45.

Fukuda, G., Bigio, D. I., Andersen, P., and Wetzel, M. (2015). A new scale-up approach for dispersive mixing in twin-screw compounding. In *AIP Conf. Proceedings*, AIP Conference Proceedings, page 100007, Cleveland, Ohio, USA. AIP Publishing LLC.

Fukuzawa, Y., Shigeishi, T., Munemasa, K., Tomiyama, H., Yamanoi, M., and Koshizuka, S. (2017). Analysis of polymer plasticization by DEM–MPS coupling simulation. In *International Conference on Particle-based Methods. Fundamentals and Applications*, Hannover.

García-Franco, C. A. (2013). A note on the elasticity of polymer melts described by primary normal stress difference (N 1). *Macromol. Symp.*, 325-326:184.

Gennadios, A., Brandenburg, A. H., Weller, C. L., and Testin, R. F. (1993). Effect of pH on properties of wheat gluten and soy protein isolate films. *J. Agric. Food Chem.*, 41:1835.

Georgantopoulos, C. K., Esfahani, M. K., Botha, C., Naue, I. F. C., Dingenouts, N., Causa, A., Kádár, R., and Wilhelm, M. (2021). Mechano-optical characterization of extrusion flow instabilities in Styrene-Butadiene rubbers: Investigating the influence of molecular properties and die geometry. *Macromol. Mater. Eng.*, 306:6.

Georgantopoulos, C. K., Esfahani, M. K., Naue, I. F. C., Wilhelm, M., and Kádár, R. (2023). Role of molecular architecture and temperature on extrusion melt flow instabilities of two industrial LLDPE and LDPE polyethylenes investigated by capillary rheology, high-pressure sensitivity slit die and optical analysis. *J. Appl. Polym. Sci.*, 140:6.

Georgantopoulos, C. K., Esfahani, M. K., Pollard, M. A., Naue, I. F. C., Causa, A., Kádár, R., and Wilhelm, M. (2022). Derivation of a qualitative model for the spatial characteristic wavelength of extrusion flow instabilities: Investigation of a polybutadiene rubber through capillary, slit and complex geometry extrusion dies. *Macromol. Mater. Eng.*, 307:17.

Guan, T., Sägesser, C., Villiger, R., Zychowski, L., Kohlbrecher, J., Dumpler, J., Mathys, A., Rühs, P., Fischer, P., and Matsarskaia, O. (2024). In situ studies of plant-based meat analog texturization. *Food Hydrocoll.*, 155:110215.

Guyony, V., Fayolle, F., and Jury, V. (2022). Die dimensions impact on fibrous plant protein formation during high moisture extrusion. *Appl. Food Res.*, 2:100228.

Hallström, E., Röös, E., and Börjesson, P. (2014). Sustainable meat consumption: A quantitative analysis of nutritional intake, greenhouse gas emissions and land use from a Swedish perspective. *Food Policy*, 47:81.

Hatzikiriakos, S. G. (2012). Wall slip of molten polymers. *Prog. Polym. Sci.*, 37:624.

Hatzikiriakos, S. G. and Dealy, J. M. (1992). Wall slip of molten high density polyethylenes. II. Capillary rheometer studies. *J. Rheol.*, 36:703.

Hatzikiriakos, S. G. and Migler, K. B. (2004). *Polymer processing instabilities*. CRC Press.

Hayashi, N., Hayakawa, I., and Fujio, Y. (1991). Entrance effect correction on the flow of moisturized soy protein isolate melt in an extrusion viscometer. *IJFST*, 26:567.

Hayashi, N., Hayakawa, I., and Fujio, Y. (1993). Flow behaviour of soy protein isolate melt with low and intermediate moisture levels at an elevated temperature. *J. Food Eng.*, 18:1.

Hayashi, N., Noma, K., Hayakawa, I., and Fujio, Y. (1992). Influence of time-temperature history and strain history on the melt rheology of soy protein isolate at an elevated temperature. *IJFST*, 27:297.

Herschel, W. H. and Bulkley, R. (1926). Konsistenzmessungen von Gummi-Benzollösungen. *Kolloid-Zeitschrift*, 39:291.

Heyer, P., Wurm, C., and Ehrentraut, H. (2022). Measurement and visualization of slip in rubber flow. In *Proceedings of the Annual European Rheology Conference*, Seville, Spain.

Hicks, C. I. and See, H. (2010). The rheological characterisation of bread dough using capillary rheometry. *Rheol. Acta*, page 719.

Kaletunç, G. and Breslauer, K. J. (1996). Construction of a wheat-flour state diagram: Application to extrusion processing. *J. Therm. Anal.*, 47:1267.

Kaunisto, E., Wassén, S., and Stading, M. (2024). A thermodynamical finite element model of the fibre formation process during extrusion of high-moisture meat analogues. *J. Food Eng.*, 362:111760.

Kendler, C., Duchardt, A., Karbstein, H. P., and Emin, M. A. (2021). Effect of oil content and oil addition point on the extrusion processing of wheat gluten-based meat analogues. *Foods*, 10:697.

Keßner, U., Kaschta, J., and Münstedt, H. (2009). Determination of method-invariant activation energies of long-chain branched low-density polyethylenes. *J. Polym. Sci.*, 53:1001.

Kinsella, J. E. and Melachouris, N. (1976). Functional properties of proteins in foods: A survey. *Crit. Rev. Food Sci. Nutr.*, 7:219.

Kleinschmidt, D., Brüning, F., and Petzke, J. (2023). Wall slip-free viscosity determination of filled rubber compounds using steady-state shear measurements. *Polymers*, 15:4406.

Koch, L., Emin, M. A., and Schuchmann, H. (2017a). Influence of processing conditions on the formation of whey protein-citrus pectin conjugates in extrusion. *J. Food Eng.*, 193:1.

Koch, L., Hummel, L., Schuchmann, H. P., and Emin, M. A. (2017b). Influence of Defined Shear Rates on Structural Changes and Functional Properties of Highly Concentrated Whey Protein Isolate-Citrus Pectin Blends at Elevated Temperatures. *Food Biophys.*, 12:309.

Kohlgrüber, K., editor (2019). *Co-rotating twin-screw extruders: Fundamentals*. Carl Hanser Verlag GmbH & Co. KG, München.

Koopmans, R., Den Doelder, J., and Molenaar, J. (2010). *Polymer melt fracture*. CRC Press.

Koshizuka, S. and Oka, Y. (1996). Moving-particle semi-implicit method for fragmentation of incompressible fluid. *Nucl. Sci. Eng.*, 123:421.

Kristiawan, M., Della Valle, G., and Berzin, F. (2022). Extrusion Simulation for the Design of Cereal and Legume Foods. *Foods*, 11:1780.

Kumar, P., Chatli, M. K., Mehta, N., Singh, P., Malav, O. P., and Verma, A. K. (2017). Meat analogues: Health promising sustainable meat substitutes. *Crit. Rev. Food Sci. Nutr.*, 57:923.

Kyriakopoulou, K., Keppler, J. K., and Van Der Goot, A.-J. (2021). Functionality of Ingredients and Additives in Plant-Based Meat Analogues. *Foods*, 10:600.

Lagrain, B., Goderis, B., Brijs, K., and Delcour, J. A. (2010). Molecular basis of processing wheat gluten toward biobased materials. *Biomacromolecules*, 11:533.

Langstraat, T. D., Jansens, K., Delcour, J. A., van Puyvelde, P., and Goderis, B. (2015). Controlling wheat gluten cross-linking for high temperature processing. *Ind. Crops Prod.*, 72:119.

Leblanc, J. L. and Mongruel, A. (2001). A thorough examination of a torsional dynamic rheometer with a closed oscillating cavity. *Prog. Rubber Plast. Recycl. Technol.*, 17:162.

Leeb, C., Maiser, B., and Schuchmann, H. (2008). Bestimmung der Verweilzeitverteilung bei der Kochextrusion von Maisgrieß in einem Hochgeschwindigkeitsextruder. *Chem. Ing. Tech.*, 80(8):1175–1179.

Li, D., Zhang, T., Gao, F., Zhou, C., Sun, D., Gao, Y., and Wu, M. (2024). The study of numerical simulation and texture of soybean protein based on high moisture extrusion with different screw elements. *Innov. Food Sci. Emerg. Technol.*, 92:103560.

Liu, W.-C., Halley, P., and Gilbert, R. (2010). Mechanism of Degradation of Starch, a Highly Branched Polymer, during Extrusion. *Macromol.*, 43:2855.

Malhotra, A. and Coupland, J. N. (2004). The effect of surfactants on the solubility, zeta potential, and viscosity of soy protein isolates. *Food Hydrocoll.*, 18:101.

Manjunhata Prabhu, B. and Shanthala, P. (2025). Emerging trends in meat Analogues: Innovations, challenges, limitations, future directions, and market dynamics. *J. Curr. Res. Food Sci.*, 6:36.

Markovitz, H. (1975). Superposition in rheology. *J. Polym. Sci., Polym. Symp.*, 50:431.

Martin, C. (2016). Twin Screw Extruders as Continuous Mixers for Thermal Processing: a Technical and Historical Perspective. *AAPS PharmSciTech*, 17:3.

Mavridis, H. and Shroff, R. N. (1992). Temperature dependence of polyolefin melt rheology. *Polym. Eng. Sci.*, 32:1778.

McClements, D. J. (2024). Soft matter physics approaches for creating plant-based meat analogs. *Curr. Opin. Food Sci.*, 55:101120.

Meißner, M., editor (2016). *Standard-Methoden für Getreide, Mehl und Brot*. Verlag Moritz Schäfer, Detmold, 8., überarbeitete und erweiterte auflage mit allen aktuellen icc-standards edition.

Meuser, F., Van Lengerich, B., and Reimers, H. (1984). Kochextrusion von Stärken. Vergleich experimenteller Ergebnisse zwischen Laborextrudern und Produktionsextrudern mittels Systemanalyse. *Starch - Stärke*, 36:194.

Meza Gonzalez, J. F. and Nirschl, H. (2023). Numerical investigation of the local shear rate in a twin-screw extruder for the continuous processing of Li-ion battery electrode slurries. *Energy Technol.*, 11:2201517.

Mezger, T. (2021). *Applied rheology*. Anton Paar GmbH, Graz, 8th edition edition.

Moll, T., Hellenbroich, G., Herold, K., and Beykirch, R. (2021). Co-simulation of efficiency, lubrication and thermal management for trans-missions with integrated electrical machine. *ATZ Worldw.*, 123:58.

Monaghan, J. (2005). Smoothed particle hydrodynamics. *Rep. Prog. Phys.*, 68:1703.

Mooney, M. (1931). Explicit formulas for slip and fluidity. *J Rheol.*, 2:210.

Morrison, F. A. (2001). *Understanding rheology*. Topics in chemical engineering. Oxford University Press, New York.

Muhialdin, B. J. and Ubbink, J. (2023). Effects of pH and aging on the texture and physicochemical properties of extruded pea protein isolate. *Food Hydrocoll.*, 140:108639.

Mujumdar, A., Beris, A. N., and Metzner, A. B. (2002). Transient phenomena in thixotropic systems. *J. Nonnewton. Fluid Mech.*, 102:157.

Nakai, S. (1983). Structure-function relationships of food proteins: with an emphasis on the importance of protein hydrophobicity. *J. Agric. Food Chem.*, 31:676.

Nieuwland, M., Heijnis, W., van der Goot, A.-J., and Hamoen, R. (2023). XRT for visualizing microstructure of extruded meat replacers. *Curr. Res. Food Sci.*, 6:100457.

Nisov, A., Nikinmaa, M., Nordlund, E., and Sozer, N. (2022). Effect of pH and temperature on fibrous structure formation of plant proteins during high-moisture extrusion processing. *Food Res. Int.*, 156:111089.

O Flynn, T. D., Hogan, S. A., Daly, D. F. M., O Mahony, J. A., and McCarthy, N. A. (2021). Rheological and solubility properties of soy protein isolate. *Molecules*, 26:3015.

Oberlehner, J., Cassagnau, P., and Michel, A. (1994). Local residence time distribution in a twin screw extruder. *Chem. Eng. Sci.*, 49:3897.

Opaluwa, C., Deskovski, S., Karbstein, H. P., and Emin, M. A. (2024). Effect of oil on the rheological properties and reaction behavior of highly concentrated wheat gluten under conditions relevant to high moisture extrusion. *Future Foods*, 34:100307.

Pappas, W., Brown, W., Fukuda, G., Adnew, R., and Bigio, D. (2012). Variable strength stress bead analysis in a twin screw extruder. In *Annual Technical Conference of the Society of Plastics Engineers 2012*, Orlando, Florida.

Paschedag, A. (2004). *CFD in der Verfahrenstechnik: Allgemeine Grundlagen und mehrphasige Anwendungen*. Wiley, 1 edition.

Pietsch, V., Werner, R., Karbstein, H. P., and Emin, M. A. (2019a). High moisture extrusion of wheat gluten: Relationship between process parameters, protein polymerization, and final product characteristics. *J. Food Eng.*, 259:3.

Pietsch, V. L., Bühler, J. M., Karbstein, H. P., and Emin, M. A. (2019b). High moisture extrusion of soy protein concentrate: Influence of thermomechanical treatment on protein-protein interactions and rheological properties. *J. Food Eng.*, 251:11.

Pietsch, V. L., Emin, M. A., and Schuchmann, H. P. (2017). Process conditions influencing wheat gluten polymerization during high moisture extrusion of meat analog products. *J. Food Eng.*, 198:28.

Pietsch, V. L., Schöffel, F., Rädle, M., Karbstein, H. P., and Emin, M. A. (2019c). High moisture extrusion of wheat gluten: Modeling of the polymerization behavior in the screw section of the extrusion process. *J. Food Eng.*, 246:67.

Quevedo, M., Karbstein, H., and Emin, M. (2021a). Concentration-dependent changes in the reaction behavior of whey proteins: Diffusion-controlled or transition state-controlled reactions? *Food Hydrocoll.*, 118:106745.

Quevedo, M., Karbstein, H., and Emin, M. (2021b). Influence of thermomechanical treatment and pH on the denaturation kinetics of highly concentrated whey protein isolate. *J. Food Eng.*, 292:110294.

Quevedo, M., Kulozik, U., Karbstein, H., and Emin, M. A. (2020). Kinetics of denaturation and aggregation of highly concentrated beta-Lactoglobulin under defined thermomechanical treatment. *J. Food Eng.*, 274:109825.

Rabinowitsch, B. (1929). Über die viskosität und elastizität von solen. *Z. fur Phys. Chem.*, 145A:1.

Rauschmann, T., Buhrin, H. G., Wirth, O., and Reddy, S. (2022). Steady shear viscosity measurements of filled rubber compounds using new enhanced RPA technology. In *Kurzfassung der Vorträge*, Nuremberg, Germany.

Rauwendaal, C. (2014). *Polymer extrusion*. Hanser Publishers, Munich, 5th edition edition.

Renkema, J. M. (2004). Relations between rheological properties and network structure of soy protein gels. *Food Hydrocoll.*, 18:39.

Rubinstein, M. and Colby, R. H. (2014). *Polymer physics*. Oxford Univ. Press, Oxford, repr edition.

Saavedra I., G. I., Pietsch, V., Beutler, P., Hoehne, S., and Leister, N. (2023). Influence of rapeseed oil on extruded plant-based meat analogues: Assessing mechanical and rheological properties. *Processes*, 11:1871.

Sarhangi Fard, A. and Anderson, P. D. (2013). Simulation of distributive mixing inside mixing elements of co-rotating twin-screw extruders. *Comput. Fluids*, 87:79.

Schmid, V., Mayer-Miebach, E., Behsnilian, D., Briviba, K., Karbstein, H. P., and Emin, M. A. (2022). Enrichment of starch-based extruded cereals with chokeberry (Aronia melanocarpa) pomace: Influence of processing conditions on techno-functional and sensory related properties, dietary fibre and polyphenol content as well as in vitro digestibility. *LWT*, 154:112610.

Schreuders, F., Sagis, L., Bodnár, I., Erni, P., Boom, R. M., and van der Goot, A.-J. (2021a). Mapping the texture of plant protein blends for meat analogues. *Food Hydrocoll.*, 118:106753.

Schreuders, F. K. G., Sagis, L. M. C., Bodnár, I., Erni, P., Boom, R. M., and van der Goot, A. J. (2021b). Small and large oscillatory shear properties of concentrated proteins. *Food Hydrocoll.*, 110:106172.

Schuchmann, H. (2008). Extrusion zur Gestaltung von Lebensmittelstrukturen. *Chem. Ing. Tech.*, 80:1097.

Schwab, L., Hojdis, N., Lacayo, J., and Wilhelm, M. (2016). Fourier-transform rheology of unvulcanized, carbon black filled styrene butadiene rubber. *Macromol. Mater. Eng.*, 301:457.

Shen, Z., Liu, Z., Rui., X., Chen, X., Jiang, M., and Dong, M. (2021). Effects of fat content on the textural and in vivo buccal breakdown properties of soy yogurt. *J. Texture Stud.*, 52:334.

Singh, R. P. and Heldman, D. R. (2009). *Introduction to food engineering*. Food science and technology, international series. Acadademic Press Elsevier, Amsterdam, 4 edition.

Skadsem, H. J., Leulseged, A., and Cayeux, E. (2019). Measurement of drilling fluid rheology and modeling of thixotropic behavior. *Appl. Rheol.*, 29:1.

Skrzeszewska, P. J., Sprakel, J., Wolf, F. A., Fokkink, R., Cohen Stuart, M. A., and van der Gucht, J. (2010). Fracture and self-healing in a well-defined self-assembled polymer network. *Macromol.*, 43:3542.

Snijkers, F., Ratkanthwar, K., Vlassopoulos, D., and Hadjichristidis, N. (2013a). Viscoelasticity, nonlinear shear start-up, and relaxation of entangled star polymers. *Macromol.*, 46:5702.

Snijkers, F. and Vlassopoulos, D. (2014). Appraisal of the Cox-Merz rule for well-characterized entangled linear and branched polymers. *Rheol. Acta*, 53:935.

Snijkers, F., Vlassopoulos, D., Ianniruberto, G., Marrucci, G., Lee, H., Yang, J., and Chang, T. (2013b). Double stress overshoot in start-up of simple shear flow of entangled comb polymers. *ACS Macro Lett.*, 2:601.

Snijkers, F., Vlassopoulos, D., Lee, H., Yang, J., Chang, T., Driva, P., and Hadjichristidis, N. (2013c). Start-up and relaxation of well-characterized comb polymers in simple shear. *J. Rheol.*, 57:1079.

Spiegel, T. and Huss, M. (2002). Whey protein aggregation under shear conditions – effects of pH-value and removal of calcium. *Int. J. Food Sci. Technol.*, 37:559.

Stadler, F. J., Gabriel, C., and Münstedt, H. (2007). Influence of short-chain branching of polyethylenes on the temperature dependence of rheological properties in shear. *Macromol. Chem. Phys.*, 208:2449.

Steffe, J. (1996). *Rheological methods in food process engineering*. Freeman Press, East Lansing, 2. ed edition.

Stokes, J. R. and Telford, J. H. (2004). Measuring the yield behaviour of structured fluids. *J. Nonnewton. Fluid Mech.*, 124:137.

Sun, D., Zhou, C., Yu, H., Wang, B., Li, Y., and Wu, M. (2022). Integrated numerical simulation and quality attributes of soybean protein isolate extrusion under different screw speeds and combinations. *Innov. Food Sci. Emerg. Technol.*, 79:103053.

Sweat V. E. (1986). Thermal propeties of foods. In Rao M. A., R. S. H., editor, *Engineering properties of food*, page 87. CRC Press, New York.

Sägesser, C., Mair, T., Braun, A., Dumpler, J., Fischer, P., and Mathys, A. (2025). Application of a shear cell for the simulation of extrusion to test the structurability of raw materials. *Food Hydrocoll.*, 160:110736.

Taghian Dinani, S., Broekema, N., Boom, R., and Van Der Goot, A.-J. (2023). Investigation potential of hydrocolloids in meat analogue preparation. *Food Hydrocoll.*, 135:108199.

Takeda, K., Matsumura, Y., and Shimizu, M. (2001). Emulsifying and surface properties of wheat gluten under acidic conditions. *J. Food Sci.*, 66:393.

Thornell, T. L., Helfrecht, B. A., Mullen, S. A., Bawiskar, A., and Erk, K. A. (2014). Fracture-healing kinetics of thermoreversible physical gels quantified by shear rheophysical experiments. *ACS Macro Lett.*, 3:1069.

Tolstoguzov, V. B. (1993). Thermoplastic extrusion-the mechanism of the formation of extrudate structure and properties. *J. Am. Oil Chem. Soc.*, 70:417.

Totosaus, A., Montejano, J. G., Salazar, J. A., and Guerrero, I. (2002). A review of physical and chemical protein-gel induction. *Int. J. Food Sci. Technol.*, 37:589.

Tsegaye, B., Barman, S., Bovagne, L., Ellwanger, F., Kaunisto, E., Lorén, N., Kádár, R., and Stading, M. (2025). Rheological properties of pea protein melts used for producing meat analogues. *Appl. Rheol.*, 35:20250036. Publisher: Walter de Gruyter GmbH.

Van Den Einde, R., Akkermans, C., Van Der Goot, A., and Boom, R. (2004). Molecular breakdown of corn starch by thermal and mechanical effects. *Carbohydr. Polym.*, 56:415.

Van Der Goot, A. J., Peighambardoust, S. H., Akkermans, C., and Van Oosten-Manski, J. M. (2008). Creating Novel Structures in Food Materials: The Role of Well-Defined Shear Flow. *Food Biophysics*, 3:120–125.

van der Sman, R. G. M. and van der Goot, A. J. (2023). Hypotheses concerning structuring of extruded meat analogs. *Curr. Res. Food Sci.*, 6:100510.

van der Sman, R. G. M., Voudouris, P., and Hamoen, J. R. (2024). Extrapolation of classical rheometry of plant protein pastes to extrusion conditions. *Food Hydrocoll.*, 150:109663.

Van Esbroeck, T., Sala, G., Stieger, M., and Scholten, E. (2024). Effect of structural characteristics on functional properties of textured vegetable proteins. *Food Hydrocoll.*, 149:109529.

van Lengerich, B. (1990). Influence of extrusion processing on in-line rheological behavior, structure, and function of wheat starch. In Faridi, H. and Faubion, J. M., editors, *Dough Rheology and Baked Product Texture*, volume 32, page 421. Springer US, Boston, MA.

Vergnes, B., Della Valle, G., and Delamare, L. (1998). A global computer software for polymer flows in corotating twin screw extruders. *Polym. Eng. Sci.*, 38:1781.

Versteeg, H. K. and Malalasekera, W. (2007). *An introduction to computational fluid dynamics: the finite volume method*. Pearson/Prentice Hall, Harlow, 2. ed., [nachdr.] edition.

Vittorias, I., Lilge, D., Baroso, V., and Wilhelm, M. (2011). Linear and non-linear rheology of linear polydisperse polyethylene. *Rheol. Acta*, 50:691.

Wagner, C. E. and Ganjyal, G. M. (2024). Impact of functional dietary fiber incorporation on the appearance and mechanical properties of extruded high moisture meat analogs. *J. Food Sci.*, 89:4953.

Webb, D., Dogan, H., Li, Y., and Alavi, S. (2023). Use of legume flours and fiber for tailoring structure and texture of pea protein-based extruded meat alternatives. *J. Food Sci.*, 88:57.

Webb, D., Plattner, B., Donald, E., Funk, D., Plattner, B. S., and Alavi, S. (2020). Role of chickpea flour in texturization of extruded pea protein. *J. Food Sci.*, 85:4180.

Willats, W. G., Orfila, C., Limberg, G., Buchholt, H. C., van Alebeek, G. J., Voragen, A. G., Marcus, S. E., Christensen, T. M., Mikkelsen, J. D., Murray, B. S., and Knox, J. P. (2001). Modulation of the degree and pattern of methyl-esterification of pectic homogalacturonan in plant cell walls. Implications for pectin methyl esterase action, matrix properties, and cell adhesion. *J. Biol. Chem.*, 276:19404.

Williams, M., Landel, R., and Ferry, J. (1955). The Temperature Dependence of Relaxation Mechanisms in Amorphous Polymers and Other Glass-forming Liquids. *J. Am. Chem. Soc.*, 77(14):3701–3707.

Winter, H. H. (2009). Three views of viscoelasticity for Cox–Merz materials. *Rheol. Acta*, 48:241.

Wittek, P., Ellwanger, F., Karbstein, H. P., and Emin, M. A. (2021a). Morphology development and flow characteristics during high moisture extrusion of a plant-based meat analogue. *Foods*, 10:1753.

Wittek, P. and Emin, M. (2017). Three-Dimensional Modeling of Food Extrusion Processes. In *Reference Module in Food Science*, page B9780081005965212110. Elsevier.

Wittek, P., Karbstein, H. P., and Emin, M. A. (2021b). Blending proteins in high moisture extrusion to design meat analogues: Rheological properties, morphology development and product properties. *Foods*, 10:1509.

Wittek, P., Pereira, G. G., Emin, M. A., Lemiale, V., and Cleary, P. W. (2018). Accuracy analysis of SPH for flow in a model extruder with a kneading element. *Chem. Eng. Sci.*, 187:256.

Wittek, P., Walther, G., Karbstein, H. P., and Emin, M. A. (2021c). Comparison of the rheological properties of plant proteins from various sources for extrusion applications. *Foods*, 10:1700.

Wittek, P., Zeiler, N., Karbstein, H. P., and Emin, M. A. (2020). Analysis of the complex rheological properties of highly concentrated proteins with a closed cavity rheometer. *Appl. Rheol.*, 30:64.

Wittek, P., Zeiler, N., Karbstein, H. P., and Emin, M. A. (2021d). High moisture extrusion of soy protein: Investigations on the formation of anisotropic product structure. *Foods*, 10:102.

Wong, D. (2018). *Mechanism and Theory in Food Chemistry, Second Edition*. Springer International Publishing, Cham.

Wu, Y. V. and Dimler, R. J. (1963). Hydrogen-ion equilibria of wheat gluten. *Arch. Biochem. Biophys.*, 102:230.

Zhang, X.-M., Feng, L.-F., Chen, W.-X., and Hu, G.-H. (2009). Numerical simulation and experimental validation of mixing performance of kneading discs in a twin screw extruder. *Polym. Eng. Sci.*, 49:1772.

Zhang, X.-M., Xu, Z.-B., Feng, L.-F., Song, X.-B., and Hu, G.-H. (2006). Assessing local residence time distributions in screw extruders through a new in-line measurement instrument. *Polym. Sci. Eng.*, 46:510.

Zhu, X., Sun, M., He, T., Yu, K., Le Zong, and Choi, J.-H. (2021). Study of the cone-shaped drogue for a deep-towed multi-channel seismic survey system based on data-driven simulations. *J. Mar. Sci. Eng.*, 9:1367.

List of Figures

List of Tables

List of Publications

PEER-REVIEWED ARTICLES

F. Ellwanger, R. Kádár, and M. Azad Emin. Observations from capillary and closed cavity rheometry on the apparent flow behavior of a soy protein isolate dough used in meat analogues. *Appl. Rheol.*, 2025. doi: 10.1515/arh-2025-0059.

B. Tsegaye, S. Barman, L. Bovagne, **F. Ellwanger**, E. Kaunisto, N. Lorén, R. Kádár, and M. Stading. Rheological properties of pea protein melts used for producing meat analogues. *Appl. Rheol.*, 2025. doi: 10.1515/arh-2025-0036.

F. Ellwanger, M. Fuhrmann, Heike P. Karbstein, and G. I. Saavedra Isusi. Influence of lowering the ph value on the generation of fibrous structures of protein gels with different network types. *Gels*, 2024. doi: doi:10.3390/gels10030173.

F. Ellwanger, Laurids Pernice, Heike P. Karbstein, and M. Azad Emin. Investigating local residence time and thermomechanical stress profile in twin-screw extrusion of plant proteins by using the moving particle semi-implicit simulation method. *Journal of Food Engineering*, 2023a. doi: doi:10.1016/j.jfoodeng.2023.111665.

F. Ellwanger, Georgantopoulos C. K., H. P. Karbstein, M. Wilhelm, and M. A. Emin. Application of the ramp test from a closed cavity rheometer to obtain the steady-state shear viscosity. *Applied Rheology*, 2023b. doi: doi:10.1515/arh-2022-0149.

K. Dauer, P. Kayser, **F. Ellwanger**, A. Overbeck, A.and Kwade, H. P. Karbstein, and Wagner K.G. Highly protein-loaded melt extrudates produced by small-scale ram and twin-screw extrusion - evaluation of extrusion process design on protein stability by experimental and numerical approaches. *International Journal of Pharmaceutics*, 2023. doi: doi:10.1016/j.ijpx.2023.100196.

P. Wittek, **F. Ellwanger**, Karbstein H. P., and M. A. Emin. Morphology Development and Flow Characteristics during High Moisture Extrusion of a Plant-Based Meat Analogue. *Foods*, 2021. doi: doi:10.3390/foods10081753.

ORAL PRESENTATIONS

F. Ellwanger, M. Fuhrmann, J. Sundermeier, G.I. Saavedra I., and U. van der Schaaf. Shaping texture: The role of pH in meat analog structuring. In *39th EFFoST International Conference, Porto, Portugal*, 17–19 November 2025a.

F. Ellwanger, R. Kádár, and M.A. Emin. Understanding the apparent flow behavior of soy protein isolate formulation used in meat analogs. In *Annual European Rheology Conference, Lyon, France*, 14–17 April 2025b.

F. Ellwanger, H.P. Karbstein, and M.A. Emin. Challenges in obtaining the steady-state shear viscosity of protein-water mixtures under extrusion-like conditions. In *Annual European Rheology Conference, Leeds, United Kingdom*, 9–12 April 2024a.

F. Ellwanger, M. Fuhrmann, H.P. Karbstein, and G. Saavedra Isusi. The pH Modulation during Plant Protein Extrusion: Impact on Meat-Like Structures. In *Plant Protein Extrusion Conference, Chatham, United Kingdom*, 14–15 March 2024b.

F. Ellwanger, H.P. Karbstein, and A.M. Emin. Local process conditions in the twin-screw extruder during the functionalization of highly concentrated protein systems. In *14th European Congress of Chemical Engineering and 7th European Congress of Applied Biotechnology, Berlin, Germany*, 17–21 September 2023a.

F. Ellwanger. Ernährung von Morgen – Insekten und Pflanzen als Proteinlieferanten. In *Gamescom, Köln, Germany*, 23–27 August 2023.

F. Ellwanger, L. Pernice, H.P. Karbstein, and A.M. Emin. Numerische Ermittlung lokaler Prozessbedingungen während der Doppelschneckenextrusion pflanzlicher Proteine. In *Jahrestreffen der DECHEMA-Fachgruppen Hochdruckverfahrenstechnik, Bochum, Germany*, 13–15 March 2023b.

F. Ellwanger, V. Schmid, H.P. Karbstein, and A.M. Emin. Functionalizing insects via twin-screw extrusion. In *Alternative Proteins and Plant-Based Meat, Freising, Germany*, 1–2 June 2022a.

F. Ellwanger, V. Schmid, Marel A.-K., V. Wiedenmann, A. Müller, A.-K. Meinhardt, E. Mayer-Miebach, B. Hetzer, E. Sciurba, M. Huch, H.P. Karbstein, and A.M. Emin. Extrudierte Insektenmehle für die Brotherstellung. In *Anuga Foodtec, Köln, Germany*, 26–29 April 2022b.

F. Ellwanger, A. Husfeldt, H.P. Karbstein, and A.M. Emin. Analyse der Prozessbedingungen während der Doppelschneckenextrusion pflanzlicher Proteine mit numerischen und rheologischen Methoden. In *11. Jahrestreffen der ProcessNet-Fachgruppen Lebensmittelverfahrenstechnik und Trocknungstechnik, Frankfurt am Main, Germany*, 10–11 March 2022c.

POSTER PRESENTATIONS

F. Ellwanger, R. Kádár, and M.A. Emin. Observations from capillary and closed cavity rheometry of the apparent flow behavior of a soy protein isolate formulation used in meat analogs. In *Nordic Rheology Conference and DRG Symposium, Berlin, Germany*, 10–12 June 2025.

F. Ellwanger, M. Fuhrmann, H. P. Karbstein, and G.I. Saavedra Isusi. Modulation of the fibrous structures of high moisture meat substitutes by altering the pH. In *Annual European Rheology Conference, Leeds, United Kingdom*, 9–12 April 2024a.

L. Pernice, A. Schütze, **F. Ellwanger**, U. van der Schaaf, and H. P. Karbstein. Einfluss isolierter Cellulosefasern auf anisotrope Strukuren und die Expansion trockenextrudierter Fleischersatzprodukte. In *Jahrestreffen der DECHEMA/VDI-Fachgruppe Lebensmittelverfahrenstechnik, Quackenbrück, Germany*, 27–28 February 2024.

F. Ellwanger, M. Fuhrmann, H. P. Karbstein, and G.I. Saavedra Isusi. Modulierung der faserartigen Strukturen von nassextrudierten Fleischersatzprodukten durch Veränderung des pH-Wertes. In *Jahrestreffen der DECHEMA/VDI-Fachgruppe Lebensmittelverfahrenstechnik, Quackenbrück, Germany*, 27–28 February 2024b.

F. Ellwanger, H. P. Karbstein, and G.I. Saavedra Isusi. Meat Substitutes as a Source of Protein in the Diet – Influence of Altering the pH on the Formation of Fibrous Structures. In *DECHEMA Infoday "Food Proteins from Biotechnology", Frankfurt am Main, Germany*, 30 November 2023a.

F. Ellwanger, H. P. Karbstein, and A.M. Emin. Numerical and rheological analysis of the twin-screw extrusion process for the production of meat substitutes. In *37th EFFoST International Conference, Valencia, Spain*, 6–8 November 2023b.

K. Dauer, **F. Ellwanger**, A.M. Emin, H. P. Karbstein, and K.G. Wagner. Highly Protein-Loaded Melt Extrudates Produced by Small-Scale Ram and Twin-Screw Extrusion - Evaluation of Extrusion Process Design on Protein Integrity by Experimental and Numerical Approaches. In *AAAPS PharmSci 360, Orlando, FL, USA*, 22–25 October 2023.

F. Ellwanger, L. Pernice, H. P. Karbstein, and A.M. Emin. Using Moving Particle Simulation Approach to Investigate Mechanical and Thermal Stress Profile in a Twin-Screw Extruder. In *14th International Congress on Engineering and Food, Nantes, France*, 20–23 June 2023c.

M. Á. Ballesteros Martínez, **F. Ellwanger**, M. Wittner, and V. Gaukel. Modelling and Analysis of the Effect of Process and Geometry Parameters on Multiphase Flow Formation in ACLR Atomizers. In *Jahrestreffen der ProcessNet Fachgruppen Mehrphasenströmung (MPH) und Computational Fluid Dynamics (CFD 2021), Paderborn, Germany*, 9–10 March 2021.